8-31-2011

Probing ultra-subwavelength inhomogeneities embedded within dielectric targets using photonic nanojets

Cesar Méndez Ruiz

César Méndez Ruiz
Candidate

Electrical and Computer Engineering
Department

This dissertation is approved, and it is acceptable in quality and form for publication:

Approved by the Dissertation Committee:

Jamesina J. Simpson, Chairperson

Christos Christodoulou

Allen Taflove

Sang M. Han

PROBING ULTRA-SUBWAVELENGTH INHOMOGENEITIES EMBEDDED WITHIN DIELECTRIC TARGETS USING PHOTONIC NANOJETS

BY

CÉSAR MÉNDEZ RUIZ

B.S., Electromechanical Engineering, Universidad Panamericana, 2003
M.S., Electronic Engineering, The University of Guadalajara, 2008

DISSERTATION

Submitted in Partial Fulfillment of the
Requirements for the Degree of
Doctor of Philosophy

Engineering

The University of New Mexico
Albuquerque, New Mexico

July, 2011

DEDICATION

To my parents and my brother

ACKNOWLEDGMENTS

I will never be able to thank Dr. Jamesina J. Simpson, my advisor and committee chair, enough for believing in me and so unconditionally supporting me throughout these years. Her guidance and confidence has inspired me in such a strong way that during my Ph.D. program I was able to do unsuspected accomplishments and exploit my potential.

I also want to thank Dr. Christos Christodoulou, committee member, for his valuable teaching during all the classes that I took with him, for his support and for allowing me to run experiments at his laboratory.

A special thanks to the rest of the committee members, Dr. Allen Taflove and Dr. Sang Han for serving on my Dissertation defense committee. I am truly honored that two such prestigious professionals are part of this.

To my parents, Maria Natividad Ruiz Guizar and Antonio Méndez Valencia and my brother, Marco Antonio Méndez Ruiz, thank you for your support and understanding in particular when I decided to leave a lot behind to pursuit one of the biggest dreams in my life. I know that you had to make sacrifices too to make this possible.

To Erik Aspelin, Pat Aspelin, and Mark Aspelin for offering me your support and friendship ever since I first came to Albuquerque. Knowing that I can count on you has been invaluable.

To my good friend Carlos Alberto Larraguivel Lepe, thank you for your supportive words in particular during my toughest moments.

A CONACYT fellowship was held during my study programs.

PROBING ULTRA-SUBWAVELENGTH INHOMOGENEITIES EMBEDDED WITHIN DIELECTRIC TARGETS USING PHOTONIC NANOJETS

BY

CÉSAR MÉNDEZ RUIZ

ABSTRACT OF DISSERTATION

Submitted in Partial Fulfillment of the
Requirements for the Degree of

Doctor of Philosophy

Engineering

The University of New Mexico
Albuquerque, New Mexico

July, 2011

PROBING ULTRA-SUBWAVELENGTH INHOMOGENEITIES EMBEDDED WITHIN DIELECTRIC TARGETS USING PHOTONIC NANOJETS

by

César Méndez Ruiz

B.S., Electromechanical Engineering, Universidad Panamericana, 2003
M.S., Electronic Engineering, The University of Guadalajara, 2008
Ph.D., Engineering, The University of New Mexico, 2011

ABSTRACT

The use of optics to detect ultra-subwavelength features embedded within structures is a hot topic for a broad diversity of applications like spectroscopy, nanotechnology, microscopy, and optical data storage discs. Conventional objective lens based optical systems have a fundamental limit on the best possible resolution of about 200 ηm due to the diffraction of light as it propagates into the far-field. There already exist several near-field techniques with the capability to overcome this limitation, but each of these systems has certain drawbacks related to the complexity of the system or to limitations imposed by the system.

A photonic nanojet is a very particular beam of light that can provide a practical way to overcome the diffraction limit inherent to far-field techniques. A nanojet is an electromagnetic field envelope formed on the shadow-side surface of a plane-wave-illuminated dielectric microsphere of diameter larger than the wavelength

and with refractive index contrast relative to the background medium of less than 2:1. It can maintain a subwavelength transversal beamwidth for distances greater than 2 wavelengths away from the surface of the generating microsphere.

This Dissertation provides a computational test of the hypothesis that the backscattered spectrum resulting from photonic nanojet illumination of a three-dimensional (3-D) dielectric structure can reveal the presence and location of ultra-subwavelength, nanoscale-thin weakly contrasting dielectric inhomogeneities within dielectric targets. The effect of surface roughness on the illuminated side of the target is analyzed, and targets ranging from simple dielectric slabs to complex biological cells are studied. The present work is performed through computational electrodynamics modeling based upon the rigorous, large-scale solution of Maxwell's equations. Specifically, the 3-D finite-difference time-domain (FDTD) method is employed to test the above hypothesis.

Table of Contents

List of Figures

Chapter 1

Introduction

There exists a major thrust by researchers in fields ranging from nanotechnology to biology for developing a means to image structures of sizes on the order of just a few nanometers using visible light. Potential applications are diverse and can vary from optical microscopy, metrology, and ultrahigh-density data storage disks, among many others. The numerical aperture (NA) of conventional lenses limits the maximum resolution to approximately 200 ηm. As a result, resolving nanostructures like a 32 ηm long gate of a transistor in a state of the art integrated circuit (IC), quantum dots in semiconductor wafers, and cellular organelles is not possible with currently well established optical systems that sense electromagnetic (EM) waves propagating in the far-field region. Solid immersion lens (SIL) [1] improves the resolution of an optical system by using a material with high refractive index (*n*) as a background medium. But this solution is limited because it only reduces the illumination wavelength (λ) while remaining diffraction limited.

EM waves that propagate in the near-field can carry information about structures of sizes below the fundamental limit of diffraction that limits the resolution of far-field optical microscopy. However these fields decay exponentially with distance from the target and impose considerable practical limitations on techniques that sense the light less than 1 λ away from the image plane.

Because the diffraction limit is valid only in the far-field region, a fundamental advance for microscopy systems would be to implement a practical way to project the waves propagating in the near-field region into the far-field zone. In a hypothetical one-dimensional (1-D) system, an illuminated ultra-subwavelength structure would locally generate a high-spatial-frequency EM field distribution which would propagate to infinity with zero attenuation or spreading. In consequence, the information regarding the structure would be obtainable at any arbitrary distance from the image plane regardless of its size or *n* contrast.

A photonic nanojet [2]-[6] is a particular beam of light that emerges from the shadow side of a plane wave illuminated dielectric sphere or cylinder, provided that the dielectric has the correct diameter with respect the λ and *n* contrast with respect the background medium. The photonic nanojet represents the closest known approximation to 1-D photon propagation realizable in a practical optical system.

The broad goal of this research is to advance a new means for inverse scattering by testing the hypothesis that the backscattered spectrum resulting visible light illumination with a photonic nanojet can be analyzed to detect and characterize ultra-subwavelength inhomogeneities embedded within dielectric targets.

1.1 State of the Art in Detecting Ultra-Subwavelength Features

There already exist techniques to overcome the fundamental diffraction limit of imaging resolution inherent to far-field optics. But these are achieved at the expense of increasing the complexity of the system and by introducing limitations. Initial research related to this topic can be traced back to 1928 when

E.H. Synge first proposed the basics for what at present is known as the near-field scanning optical microscopy (NSOM) [7]. Synge proposed to replace the lens by a subwavelength aperture in an opaque screen; this aperture is to be positioned close to the surface of the target. The light that propagates trough the aperture in the screen is forced to interact with the sample before diffracting away from the aperture. In this configuration it is the size of the aperture rather than the diffraction limit that determines the spatial resolution of the system. NSOM is capable of reaching a lateral resolution of 20 ηm and vertical resolution of 2–5 ηm [8]. The disadvantages of NSOM are the low light-collection efficiency, relatively slow image-acquisition rate and sensitivity limited to superficial features of the target.

Metamaterials can be implemented in optical frequencies to generate slabs with negative *n* [9]. With the correct configuration, it is possible to focus all spectral components of the light propagating in the near-field region, even the evanescent modes. The problem comes with the fabrication process of this kind of superlense because the parameters of the material are extremely sensitive to small deviations which can make the subwavelength structures unobservable and limit the usable frequency range. Also, the intrinsic resonant nature of most metamaterials makes them highly dispersive.

Metamaterials can also be implemented by exploiting the dynamic properties of surface plasmons. With this option, applicable only to the particular frequency range of visible light, it is possible to produce nano-sized isolated hot spots [10]

but the control over their position is limited which makes them unsuitable for imaging applications.

Fluorescence based methods, like Stimulated Emission Depletion microscopy (STED) [11], allow the detection of structures of size substantially smaller than the illuminating focus size. A resolution of 5.8 ηm has been recently achieved [12]. The fluorescent dyes present a non-linearity de-excitation that is used together with standard confocal laser scanning microscopes and conventional far-field optical microscopes to reconstruct an image of the target. As a consequence the resolution depends on the shape of the optical focus of a conventional lens system, which makes them susceptible to distortions due to scattering. An additional drawback of fluorescence microscopy is that it is not always possible or desirable to dope the target to sense.

Other attempt to improve resolution that belongs to the far-field techniques is the SIL [1]. This technique employs a material with high *n* as a background medium to reduce the wavelength of the illuminating light. But this solution still results in a diffraction limited system.

Northwestern University and NorthShore University HealthSystem researchers have pioneered a partial wave spectroscopy (PWS) technique that has been successful in providing experimental and clinical evidence of early cancer detection capability based on spectrum analysis of backscattered light [13], [14]. PWS is based upon the assumption that detection of photons propagating in a 1-D channel permit a reflected optical signal to be sensitive to length-scales of *n* fluctuations much smaller than the classical diffraction limit. The analyzed signal

is not affected by the far-field interference of all waves propagating within the scatterer but is determined by a subset of these waves (1-D). The microscope is composed by a complicated system that involves a series of lenses, condenser, aperture, and beam splitter. It divides the area to image in a collection of 1D parallel channels of diffraction limited transverse size.

More recently a novel kind of scattering lens has been experimentally demonstrated to image gold nanoparticles [15]. The principle of operation is to manipulate the wave front of the incident light in the correct way so that when it illuminates a strongly disordered scattering layer on top a high *n* dielectric slab, it produces constructive interference in all propagating angles within the slab. The result is a spherical wave that converges toward the image plane. In [15] the authors imaged gold nanoparticles at an optical resolution of 97 ηm diameter, whereas photonic nanojets have been demonstrated to image gold nanoparticles of 50 ηm of diameter [16]. Also, in [15], van Putten *et al*. do not provide insight into the distance over which the transverse section of the beam is maintained in subwavelength scales, whereas for photonic nanojets the subwavelength beamwidth can extend for about 2λ or more [5].

1.2 Applications for Breaking the Fundamental Limit of Diffraction

In order to put in context the relevance of the research on improving the capability of optical systems to sense thinner and narrower inhomogeneities embedded within dielectric objects, this section is devoted to briefly reviewing some potential applications that can result from this kind of improvement to imaging systems.

1.2.1 Ultrahigh-Density Data Storage Disks

The latest advance for optical data storage disks available on the market is the format transition from the DVD™ to BluRay™. The increment in data storage density was achieved by a reduction of the illuminating light λ from 650 ηm to 405 ηm, an increment of the NA from 0.60 to 0.85 and a reduction of the cover layer thickness. These changes result in a reduction of the spot size to 580 ηm. However this improved optical system is still diffraction limited.

Photonic nanojets have been applied to develop ultrahigh-density data storage disks in which the data are recorded on pits in an aluminum substrate [17]. The system works with 400 ηm light to illuminate pits having lateral dimensions of 50 ηm by 80 ηm, which is a significant reduction with respect BluRay™ technology. The high levels of backscattered light enabled by the photonic nanojet can allow multiple data values on a single spot size by sensing the pith-dept or pith-pair separation to code information.

1.2.2 Inspection of Semiconductor Wafers

One of the most obvious challenges in scaling IC designs to follow Moore's law is in the dealing with devices with basic structures just a few ηm in size. State of the art IC is currently fabricated with Intel® 32 ηm Logic Technology [18]. To support maintain a high yield in the manufacturing of these devices, it is necessary to have a metrology system capable of determining the presence and location of basic circuitry elements and unintended contamination on semiconductor wafers. Chen et al. [19] patented a technique to determine the presence, location and dimensions of a structure by measuring the retroreflected light from a target that is illuminated by a nanojet. The solved structure can be an isolated, periodic or

non-periodic geometry formed at the surface of the wafer; the basic elements of this structure can be the gate of a transistor, a transmission line, drain, vias and even contaminating particles. The existence and size of a structure is determined by measuring the backscattered light intensity scanned at different scattering angles and scanning positions and then comparing against a set of predetermined set of backscattering signatures. So this is a library based technique that is also only concerned with superficial features.

1.2.3 Microscopy

In biological and medical sciences there exists an increasing need to understand processes inside a cell at a nanoscale level that involve measurements of ultra-subwavelength refractive index fluctuations. The sensitivity of spectroscopy of elastic scattering is not enough to image fundamental organelles like nucleosomes, cytoskeleton, ribosomes, and mitochondria. Probably the hottest application relating to the need to image smaller features inside of cells is the early detection of cancer.

It is well accepted that the process of carcinoma formation involves stepwise accumulation of genetic and epigenetic alterations that can take many years before histological (microarchitectural) aberrations appear. This means a cancer cell may look histologically normal and still have architectural nanoscale aberrations. Spatial dependence of intracellular solids (lipids, DNA, proteins, RNA) generates a spatial dependence of n, and for biological tissue these n fluctuations can range from 0.02 to 0.1 [20]. The average dimension of a unit block where n is constant determines the aggressiveness of the cell line.

As shown in the work of this Dissertation, photonic nanojets can be used to illuminate a cell under study and then project into the far field zone the high-spatial-frequency EM field distribution generated by the sub-wavelength *n* fluctuations within the cell.

1.3 Dissertation Statement

The objective of the research discussed in this dissertation is to provide a fundamental advance in inverse scattering. Specifically, the following hypothesis is tested: the backscattered spectrum resulting from visible-light illumination of a dielectric microsphere can be analyzed to characterize nanoscale-thin (i.e., ultra-subdiffraction thickness) localized dielectric inhomogeneities within a three-dimensional (3-D) dielectric structure that is on the shadow side of the dielectric sphere. The hypothesis effectively involves an investigation of whether a 3-D inverse-scattering problem involving photonic nanojet illumination of a dielectric target can be effectively reduced to what amounts to be 1-D.

Kong. *et al.* [6] demonstrated the quasi 1-D EM wave propagation of a photonic nanojet. In the research work of this dissertation the backscattered spectrum is found to be extremely sensitive to the presence of ultra-subwavelength dielectric inhomogeneities within the nanojet. This is especially revealed by examining the DFT of the backscattered spectrum, which yields the backscattered cepstrum.

Results from 1-D and 3-D finite-difference time-domain (FDTD) [21] [22] simulations indicate that the backscattered cepstra of a ηm-thick dielectric layer embedded within a dielectric slab are nearly identical. Further, the ηm-thick dielectric layer remains detectable as it is narrowed in the transverse direction

even below the width of the nanojet. The implication of this is that the nanojet yields a sufficiently 1-D electromagnetic excitation / backscattering geometry to allow detection of ultra-subwavelength-thin dielectric inhomogeneities, with a transverse resolution of approximately the classical diffraction limit.

Additional configurations involving flat dielectric slabs are considered to characterize the effects on the cepstra curve of the position of the inhomogeneity with respect to the slab surface, the number of inhomogeneities among some other parameters.

Effects of the slab surface are first studied by considering dielectric slabs having checkered surface pattern and later random surface roughness. It is found that the surface roughness decreases the backscattered light but improves the contrast of the backscattering from the inhomogeneity with respect to that from the dielectric slab itself.

Finally, the backscattering from a sample human colon cell HT29 cell is considered. The topography of this cell is imported to the FDTD model from measurements taken with Atomic Force Microscopy (AFM) that Marc Richter, a PhD student at the Institute of Photonic Technology (IPHT), shared with Prof. Simpson's Computational Electrodynamics Laboratory.

1.4 Dissertation Outline

The maximum resolution of optical systems that sense photons propagating in the far-field zone is limited by the diffraction of light. There exists several techniques that overcome this limit but these are achieved at the expense of increased complexity and imposed limitations. Mesoscopic light transport theory

predicts that 1-D photon propagation is sensitive to any length scale of refractive index fluctuations, making it possible to detect them at any arbitrary distance from the target. The photonic nanojet is a 3-D beam of light known to present the best approximate 1-D photon propagation. Photonic nanojets can also have a subwavelength full-width at half-maximum (FWHM). These characteristics among others make photonic nanojets a promising option for reaching ultra-subwavelength width resolution for microscopy, metrology and ultrahigh-density data storage disks. The present work validates that the backscattered spectrum resulting from photonic nanojet illumination of a dielectric structure having nanoscale-thin localized dielectric inhomogeneities can be analyzed to solve for the characteristics of the *n* fluctuations within the target.

The remainder of this dissertation is organized as follows: The FDTD method and formulations used in this research are summarized in Chapter 2; an insight to photonic nanojet characteristics is presented in Chapter 3; analysis of all the different photonic nanojet / target simulation cases considered are documented in Chapters 4-6; possible future work is proposed in Chapter 7; and Chapter 8 concludes the dissertation.

Chapter 2

The FDTD Method

2.1 Introduction

Modern approaches and capabilities in solving EM problems have evolved a long way since the unification of the electric and magnetic forces in one single mathematical model by James Clerk Maxwell in 1861. The need to develop effective and reliable radar systems, together with countermeasures aimed at jamming or avoiding radars for defense purposes during World War II were the initial applications of Maxwell's equations solutions. During this era, EM problems were solved using closed-form and infinite-series analytical solutions for sinusoidal steady state [22].

After about 1960, the frequency domain techniques became more sophisticated because of the increased availability of programmable electronic digital computers. The powerful new high-level programming languages, rapid data storage capacity, and fast computational speeds brought new capabilities not possible with mechanical calculators used before 1960. Initial advances on frequency-domain techniques involved high-frequency asymptotic methods [23] and integral equations [24].

The limitations of frequency-domain integral-equation solutions for Maxwell's equations together with the increased computational and memory capabilities of computers of the 1970s and 1980s lead to the exploration of direct time-domain solutions of Maxwell's differential equations on spatial grids. The FDTD method

was the first technique to solve EM problems this way. There are seven primary reasons [22] why the FDTD method has expanded beyond defense applications and also make it suitable for this present work:

- FDTD avoids the difficulties of dealing with linear algebra because it is a fully explicit computation
- The sources of error have been identified and countermeasures aimed at solving or limiting them have been developed
- A single simulation can provide the response over the complete spectrum of the excitation source
- FDTD can calculate directly any nonlinear response of the system
- The implementation of a new problem is done by defining the corresponding grid without the need of reformulating an integral equation
- Computer memory keeps increasing according to Moore's law which mitigates FDTD's significant computational resources requirements
- Since FDTD calculates EM fields everywhere as they evolve in time, it is straightforward to generate animated displays of the electromagnetic field propagation through the domain. This type of display is useful in understanding the model

Currently, FDTD is one of the most popular methods for solving Maxwell's equations to model: electromagnetic wave guiding, radiation, scattering, electromagnetic coupling, resonances, among other applications. It is a wide-band computational technique that can go from near-DC to visible light. Some examples are:

- Near-DC: Ultralow-frequency geophysics involving the entire Earth-ionosphere waveguide
- Microwaves: Radar systems, antennas, wireless communications devices, digital interconnects, biomedical imaging/treatment
- Visible light: Photonic crystals, nanoplasmonics, solitons, and biophotonics

2.2 Algorithm

Maxwell's differential (curl) equations in time domain, which correspond to Faraday's law and Ampere's law respectively, are:

$$\nabla \times \mathbf{E} = -\frac{\partial \mathbf{B}}{\partial \mathrm{t}} - \mathbf{M} \tag{2.1}$$

$$\nabla \times \mathbf{H} = \frac{\partial \mathbf{D}}{\partial \mathrm{t}} + \mathbf{J} \tag{2.2}$$

where

$\mathbf{E}$: Electric field

$\mathbf{H}$: Magnetic field

$\mathbf{D}$: Electric flux density

$\mathbf{B}$: Magnetic flux density

$\mathbf{J}$: Electric current density

$\mathbf{M}$: Equivalent magnetic current density

The constitutive relations can be used to relate $\mathbf{D}$ to $\mathbf{E}$ and $\mathbf{B}$ to $\mathbf{H}$ for linear, isotropic, nondispersive materials.

$$\mathbf{D} = \varepsilon \mathbf{E}; \quad \mathbf{B} = \mu \boldsymbol{H} \tag{2.3}$$

where

ε: Electrical permittivity

μ: Magnetic permeability

Note that equations (2.1) and (2.2) form a system of time-domain Partial Differential Equations (PDEs) where the change in time of $\mathbf{E}$ is coupled with the change in time of $\mathbf{H}$ across space. The basic algorithm works by approximating all of the temporal and spatial derivatives as finite central-differences in a discretization procedure that employs the Yee lattice scheme. The system is then solved for the new value of $\mathbf{E}$ as a function of the value of $\mathbf{E}$ already stored in memory and the curl of the local distribution of the $\mathbf{H}$-field in space. Then the corresponding calculation to update the value of $\mathbf{H}$ is performed in a similar manner. This single calculation cycle represents a temporal advance of one time step. As enough calculation cycles are completed, the response of the system is progressively obtained.

In the Yee algorithm, the $\mathbf{E}$ and $\mathbf{H}$ fields are decomposed in 3-D spatial components and placed along the edges and normal to the faces of a cube. For the particular case of the Cartesian coordinates system, the locations of the field components are arranged so that every $\mathbf{E}$ component is surrounded by four circulating $\mathbf{H}$ components and vice versa. Fig. 1 shows the exact location and direction of each electric and magnetic field component on the unit cell that represents the fundamental building block of the complete FDTD grid.

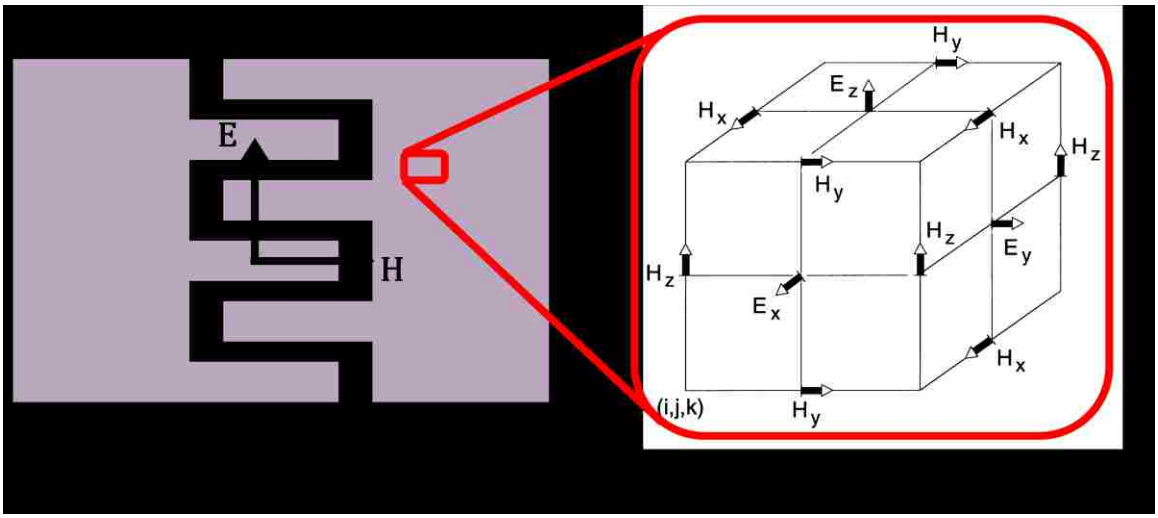

Figure 1: Illustration of a Cartesian unit cell which is the basic element to construct the complete computational domain. Each of the 6 field components are shown at their corresponding locations and orientations within the Yee cell. The primary lattice on the right side was taken from Ref. [22].

The Yee algorithm is second-order accurate because it implicitly uses central differencing in both time and space. Also note that in the absence of a source the mesh is divergence free, therefore the two Gauss' laws

$$\nabla \cdot D = q_{ev}; \qquad \nabla \cdot B = q_{em}$$

(with q_{ev} and q_{em} are the electric and equivalent magnetic charge density respectively; their value is equal to 0 for the source free case) are implicitly respected.

Before applying the discretization scheme on equations (2.1) and (2.2), it is necessary to decompose them into a set of 6 equations, one for each Cartesian component of $\mathbf{E}$ and $\mathbf{H}$. For convenience, only the equations to update the x component of each field are shown below. The derivation of the other four components leads to similar equations.

$$\frac{\partial H_x}{\partial t} = \frac{1}{\mu}\left[\frac{\partial E_y}{\partial z} - \frac{\partial E_z}{\partial y} - \left(M_{source_x} + \sigma^* H_x\right)\right] \tag{2.4}$$

$$\frac{\partial E_x}{\partial t} = \frac{1}{\varepsilon}\left[\frac{\partial H_z}{\partial y} - \frac{\partial H_y}{\partial z} - \left(J_{source_x} + \sigma E_x\right)\right] \tag{2.5}$$

Note that the current densities $\mathbf{J}$ and $\mathbf{M}$ were each broken into two components. One component is meant to allow for independent sources to excite the computational domain ($\mathbf{J_{source}}$ and $\mathbf{M_{source}}$) and the other to account for the effect of lossy materials

$$\mathbf{J} = \mathbf{J_{source}} + \sigma\mathbf{E}; \qquad \mathbf{M} = \mathbf{M_{source}} + \sigma^*\mathbf{H}$$

with

σ: electric conductivity

σ^*:equivalent magnetic loss

An appropriate substitution of the central differencing scheme in equations like (2.5) results in:

$$\frac{E_x|_{i,j+1/2,k+1/2}^{n+1/2} - E_x|_{i,j+1/2,k+1/2}^{n-1/2}}{\Delta t} =$$

$$\frac{1}{\varepsilon_{i,j+1/2,k+1/2}} \cdot \left(\begin{array}{c} \dfrac{H_z|_{i,j+1,k+1/2}^{n} - H_z|_{i,j,k+1/2}^{n}}{\Delta y} - \dfrac{H_y|_{i,j+1/2,k+1}^{n} - H_y|_{i,j+1/2,k}^{n}}{\Delta z} - \cdots \\ J_{source_x}|_{i,j+1/2,k+1/2}^{n} - \sigma_{i,j+1/2,k+1/2} E_x|_{i,j+1/2,k+1/2}^{n} \end{array} \right)$$

The field component E_x on the right side of the equation is not stored in memory at time n. It is necessary to estimate it with the semi-implicit approximation

$$E_x|_{i,j+1/2,k+1/2}^{n} = \frac{E_x|_{i,j+1/2,k+1/2}^{n+1/2} + E_x|_{i,j+1/2,k+1/2}^{n-1/2}}{2}$$

to obtain the final form implemented in the code:

$$E_x|_{i,j+1/2,k+1/2}^{n+1/2} = \left(\frac{1-\frac{\sigma_{i,j+1/2,k+1/2}\Delta t}{2\varepsilon_{i,j+1/2,k+1/2}}}{1-\frac{\sigma_{i,j+1/2,k+1/2}\Delta t}{2\varepsilon_{i,j+1/2,k+1/2}}}\right) E_x|_{i,j+1/2,k+1/2}^{n-1/2} + \cdots$$

$$\left(\frac{\frac{\Delta t}{\varepsilon_{i,j+\frac{1}{2},k+1/2}}}{1+\frac{\sigma_{i,j+\frac{1}{2},k+1/2}\Delta t}{2\varepsilon_{i,j+1/2,k+1/2}}}\right) \cdot \left(\begin{array}{c} \frac{H_z|_{i,j+1,k+\frac{1}{2}}^{n} - H_z|_{i,j,k+\frac{1}{2}}^{n}}{\Delta y} - \cdots \\ \frac{H_y|_{i,j+\frac{1}{2},k+1}^{n} - H_y|_{i,j+\frac{1}{2},k}^{n}}{\Delta z} - \cdots \\ J_{source_x}|_{i,j+1/2,k+1/2}^{n} \end{array}\right)$$

The equations to compute the remaining five field components can be obtained in a similar manner.

It is worth mentioning that for practical implementation of the demanding computation and storage resources required by the modeling considered in this Dissertation, it becomes necessary to exploit parallel processing techniques. Specifically, the domain decomposition parallelism scheme in which the computational domain is divided into equal rectangular sub-areas is employed. The essential elements of a parallel algorithm for the FDTD method using the Message Passing Interface (MPI) library are reported in [25]. With this implementation, the FDTD updates are calculated independently by each processor for its respective local mesh. After every time step the data are exchanged between neighboring sub-domains.

2.3 Scattered Field Formulation

Because the present work concerns about backscattering from a plane wave illuminated dielectric sphere in front of a dialectic target to be sensed, two particular FDTD formulations are used: Scattered Field Formulation (SF) and Total-Field / Scattered-Field formulation. The former is reviewed in this section;

the latter is left for section 2.4. Also, this section is specialized in the application of the SF formulation to lossy dielectric scatterers. There are important differences in the implementation of SF for the case of perfect electric conductor (PEC) structures. Refer to [22] or [26] for details on how to treat the case of metallic scatterers.

In the SF formulation, the linearity of the Maxwell's equations is used to decompose the total EM fields ($\mathbf{E}_t$ and $\mathbf{H}_t$) into incident fields ($\mathbf{E}_i$ and $\mathbf{H}_i$) and scattered fields ($\mathbf{E}_s$ and $\mathbf{H}_s$).

$$\mathbf{E} = \mathbf{E}_t = \mathbf{E}_i + \mathbf{E}_s; \qquad \mathbf{H} = \mathbf{H}_t = \mathbf{H}_i + \mathbf{H}_s \tag{2.6}$$

The plane wave that illuminates the scatterer is the incident component of the total field and is assumed to propagate in free space; therefore it can be calculated analytically or with the aid of a separated 1-D FDTD simulation.

$$\nabla \times \mathbf{E}_i = -\mu_o \frac{\partial \mathbf{H}_i}{\partial t}$$

$$\nabla \times \mathbf{H}_i = -\varepsilon_o \frac{\partial \mathbf{E}_i}{\partial t}$$

With μ_o and ε_o representing the free space permeability and permittivity respectively. The FDTD method is used to time step only the scattered fields throughout the complete space domain. Substraction of the incident fields from the total fields results in:

$$\nabla \times \mathbf{E}_s = -\mu \frac{\partial \mathbf{H}_s}{\partial t} - \sigma^* \mathbf{H}_s - \sigma^* \mathbf{H}_i - (\mu - \mu_o) \frac{\partial \mathbf{H}_i}{\partial t} \tag{2.7}$$

$$\nabla \times \mathbf{H}_s = \varepsilon \frac{\partial \mathbf{E}_s}{\partial t} + \sigma \mathbf{E}_s + \sigma \mathbf{E}_i + (\varepsilon - \varepsilon_o) \frac{\partial \mathbf{E}_i}{\partial t} \tag{2.8}$$

The central differentiation scheme explained in section 2.2 can be applied to (2.7) and (2.8) for implementation in a FDTD code. With this formulation, the sources that excite the FDTD simulations are the interaction of the known incident fields with the material that forms the scatterer. Therefore the incident fields have to be calculated for all locations in the grid where the properties are different than those corresponding to vacuum. If the total field waveform in the time domain is needed, it can be obtained by adding the known incident field to the FDTD-computed scattered-field in a data postprocessing procedure.

2.4 Total-Field / Scattered-Field Formulation

This technique offers a second option to model plane wave illumination of a structure and to isolate the fields scattered by the object from the total fields. Again, linearity of Maxwell's equations is exploited to decompose the total EM fields as indicated in (2.6). The main difference between SF and Total-Field / Scattered-Field (TF/SF) is that in the latter the Yee algorithm is applied to all three: incident field, scattered field, and total field. To accomplish this, the computational domain is segmented in 2 regions, as shown in Fig. 2.

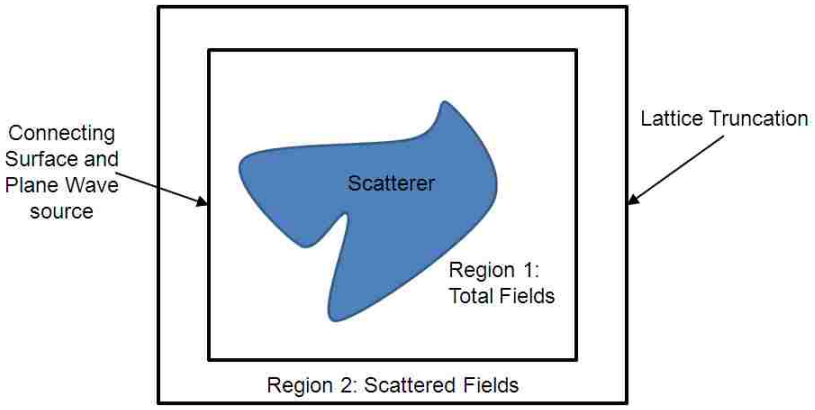

Figure 2: TF/SF segmentation of computational domain. Total Field and Scattered Field regions are separated by a virtual surface. The scattered field zone is surrounded by the lattice truncation, which performs the function of Absorbing Boundary Conditions.

The Yee algorithm operates on total fields to time step them through the inner most region of the grid (Region 1), where the scattering structure is located. Only scattered fields are propagating In Region 2, this means that no incident field component is present in the outer most region. Appropriate absorbing boundary conditions (ABC) surround Region 2 to truncate the complete grid. The two regions need to be separated by a virtual surface to isolate the incident field within Region 1 but at the same time to allow scattered fields to enter Region 2. It is also during this connecting functionality that the virtual surface serves as the source of the incident plane wave.

TF/SF is a very flexible technique that allows for definition of an incident plane wave having any desired time waveform, duration, angle of incidence, and polarization. It is also convenient that the incident field needs to be calculated only along the connecting virtual surface where the wave is assumed to propagate in free space. This makes the problem of computing the incident field independent of the scatterer material properties and geometry.

2.5 Convolutional Perfectly Matched Layer

The maximum size of the FDTD grid that can be simulated is limited by computer resources. Unless appropriate ABCs are implemented in the model, unintended reflections will propagate back into the computational domain when the wave impinges the outer lattice boundary. This is a problem that must be addressed because the EM problems considered in this dissertation are defined to have unbounded regions in the three Cartesian directions. Therefore it is necessary to simulate an infinite space at the boundaries of the grid.

One popular approach to realize ABCs is to place an outer-layer absorbing material medium to bring unwanted reflections down to acceptable levels. In 1994, Berenger introduced the most successful absorbing-material ABCs which is termed Perfectly Matched Layer (PML) [27]. The PML reduced the reflections from state-of-the-art ABCs at the time further by a factor of 100. Further, it efficiently absorbs plane waves of arbitrary angles of incidence, polarization, and frequency.

Convolutional PML (CPML) [28] is a more recently developed and improved version of the PML, and it is the ABC employed in this Dissertation. CPML is an implementation of the Complex Frequency Shifted (CFS) tensor [29] based on the stretched coordinate form of the PML [30] and a recursive convolution (RC) method originally proposed by Luebbers, *et al.* [31], [32]. The main advantages of CPML are that it is completely independent of the host medium and, unlike PML, it is highly absorptive of evanescent modes.

Chapter 3

The Photonic Nanojet

3.1 Introduction

In this work the dielectric targets are illuminated with a photonic nanojet. In Chapter 1 the photonic nanojet was described to be a particular beam of light that emerges from the shadow side of a plane wave illuminated dielectric sphere or cylinder and to be the closest known approximation to 1-D photon propagation realizable in a practical optical system. In this Chapter, the key characteristics and physics behind the formation of a nanojet are reviewed. Then, while conducting the 3-D FDTD modeling studies of this Dissertation, it was found that by using a modified *n* profile of layered microsphere the length of the photonic nanojet can be increased longer than that obtained with the *n* profile reported in Kong et al [6]. Section 3.3 documents how this elongated photonic nanojet is accomplished. Finally, this Chapter is complemented with a brief review of some theory related to photon propagation in 1-D.

3.2 Characteristics of Photonic Nanojets

A photonic nanojet [2]-[6] is a narrow, high-intensity field envelope that emerges from the shadow-side surface of a plane-wave-illuminated dielectric microcylinder or microsphere of diameter larger than the illuminating λ and appropriate *n* contrast with respect the background medium. This beam having a unique combination of a narrow waist and little divergence has been called photonic nanojet by Chen and Taflove [2], drawing an analogy between the high-speed gradient typical in a jet fluidic mechanics and the corresponding high light flux

gradient. Fig. 3 shows one sample photonic nanojet generated by a silica microsphere that is submerged in water.

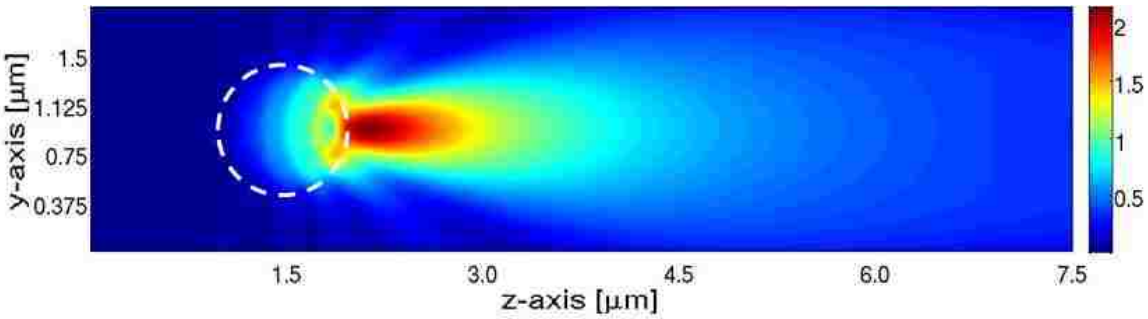

Figure 3: Visualization of a photonic nanojet generated by a plane-wave-illuminated silica microsphere of 1.0 µm diameter submerged in water. The λ of incident light is 500 ηm; the wave propagates from left to right.

Ever since it was initially identified, the photonic nanojet has been found to exhibit the following key properties [5], [6]:

- Its maximum intensity typically exceeds by a significant ratio that of the incident plane-wave.
- A nanojet is capable of maintaining a subwavelength full-width at half-maximum (FWHM) at distances from the shadow-side surface of the dielectric microcylinder or microsphere that can extend more than ~2λ without significant divergence.
- The transverse beamwidth can be shorter than the classical diffraction limit. The lowest realizable limit seen so far is about λ/3.
- It can appear for a wide range of dielectric microcylinders or microspheres with diameters d_μ that range from about 2λ to more than 40λ, provided that the n contrasts with respect the background medium are less than 2:1.
- A metallic nanoparticle of diameter d_n that is located within the nanojet perturbs the backscattered power projected into the far-field from the

illuminated microsphere by an amount that varies as d_n^3 for a fixed λ. This perturbation is much higher than the d_n^6 dependence that corresponds to Rayleigh scattering for the same nanoparticle when it is illuminated by a plane-wave.

The d_n^3 perturbation behavior leads to the possibility of detecting a nanoparticle via its perturbation of the backscattering of the microsphere. In fact, experiments at visible light regime and scaled up to the microwave frequencies as well have demonstrated that a metallic particle of only 1/100th the diameter of the dielectric sphere can increase the backscattered power by about 2 times that of the dielectric sphere alone [4], [16], [33].

Fig. 4, taken from Ref. [5], vividly illustrates the final property above: extreme sensitivity of the amplitude of the backscattered nanojet to a nanoparticle perturbation. In this example, a 3.5 μm-diameter dielectric sphere of n = 1.59 is illuminated in an infinite vacuum region by an x-polarized, z-propagating plane wave of λ = 400 ηm. A d_n = 20 ηm gold nanoparticle moving along the dotted path causes a peak backscattered power perturbation of +40% relative to the backscattered power of the isolated microsphere. This perturbation is only 4 dB below the full backscattered power of the isolated microsphere, and is caused by a nanoparticle that is 175-times smaller than the microsphere in diameter, and hence more than 30,000-times smaller than the microsphere in cross-section area. In effect, *the nanojet projects the presence of the nanoparticle to the far field*.

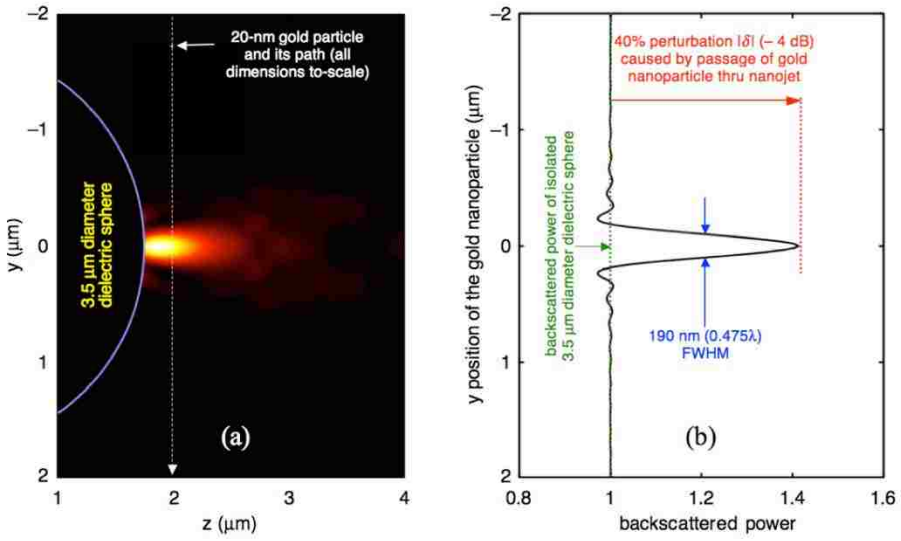

Figure 4: Extreme sensitivity of the amplitude of a backscattered nanojet to a gold nanoparticle. The dotted path is 240 ηm from the microsphere surface at the closest point [5].

3.3 The Elongated Photonic Nanojet

Kong. *et al*. [6] demonstrated how the length of the photonic nanojet can be increased to several microns (4.7 μm in their particular work) by radially grading the *n* of the generating microsphere, having the highest *n* at the center. In conducting the 3-D FDTD modeling studies used in this Dissertation, it was found that an even longer nanojet could be produced, up to ~20 μm, using an alternative radial grading. Fig. 5 illustrates the results of such a grading for an x-polarized plane-wave-illuminated (λ = 500 ηm) 5 μm diameter microsphere in free space, wherein six equally thick spherical shells are assumed. In order, from the outer shell to the inner core, the refractive indices of the modified profile are *n* = 1.02, 1.04, 1.06, 1.08, 1.10, and 1.12. (These values of *n* are physically realizable using recent technology [34]) It is important to note that the lengthening of the nanojet of Fig. 5 relative to the nanojet of Fig. 4 comes at the expense of its widening in the transverse direction to a FWHM of 1.28 μm (~2.5λ). This is wider than the original nanojet's transverse width of ~λ/3,

however utilizing the elongated nanojet, inhomogeneities located deeper inside the scattering object may be detected.

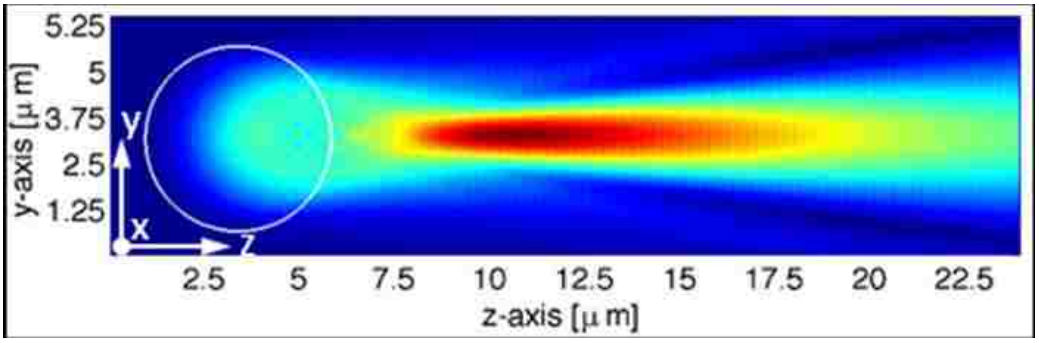

Figure 5: Visualization of an elongated photonic nanojet generated by a plane-wave-illuminated, six-layer radially graded dielectric microsphere of 5 μm diameter. The incident wave is polarized along x-axis and propagates along the z-axis.

The difference between the radial grading used in this Dissertation and that of [6] is the contrast of the refractive index between each layer of the microsphere, and the lower average value of the microsphere layers. An alternative approach to changing the length of the nanojet is to alter the background medium as done in Wang *et al*. [35]. In this case, a homogeneous microsphere (n = 1.45332) surrounded by water (n = 1.326) yields a longer nanojet compared to when air is employed as the background media. That is, when the microsphere refractive index is closer in value to that of the background medium, the photonic nanojet is longer.

3.4 Physics behind Photonic Nanojets

A detailed understanding of the physics that leads to the formation of a photonic nanojet is important to this Dissertation. The optimum selection of the microsphere parameters to engineer an optical beam having desirable properties, as well as the correct interpretation of the interaction of this beam with

certain targets depend in a great degree upon the understanding of the physics behind the electrodynamics of the photonic nanojet.

Full wave analysis via 3-D FDTD is employed in this work to have the capability of modeling in a practical way backscattering from complex dielectric targets like the human colon cancer cell HT29 including the superficial features of its membrane and random *n* fluctuations. However for the simpler problem of scattering from a single, isotropic, homogeneous dielectric microsphere there already exist validated analytical methods like Mie theory formulated in 1908 [36]. Although such analytical evaluations are not always straightforward, one advantage of these solutions is that they can provide insight into the physics that govern the formation a photonic nanojet.

The Mie theory solution can be expanded into a Debye series [37] to bridge the gap between physical optics and geometrical optics [38]. However special care must be taken during the numerical evaluation because an improper algorithm can lead to significant errors when the characteristic length of the scatterer becomes much larger than the illuminating λ. A combination of geometrical optics, Mie theory and angular spectrum analysis can be employed to perform the numerical evaluation [38]. The convenience of this calculation algorithm resides in its ability to relate the spatial characteristics to its spatial frequency content.

The geometry for the Mie solution is shown in Fig. 6

Figure 6: Elements of the Mie theory solution. A dielectric sphere is illuminated by a plane wave which in the analysis is assumed to be TM. The origin of the coordinate systems is at the center of the sphere.

The magnitude of the magnetic field polarized in the z-direction (h) has to satisfy the Helmholtz equation

$$\nabla^2 h + n^2 k^2 h = 0 \tag{3.1}$$

where k is the magnitude of the free space wave vector. (3.1) is applied on the three: incident plane wave (h_{inc}), magnetic field inside the particle (h_1), and the scattered field in the surrounding region (h_2). The general solutions in polar coordinates can be written in terms of Bessel and Henkel functions [39].

$$h_{inc}(r,\varphi) = \sum_{m=0}^{\infty} c_m \cos(m\varphi) J_m(n_2 kr) \tag{3.2}$$

Where

$$c_m = \begin{cases} 1, & m = 0 \\ 2i^m, & m > 0 \end{cases}$$

And J_m is the Bessel function of the first kind of order m

$$h_1(r,\varphi) = \sum_{m=0}^{\infty} (a_m \cos(m\varphi) + \tilde{a}_m \sin(m\varphi)) J_m(n_1 kr) \tag{3.3}$$

$$h_2(r,\varphi) = \sum_{m=0}^{\infty} \left(b_m \cos(m\varphi) + \tilde{b}_m \sin(m\varphi)\right) H_m^{(1)}(n_2 kr) \tag{3.4}$$

The Bessel function of the first kind is appropriate for the incident and inside the particle fields because its value is finite at the origin. The Henkel function of the first kind ($H_m^{(1)}$) behaves like a wave propagating outwards for large r.

The values of the coefficients a_m and b_m are found by enforcing continuity of tangential components of magnetic and electric fields on the surface of the sphere.

The Debye-series approach analyzes the scattering problem by decomposing the total field into components of transmitted and reflected fields. The radially outgoing cylindrical wave and the incoming cylindrical wave (described by the Henkel function of the second kind, $H_m^{(2)}$) are designated by the modes *O* and *I* respectively; with subscript 1 to denote inside the particle and 2 to denote outside the particle.

Under the assumption that the I_2 mode produces a reflected mode O_2 and transmitted mode I_1, boundary conditions are used again but in this occasion to calculate the coefficient R_{22} for the reflection of the I_2 mode and T_{21} for transmission into the particle. Also, an O_1 mode is assumed to generate a reflected I_1 mode and a transmitted O_2 mode. This second assumption is used together with boundary conditions to calculate the coefficients T_{12} and R_{11}.

With the reflection and transmission coefficients it is possible to rewrite the Mie theory solution in an infinite sum of a series of modes as in [38]:

$$h_{tot}^{out} = \left[c_m J_m(n_2 kr) + \frac{c_m}{2}(R_{22} - 1)H_m^{(1)}(n_2 kr)\right] + \frac{c_m}{2}\sum_{j=0}^{\infty} T_{12}(R_{11})^j T_{21} H_m^{(1)}(n_2 kr)$$

where h_{tot}^{out} is the total magnetic field outside the sphere.

Fig. 7 shows a diagram of how the modes are being generated starting from the illuminating TM plane wave. Adapted from [38].

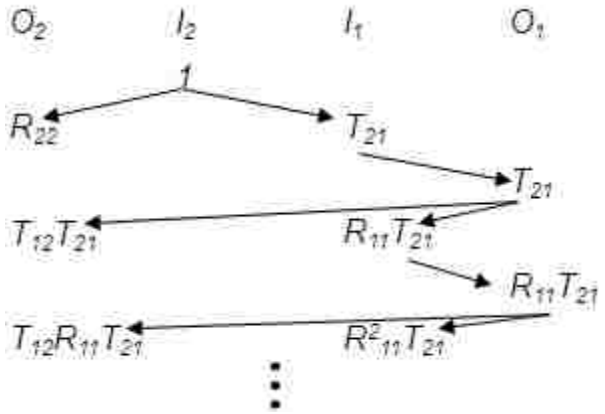

Figure 7: Diagram of the generation of the Debye series components. Each Debye mode determines a component of the total field in terms of transmission and reflection coefficients. Adapted from [38].

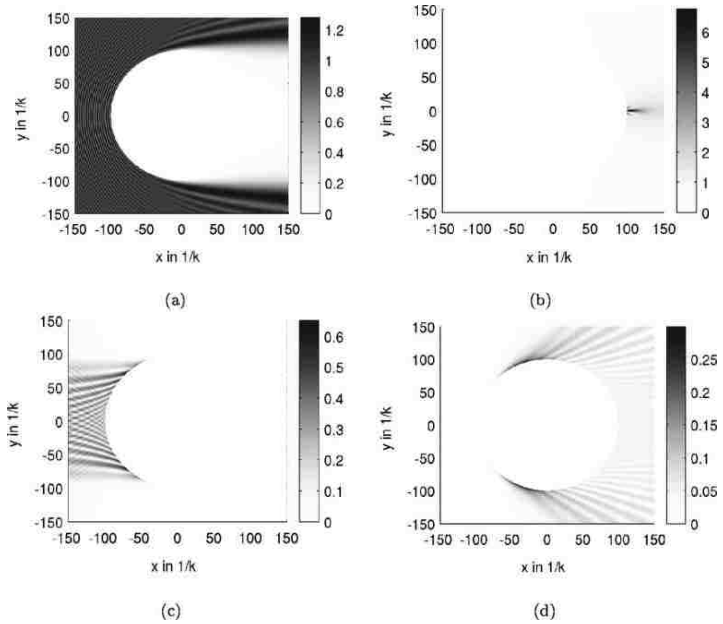

Figure 8: Debye series terms for a sphere with radius a = 100λ and n_1 = 1.78n_2: (a) incidence+R_{22} term, (b) $T_{12}T_{21}$ term, (c) $T_{21}R_{11}T_{12}$ term, and (d) $T_{21}R^2{}_{11}T_{12}$ term. Source: Reference [38].

Fig. 8 shows a collection of field envelopes, taken from Ref [38], that correspond to the first four terms in the Debye series. It is evident that the main contributor to the formation of the nanojet is the $T_{12}T_{21}$ term; this Debye series component is generated by two consecutive refractions. Also, the rest of the components of the series, except for the incident field plus R_{22}, are affected by the reflection coefficient R_{11}. This demonstrates the necessity of employing a sphere of low *n* with respect the background medium in order to generate a photonic nanojet. As the reflection coefficient R_{11} becomes higher, the term $T_{12}T_{21}$ no longer dominates.

3.5 1-D Photon Propagation

One of the goals in the work of this dissertation is to test the hypothesis that the backscattered spectrum resulting from visible-light illumination of a realizable 3-D system involving photonic nanojets can approximate that of a photon propagating and backscattering in a purely 1-D system. The relevance of reproducing this benchmark case resides in the fact that the reflected light in the hypothetical 1-D case is sensitive to *n* fluctuations of any contrast (Δn) and length scale (l_c), including ultra-subwavelength thicknesses. This theoretically unlimited sensitivity of 1-D propagating waves can be understood from different considerations.

The scattering coefficient of the 3-D case is about $(l_c/\lambda)^3$ [40]. In consequence, contributions in the far-field region from inhomogeneities with $l_c < \lambda$ are weighted down as the square of a number that is less than 1 (l_c^2). However, for the 1-D case the scattering coefficient is about (l_c/λ), which makes the contribution from

subwavelength inhomogeneities to decay slower with the size of the inhomogeneity [40].

According to Mesoscopic light transport theory [41]-[47], the backscattered light in a 1-D channel that results from multiple interferences of light waves reflected from weak *n* fluctuations is non-self-averaging (the standard deviation relative to the mean increases with the size of the system) for all l_c scales. Therefore the backscattered fields in a purely 1-D case are sensitive to any l_c of low refractive index fluctuations, making it possible to detect features of any arbitrary size in the far-field.

In a true 1-D system, there is no segmentation of the space domain into near-field or far-field regions because the spatial dependence of the time-domain 1-D Green's function ($\bar{G}^{(1)}$) is entirely contained in time-retarded Dirac delta functions [48]. This can be expressed as:

$$\bar{G}^{(1)} = \frac{U(\tau)}{2}\begin{bmatrix} [\delta(\mathbf{z}+c\tau)+\delta(\mathbf{z}-c\tau)] & -\eta[\delta(\mathbf{z}+c\tau)+\delta(\mathbf{z}-c\tau)] \\ -\eta^{-1}[\delta(\mathbf{z}+c\tau)+\delta(\mathbf{z}-c\tau)] & [\delta(\mathbf{z}+c\tau)+\delta(\mathbf{z}-c\tau)] \end{bmatrix}$$

where:

$\mathbf{z} = z - z'$

U(τ) is the unit step function

$$U(\tau) = \begin{cases} 0, & t < t' \\ 1, & t > t' \end{cases}$$

δ is the Dirac delta function

$$\delta(z) = \begin{cases} +\infty, & z = 0 \\ 0, & z \neq 0 \end{cases}$$

τ is the time increment between the initial and present time

η is the intrinsic impedance of the homogeneous medium

In such an ideal 1-D system, an illuminated ultra-subwavelength-thin dielectric film would locally generate a high-spatial-frequency electromagnetic field distribution which would propagate to infinity with zero attenuation or spreading. Information regarding the existence and characteristics of such a film could, in principle, be obtained at any remote location.

Chapter 4

Probing Flat Dielectric Slabs

4.1 Introduction

This Chapter documents FDTD models involving homogeneous and inhomogeneous dielectric targets with flat surfaces that are illuminated by the elongated photonic nanojet reported in Section 3.3. First, the analysis procedure for the backscattered light is provided. Although the response in both the time and frequency domain is analyzed, the magnitude of the backscattered cepstrum is found to be the most useful in characterizing the targets. Comparisons between 3-D models and their equivalent 1-D case are provided to demonstrate the ability of photonic nanojets to provide approximately 1-D wave propagation in 3-D. Several configurations of dielectric targets are considered to test the effect of different target features like thickness, transverse area, inhomogeneity dimensions, *n* contrast, etc, on the cepstral curve. All of the 1-D and 3-D cases considered in this Chapter are modeled using the scattered field FDTD formulation.

4.2 Cepstrum

The term “cepstrum” was coined by Bogert et al. [49] in 1963 to refer to the result of taking the Fourier Transform (FT) of the logarithm of the spectrum. It is formed by reversing the order of the first four letters in the word “spectrum”. This signal processing method is useful because it permits an analysis of the rate of change and periodicity of the spectrum over the complete frequency range of interest. As will be shown later in this Chapter, it is by analyzing the periodicity of the FDTD-

computed backscattered spectrum that the features of the sampled target can be unambiguously identified, even the ultra-sub-wavelength inhomogeneities having low *n* contrast with the dielectric slab.

The cepstra has been applied over a broad class of applications like speech processing, acoustics, communications, image processing, and more recently is being used in biology.

Power cepstrum was initially defined in [49]. It may be defined as

$$cepstrum = |\boldsymbol{F}\{log(|\boldsymbol{F}\{f(t)\}|^2)\}|^{\mathbf{2}}$$

where $\boldsymbol{F}$ denotes the Fourier transform. But there are many different definitions of cepstrum depending on the nature of the signal to analyze or the information that is desired to depict from it. For example, there exists the short-time cepstrum [50], complex cepstrum [51], and many others.

In this dissertation, the cepstrum is defined as the Discrete Fourier Transform (DFT) applied to the magnitude of the spectrum. Algorithmically this is expressed as:

$$f(t) \rightarrow DFT \rightarrow abs() \rightarrow DFT \rightarrow cepstrum$$

As shown in Fig. 9 this definition results in a simpler cepstral curve compared to the power cepstrum definition, which makes it easier to identify inhomogeneities inside the dielectric slab.

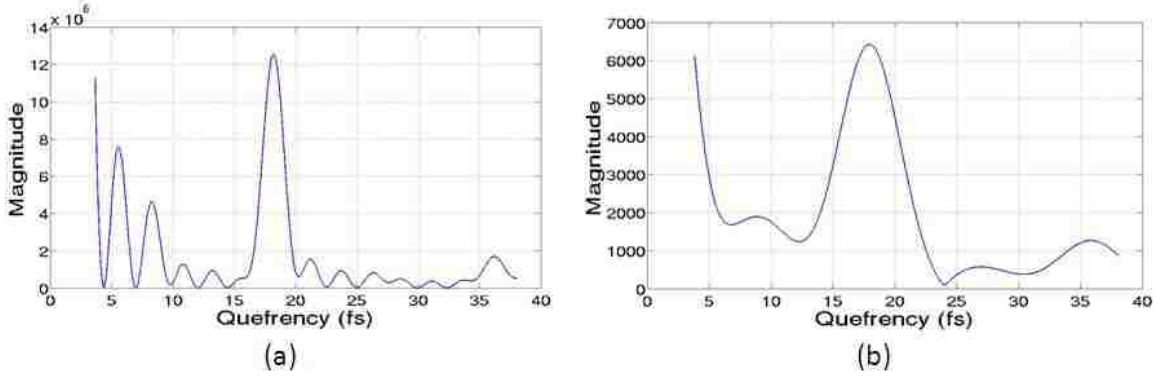

Figure 9: Comparison of cepstra of FDTD-computed backscattered light from a representative nanojet illuminated dielectric target. Cepstra obtained based on: (a) power cepstrum, (b) definition adopted in this dissertation.

Note that the independent variable in the cepstral curves has units of seconds, but these curves exist neither in the frequency nor time domain. The new domain was termed “quefrency” and the integer multiple of the fundamental quefrency was termed “rahmonics” [49]. In a similar manner as for the coining of the word “cepstra”, these terms were formed by altering the order of the initial letters of their corresponding terms that represent their counterpart in frequency domain.

4.3 Homogeneous Slabs

Fig. 10 illustrates the geometry of the pure scattered-field 3-D FDTD model of the elongated photonic nanojet shown in Fig. 5 interacting with a 2-μm dielectric cube of refractive index n = 1.3 centered upon the nanojet. In this section the cube is assumed to be homogeneous, and the study of inhomogeneities is left for Section 4.4. The grid resolution is 25 ηm in the three Cartesian directions, and a convolutional perfectly matched layer absorbing boundary condition prevents numerical wave reflections from the outer grid boundary [28]. For each simulation case, the backscattered time-waveform is recorded 1.25 μm on the incident side of the microsphere for subsequent cepstral post-processing. The layered

microsphere is illuminated with an x-polarized plane-wave Gaussian pulse modulated at λ = 500 ηm.

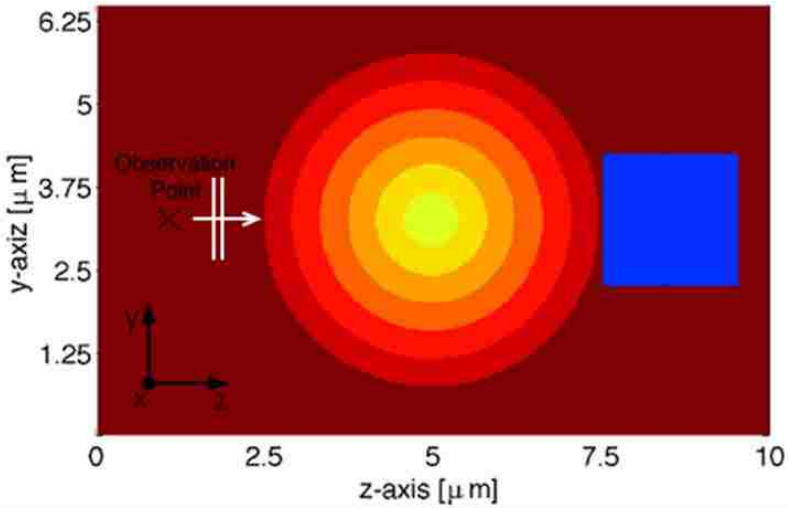

Figure 10: 2-D slice of the geometry of a 3-D six-layer radially graded dielectric microsphere exciting the 2-μm test homogeneous dielectric cube.

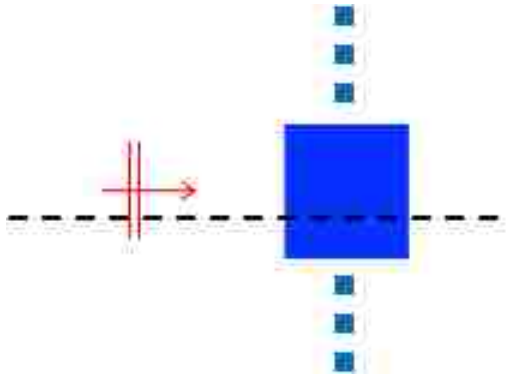

Figure 11: Example illustration of a homogeneous slab analogous to the cube of Fig. 10. The dashed line represents the 1-D FDTD grid. The slab is illuminated via a plane wave, and the slab is infinite in the transverse directions to the incident plane wave.

To permit a comparison between the 3-D case (Fig. 10) and a 1-D case, a pure scattered-field 1-D FDTD model as shown in Fig. 11 at a 25 ηm grid resolution is constructed having a 2-μm-thick dielectric slab of refractive index n = 1.3 of infinite transverse area illuminated. This slab is assumed to be homogeneous and is illuminated by a plane wave at normal incidence. Also, the reflected field time-waveform is similarly recorded 1.25 μm on the incident side of the dielectric slab for subsequent cepstral post-processing.

It is important to note that the 3-D and 1-D FDTD models studied herein have fundamentally different levels of complexity. For the 1-D model, the dielectric slab is normally and directly illuminated by a simple plane wave arriving from an infinite free-space region. Both the slab and the impinging wave extend infinitely without change in the transverse directions. On the other hand, for the 3-D model, a graded dielectric microsphere is interposed between the illuminating plane wave and the dielectric cube target. Electromagnetic wave propagation is computed in all possible directions within and around the dielectric microsphere, and within and around the dielectric cube. Any level of agreement between the results of these two widely disparate models would support the 1-D interaction hypothesis.

The first study involves a comparison of the backscattered response of the 3-D nanojet-illuminated n = 1.3 homogeneous cube and the 1-D plane-wave-illuminated n = 1.3 homogeneous slab. In the first step of the post-processing, a DFT is applied to the backscattered field time-waveform of each model to generate the backscattered spectra. This step is followed by a second DFT operating upon the magnitude of the backscattered spectra, which yields the backscattered cepstra.

Fig. 12 compares the cepstra obtained in this manner for the 3-D nanojet-illuminated n = 1.3 homogeneous cube and the 1-D plane-wave-illuminated n = 1.3 homogeneous slab. A strong correlation between the two sets of results is observed. This is our first indication that the photonic nanojet is indeed providing a nearly one-dimensional interaction with the 3-D dielectric cube.

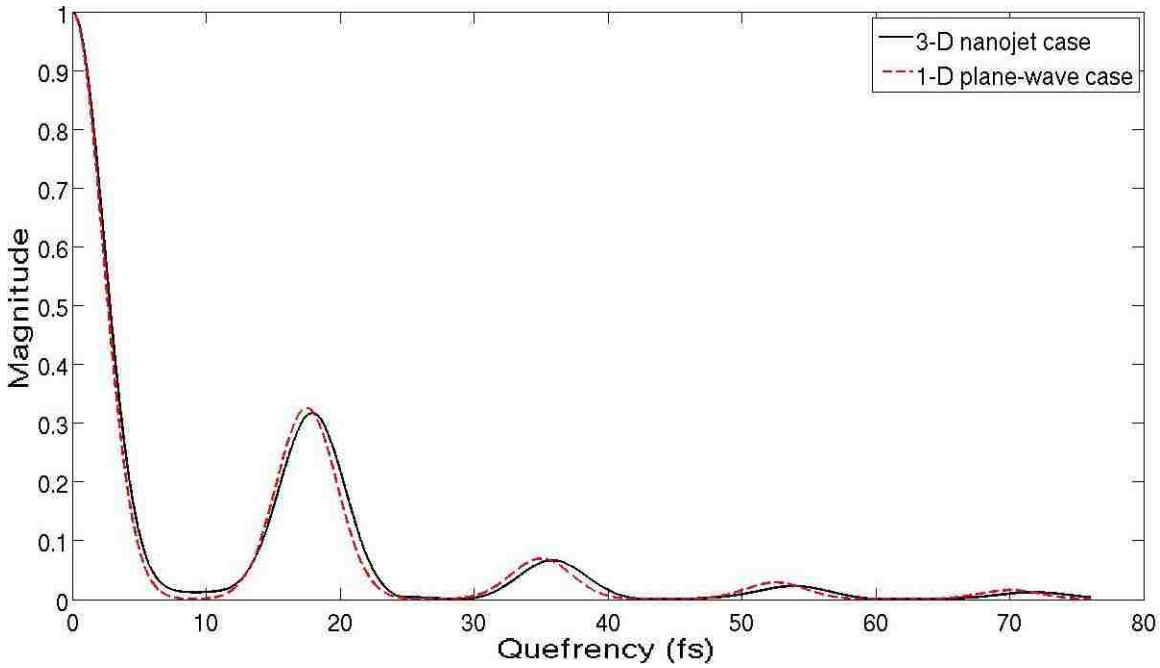

Figure 12: Comparison of the cepstra of the 3-D nanojet-illuminated n = 1.3 homogeneous cube and the 1-D plane-wave-illuminated n = 1.3 homogeneous slab. The magnitude is normalized by the maximum value.

By considering two additional cases of homogeneous dielectric targets wherein the variation is the thickness of the slab, it is possible to identify a specific trend in the cepstral curve. The position of the first rahmonic peak shifts towards higher values along the frequency axis for an increase of dielectric thickness. This is illustrated in Fig. 13, which shows results obtained from the 3-D model. The two new targets maintain the same transverse area and n as the original case, but the thickness in one case is 1.5 μm and in other is 3.0 μm. The third case is the same considered previously (2 μm thick).

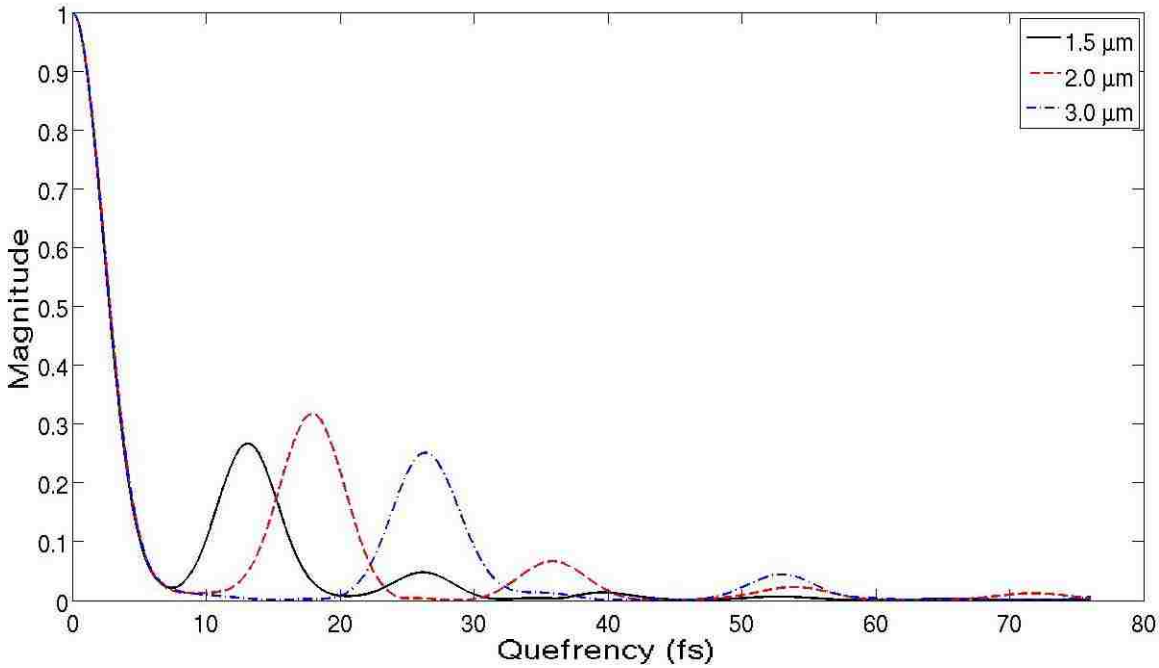

Figure 13: Dependence of the position of first rahmonic peak with dielectric slab thickness for values of 1.5, 2.0 and 3.0 µm. The magnitude is normalized by the maximum value.

These results suggest that there exists a direct correlation between the position of the rahmonic peak on the independent axis and the electrical thickness of the dielectric slab. By analyzing the signal in both time and frequency domain it will be shown that this is actually the case.

Fig. 14 shows the FDTD-computed backscattered light in the time domain. This signal was recorded at 1.25 µm from the layered microsphere that generates the impinging photonic nanojet on the dielectric slab of 2 µm thickness. The signal is comprised of a leading modulated Gaussian pulse and a second echo. The early pulse corresponds to backscattered light from the illuminated surface of the target; the retarded scaled-down copy emerges as backscattering from the shadow side surface of the target.

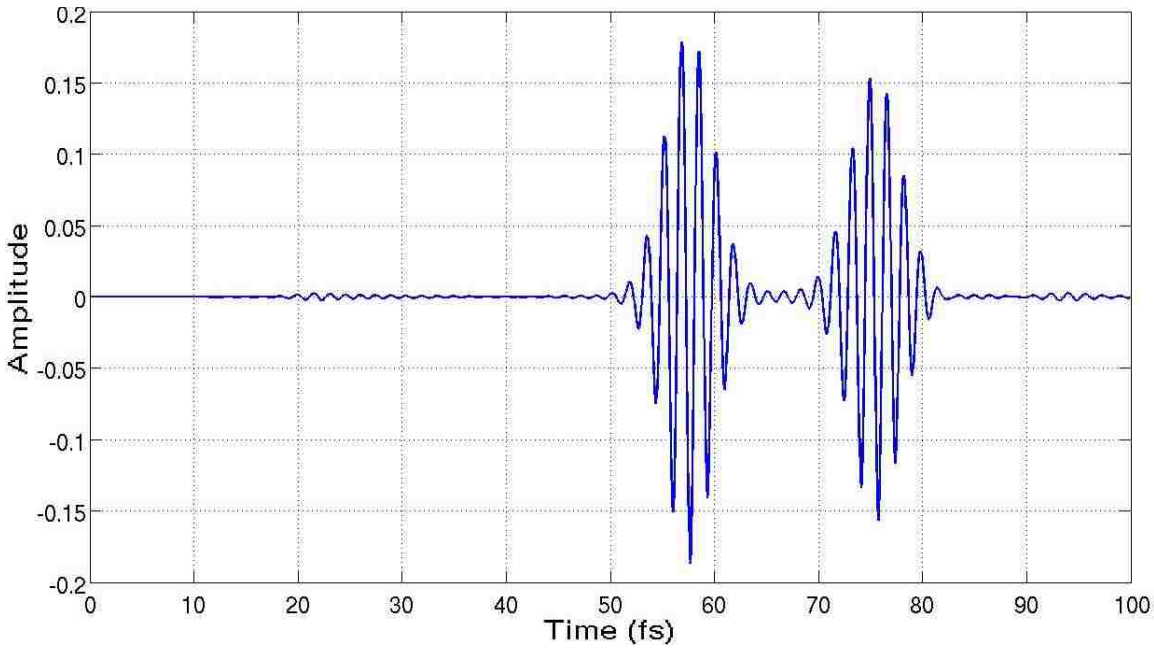

Figure 14: Recorded backscattered light in time domain from the 2 μm thick dielectric slab illuminate by the elongated photonic nanojet.

This kind of signal can be represented as

$$x(t) = s(t) + \alpha s(t - \tau) \tag{4.1}$$

where α accounts for the scaling down of the echo with respect to the leading pulse and τ is the delay between copies. The magnitude of the spectra of such a signal is given by

$$|X(f)| = |S(f)|\sqrt{1 + \alpha^2 + 2\alpha\cos(2\pi\tau f)} \tag{4.2}$$

It is evident from equation (4.2) that the magnitude of the spectrum of a signal with one simple echo has an envelope determined by the magnitude of the spectrum of the original pulse that modulates a periodic function of fundamental frequency τ. To illustrate this point, the spectrum of the signal in Fig. 14 is shown in Fig. 15.

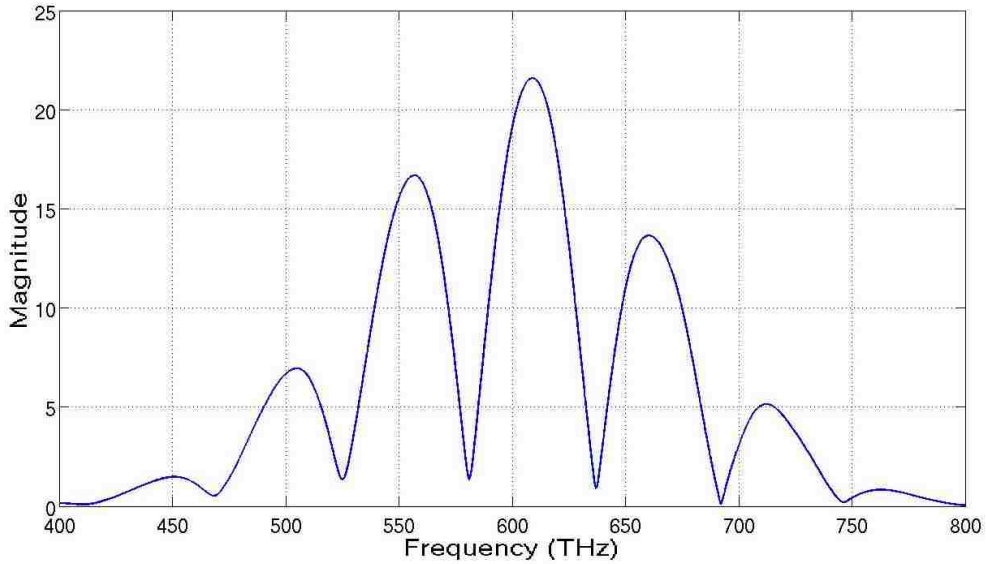

Figure 15: Magnitude of the spectrum for backscattered light from the 2 μm thick dielectric slab illuminate by the elongated photonic nanojet. The curve is composed by a periodic function multiplied by a Gaussian envelope.

Thus, the result of applying a DFT on the magnitude of the spectrum shows a peak positioned at τ on the independent axis. For this particular case, Fig. 13 shows that the first rahmonic peak is positioned at 17.9 fs, which is the same delay that is observed between the leading pulse and the second echo in Fig. 14. It is easy to check that for a 2μm thick dielectric of n=1.3, the round trip takes 17.4 fs, this agrees satisfactorily with the modeling results.

Further analyzing these results, for a fixed thickness of the dielectric slab and n contrast with respect to the background medium, the transverse area of the slab determines the absolute values of the rahmonic peaks but their position along the independent axis stays fixed. The backscattered cepstrum from dielectric slabs having transversal widths of 0.75 and 1.5 μm were compared against the 2 μm cube. As expected, the wider the target the more energy gets backscattered. Interactions of the elongated photonic nanojet with the edges and lateral faces of

the dielectric slab do not induce additional rahmonic peaks. This is illustrated in Fig. 16.

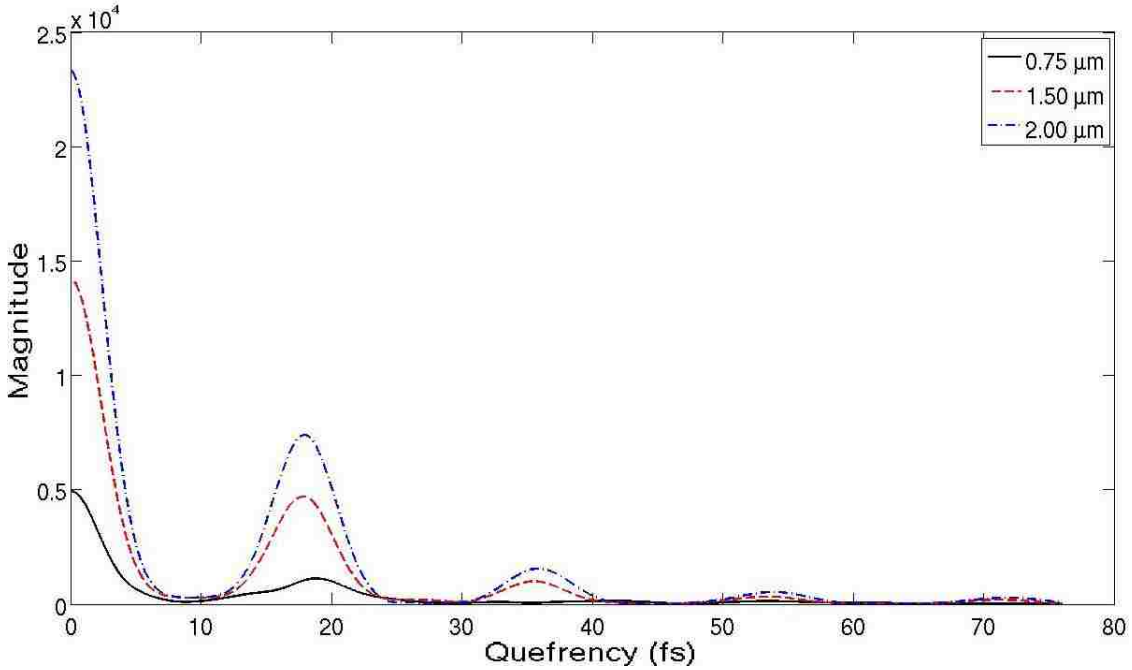

Figure 16: Dependence of magnitude of rahmonic peaks with transverse area of homogeneous dielectric slab. The illuminated square sides considered are 0.75, 1.50 and 2.0 µm. The magnitude is in absolute values.

The distortion of the rahmonic peak at 18 fs that corresponds to the 0.75 µm case is induced by the backscattering from the layered microsphere. In this case the backscattering from the target is low enough to become comparable with that of the sphere. The cepstral curve begins to converge for values of transversal width greater than 3.0 µm.

Referring to Equation (4.2), it can be seen that the DC component of the periodic function inside the square root is affected by $1 + \alpha^2$ while the periodic component is affected by 2α. This means that although the position on the frequency axis of the first rahmonic peak (of the cepstrum curve) indicates the time delay between the main pulse and the second echo, the ratio of the intersection of the cepstral

curve with the vertical axis (peak at 0 fs) to the maximum value of the first rahmonic peak does not equal the ratio of the pulses in time domain (α). In fact, both the intersection of the cepstral curve with vertical axis and maximum value of the rahmonic peak encode information regarding α.

To conclude this section, Fig. 17 shows the dependence of the cepstral curve on *n* of the dielectric target. As expected, with higher *n* the absolute value of the rahmonic peaks increase. It is also consistent that the delay of the echo from the shadow side surface increases with *n* because the physical dimensions of the dielectric are maintained constant. The enhanced multiple reflections induced by a higher *n* contrast of the dielectric cube with the background medium induces significant additional echoes. This causes an additional peak to arise at slightly higher quefrency values from the peak that indicates the delay of the echo from the shadow side of the target.

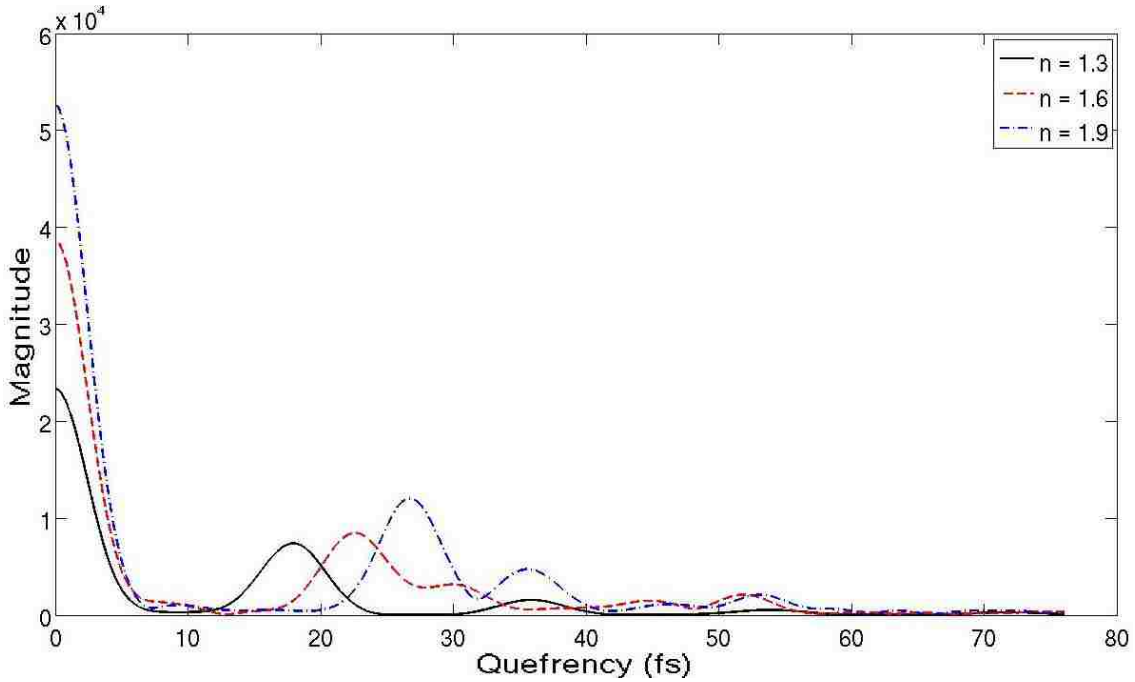

Figure 17: Dependence of cepstral curve with refractive index of homogeneous dielectric for *n* = 1.3, 1.6 and 1.9. The magnitude is in absolute values.

4.4 Embedded Thin Layers

Fig. 18 and 19 show the geometry of the pure scattered-field FDTD models of the 3-D and 1-D cases, respectively, but now with an inhomogeneity embedded within the target. These modeling cases are the same as those considered in the previous section except that the 2 μm cube has a 25-ηm-thin (λ/20) film-like inhomogeneity of index n = 1.4 embedded at its center in the direction of photon propagation. Initially the transverse width of the layer is assumed to be the same as that of the dielectric slab (W = 2 μm).

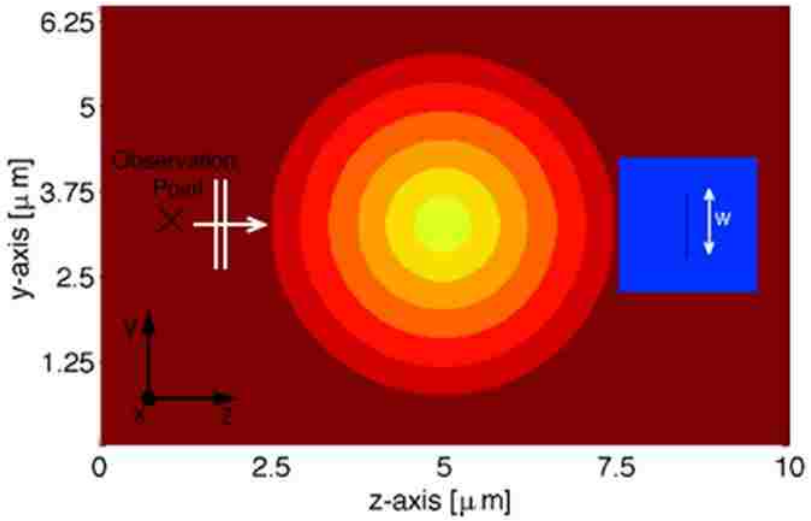

Figure 18: 2-D slice of the geometry of a 3-D six-layer radially graded dielectric microsphere exciting the 2-μm test dielectric cube, here shown with the 25-ηm-thin film-like inhomogeneity embedded at its center in the z direction.

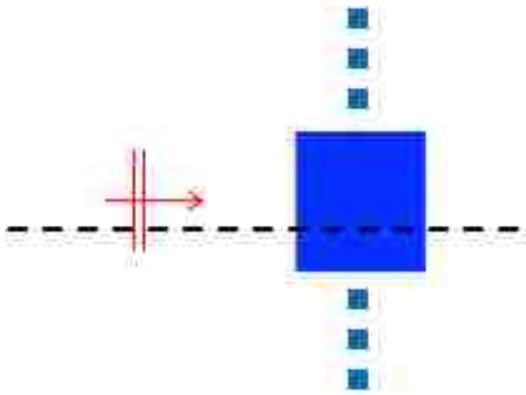

Figure 19: Example illustration of a slab having a dielectric thin film at its center, in an analogous manner to the cube of Fig. 18. The dashed line represents the 1-D FDTD grid. The slab is illuminated via a plane wave, and the slab is infinite in the transverse directions to the incident plane wave.

Cepstra curves resulting from the above cases wherein there is a 25 ηm thin film-like inhomogeneity at the center of the n = 1.3 cube are shown in Fig. 20. Data corresponding to the 1-D model of the homogeneous target is also included to emphasize the effect of the inhomogeneity. Again, there is a strong correlation between the results obtained from the 1-D and 3-D models. The beginning of the curve as it increases to its max at quefrency = 0 is omitted to better illustrate the change with respect to the homogeneous slab case.

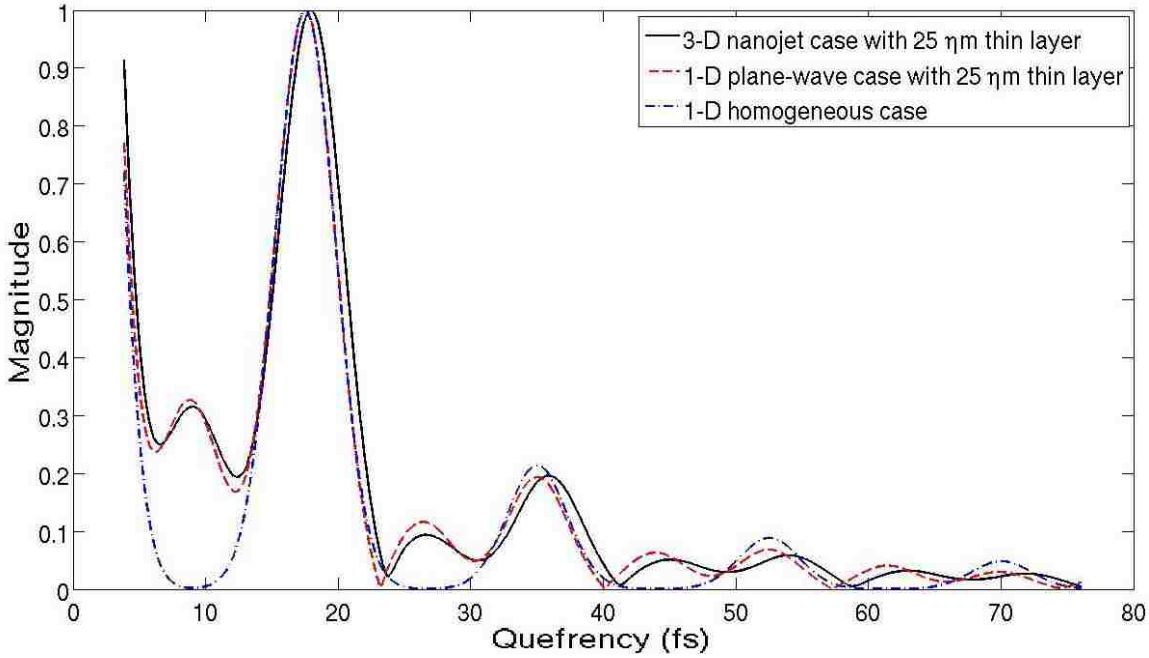

Figure 20: Comparison of the cepstra as in Fig. 12, but now both the 3-D nanojet-illuminated cube and the 1-D plane-wave-illuminated slab have a 25-ηm (λ/20) n = 1.4 film-like inhomogeneity embedded at their midpoint depths. For convenience, the 1-D plane-wave illuminated homogeneous cepstrum is also shown.

Comparing the results of the inhomogeneous dielectric with those of the homogeneous slab, it can be seen that embedding the 25-ηm n = 1.4 film at a midpoint depth within the cube and the slab causes a second set of rahmonic peaks to arise. These new peaks occur between the original rahmonic peaks, and are of significant amplitude. Furthermore, there is an excellent agreement of

the new peaks of the 3-D nanojet-illuminated cube and the 1-D plane-wave-illuminated slab at the lowest quefrencies. While this agreement diminishes with increasing quefrency values, it remains significant up to the third new peak.

In order to investigate the effect of different inhomogeneity parameters on the cepstral curve, some cases of increased thicknesses with respect the initial configuration of this section were analyzed. Fig. 21 shows how the minor rahmonic peak induced by the inhomogeneity increases with thicker layers. However there is a limit where this trend breaks down and the peak decreases.

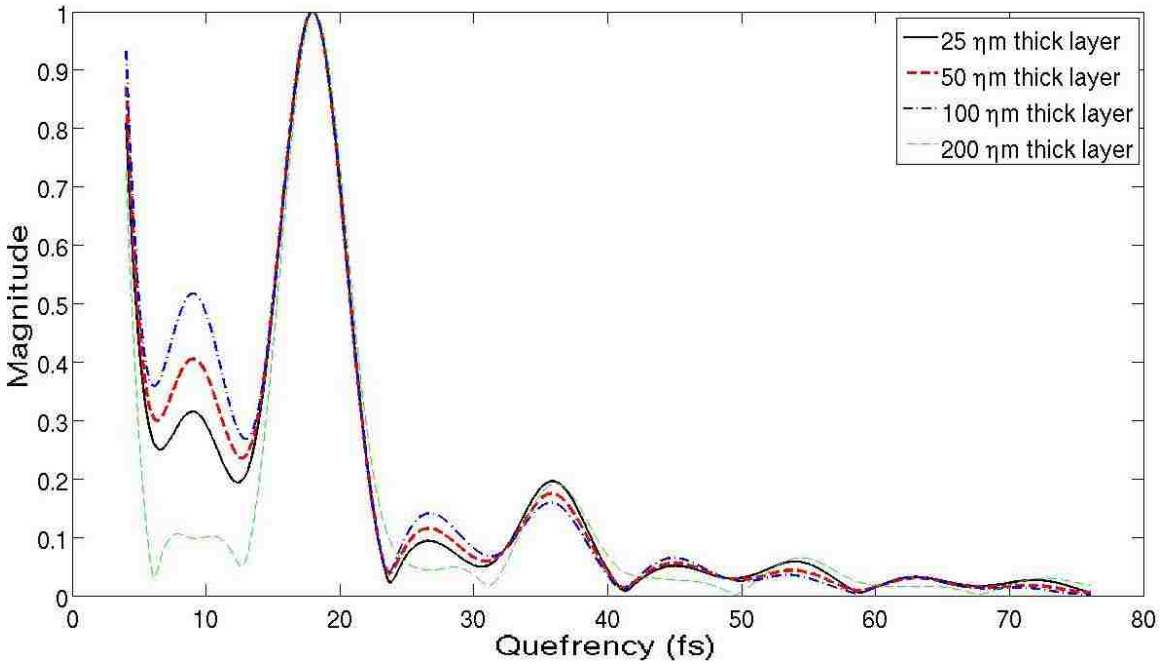

Figure 21: Dependence of magnitude of minor rahmonic peaks with inhomogeneity thickness. Cepstral curves correspond to 25, 50, 100, or 200 ηm thick layers. The magnitude is normalized with the magnitude of the major rahmonic peak.

In fact for thicker layers than shown in Fig. 21 the cepstral curve converges slowly towards the basic shape that corresponds to a homogeneous slab having a refractive index equal to that of the inhomogeneity, but in these cases the thickness is no longer subwavelength. The breakdown of this trend can be understood by considering the backscattered signal in the time domain. For the

thinnest layers, the backscattered fields from both surfaces of the layer are very close to being in phase. Therefore the interference results in a very close approximation to a retarded and scaled down copy of the leading pulse, as it was assumed to be in Equation (2.1). However as the thickness increases the interference is no longer constructive for all frequency components.

Fig. 22 illustrates cepstral results for a 25-ηm thin film embedded at the dielectric cube's midpoint in the z-direction and having a transverse width of 500, 750, 1500, or 2000 ηm. In a similar manner as for the homogeneous dielectric, for transversely very narrow areas of the inhomogeneity, the rahmonic peaks corresponding to the delay of the echo from the thin layer diminish in amplitude. In consequence, the results converge to that of the homogeneous dielectric. However, note in particular in Fig. 22 that the 1500 ηm wide film yields an increase in the second set of peaks with respect to those obtained with the 2000 ηm wide film. This amplitude increase for the 1500-ηm case is found to result from the interaction of the nanojet with the combination of the edges of the thin film and the longitudinal faces of the n = 1.3 dielectric slab. This is shown in Fig. 23, wherein we see that side lobes are generated due to the relatively short transversal width of the dielectric cube relative to the FWHM of the photonic nanojet. In fact, when the 2 μm dielectric cube is widened to 10 μm (maintaining a thickness of 2 μm), the side lobes are no longer generated. As a result, we also find that for this 10-μm wide case, the amplitude of the second set of rahmonic peaks corresponding to the thin film inhomogeneity progressively diminish in

amplitude as the thin film is progressively narrowed in the transverse direction (instead of seeing a rise for the 1500 ηm-wide case).

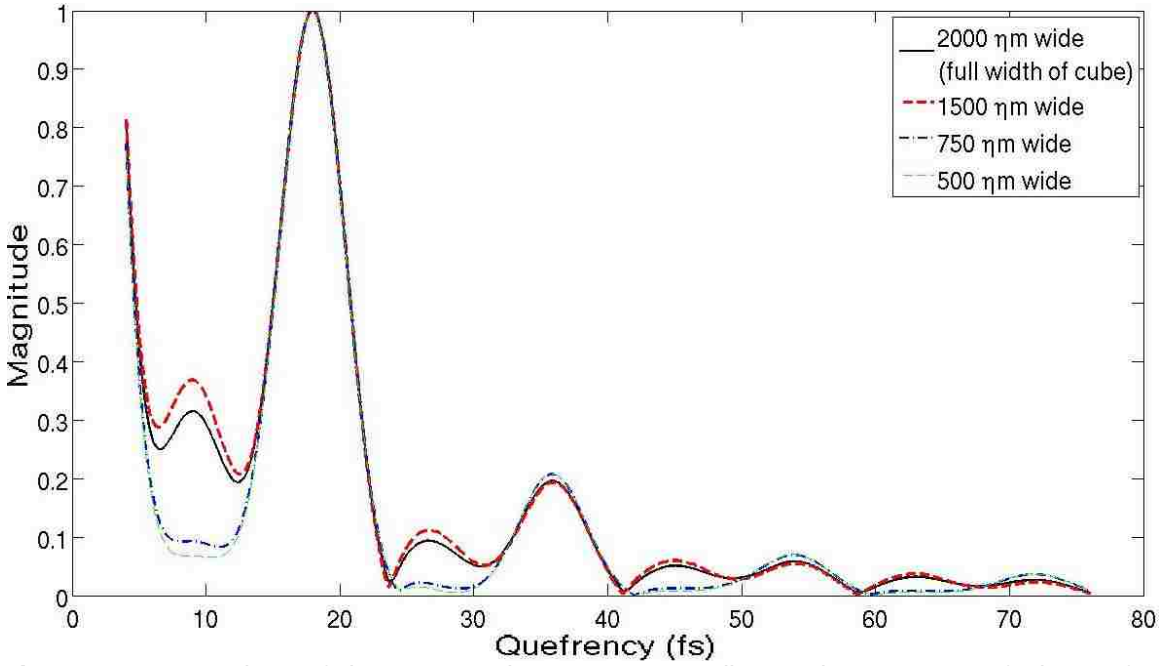

Figure 22: Comparison of the 3-D nanojet cepstra according to the geometry of Fig. 18 for transverse widths of the 25-ηm thin inhomogeneity at 500, 750, 1500 and 2000 ηm. The magnitude is normalized.

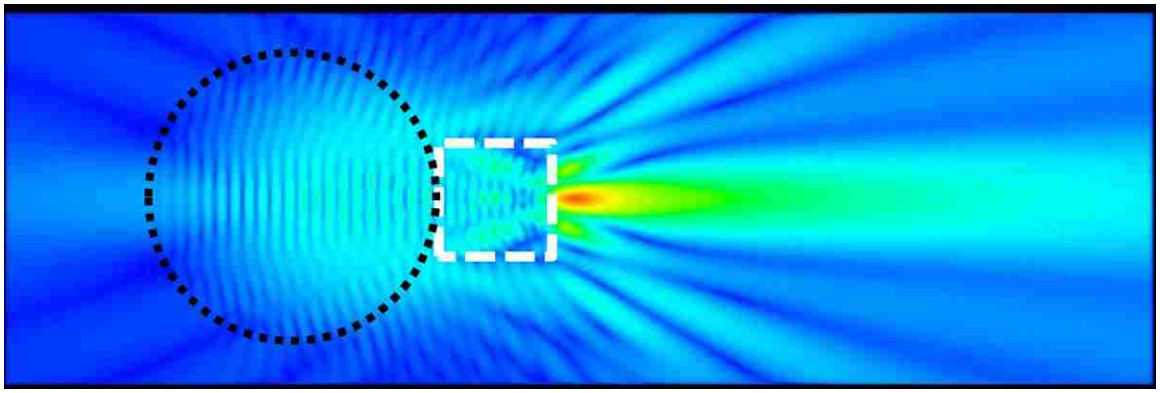

Figure 23: Visualization of the layered dielectric sphere generating a photonic nanojet with a 2 μm dielectric cube located in the path of the nanojet. The incident wave is polarized along the x-axis and propagates along the z-axis, using the same coordinate system as defined in Fig. 18.

Note that these results were obtained using the elongated nanojet, which detects inhomogeneities at greater longitudinal distances at the expense of illuminating a wider transverse area of the object. Given the above observed interaction of the photonic nanojet with the edges of the thin film and longitudinal sides of the

n=1.3 dielectric cube, it may be advantageous to choose a narrower photonic nanojet to probe objects of relatively small transverse and longitudinal dimensions. The traditional (non-elongated) photonic nanojet has a transverse beamwidth at less than the classical diffraction limit, as small as ~λ/3. Thus, it may be used to probe shallower but also narrower transverse regions.

Next, the dependence of the cepstral curve with the position of the thin layer within the dielectric slab is also investigated. Fig. 24 shows results for a 25 ηm thick layer of *n* = 1.4 located at distances of 1000, 750, and 125 ηm towards the photon propagation direction from the illuminated surface of the *n* =1.3 dielectric cube which size is 2 μm. It can be seen that the minor peak tends to vanish as the inhomogeneity approaches the illuminated surface.

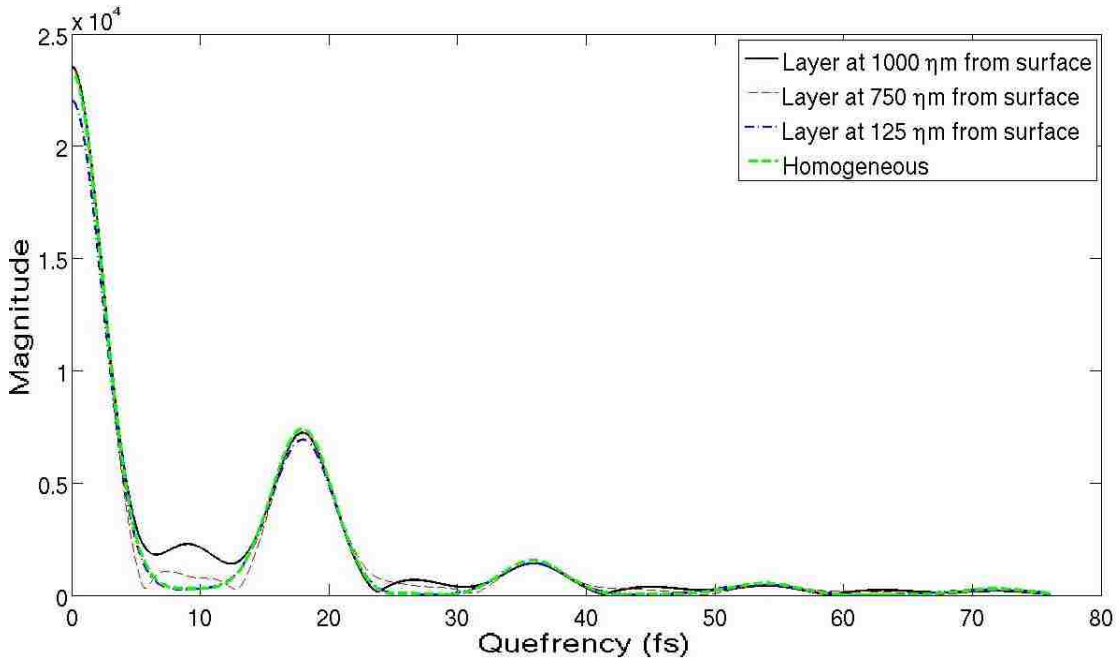

Figure 24: Comparison of minor peak magnitude for inhomogeneities located at 125, 750, and 1000 ηm from the illuminated surface. For convenience, the homogeneous case is included. The magnitude is in absolute values.

The reason that the minor peak vanishes is the echo from the thin layer begins to be overlapped and overwhelmed by the higher-amplitude backscattered light

from the illuminated front surface of the dielectric slab as the layer's position approaches the surface. Therefore the signal in the time domain is no longer a train of delayed and scaled down copies of the original pulse, but it is a partial interference of the first two pulses followed by a third pulse that corresponds to reflections from the shadow side of the dielectric slab. In order to ensure that the minor peak is observable in the cepstral curve, the inhomogeneity must be located at a large enough distance from the surfaces of the dielectric slab in such a way that the round trip between the slab and inhomogeneity interfaces allows for the complete pulse width to fit in between echoes without interferences. It is important to note however, that the information regarding the presence of the inhomogeneity is not lost. In fact, referring to Fig. 24, while the cepstral curve converges towards the homogeneous case in the neighborhood of 10 fs, both the max at quefrency = 0 and the peak located at 17.9 fs diminish beyond the homogeneous case. This reduction is more significant at 0 fs.

Considering the results up to this point, it may be expected that if multiple layers are embedded within the dielectric slab then one minor peak per layer should arise in the cepstral curve in between the vertical axis and the peak that indicates the delay of backscattering from the shadow side of the slab. In other words, there should be a minor peak per layer in between the peaks that correspond to the homogeneous slab case. This is actually the case *provided that the gap between interfaces is far apart enough to avoid interference between different backscattered pulses*. Fig. 25 shows results for 2, 3 and 4 layers embedded within the dielectric slab. Because the gap from dielectric slab surface to

inhomogeneity and between inhomogeneities was kept constant (1 μm), the total thickness of the dielectric slab varies with number of layers.

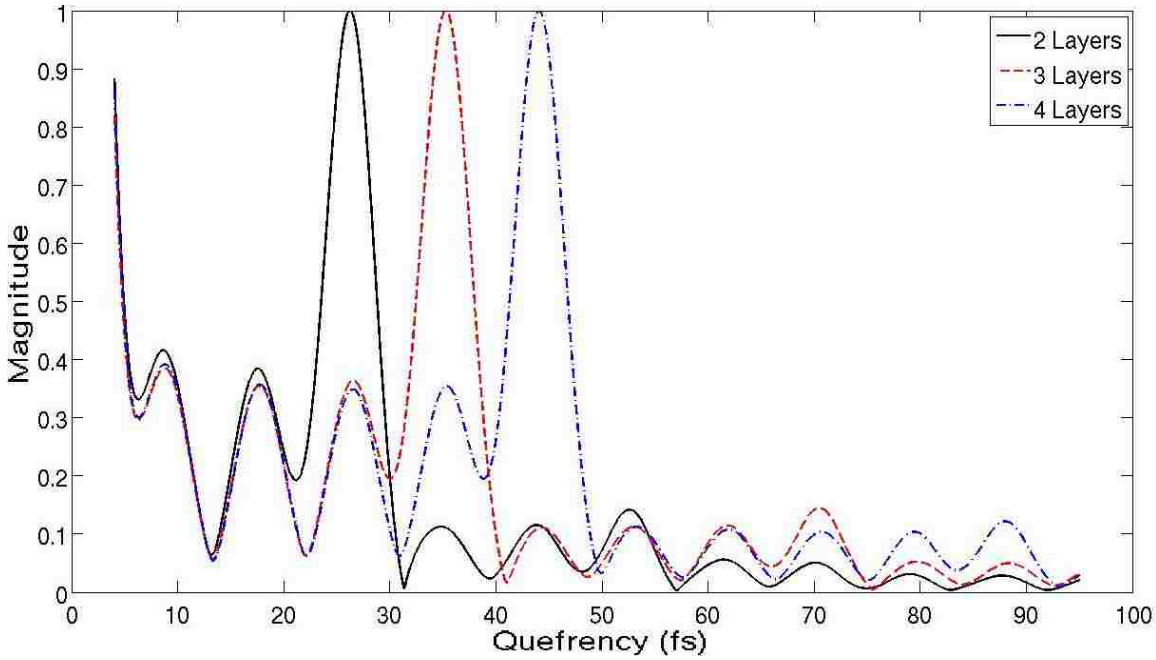

Figure 25: Comparison of cepstral curves for 2, 3, and 4 layers embedded within a dielectric slab. The thickness of the dielectric slab adjusts so that each layer is separated 1 μm from its neighboring layer(s) / dielectric surface. The magnitude is normalized to the major peak.

The major rahmonic peak at a magnitude of 1.0, which indicates the delay of the backscattered pulse from the shadow side surface of the slab, appears positioned at quefrency values equal to 26.36, 35.41, and 44.14 fs for the cases of 2, 3 and 4 embedded inhomogeneities respectively. In each cepstral curve, the minor peaks that appear at lower quefrency values than their corresponding major peak are induced by backscattering from the inhomogeneities.

By generalizing equation (4.1) to have n_t number of echoes

$$x(t) = s(t) + \alpha_1 s(t-\tau_1) + \alpha_2 s(t-\tau_2) + \alpha_3 s(t-\tau_3) + \cdots + \alpha_{n_t} s\left(t-\tau_{n_t}\right),$$

$$\tau_1 < \tau_2 < \tau_3 < \cdots < \tau_{n_t} \tag{4.3}$$

with each $\tau_i - \tau_{i-1}$ being high enough to avoid interference between copies, the magnitude of the spectrum results in

$$|X(f)| = |S(f)| \sqrt{1 + \sum_{i=1}^{n_t} \alpha_i^2 + 2\left\{\sum_{i=1}^{n_t} \alpha_i \cos(2\pi\tau_i f) + \sum_{i=1}^{n_t-1} A_i\right\}} \qquad (4.4)$$

Where

$$A_i = \alpha_i\alpha_{i+1}\cos(2\pi[\tau_{i+1} - \tau_i]f) + \alpha_i\alpha_{i+2}\cos(2\pi[\tau_{i+2} - \tau_i]f) + \cdots$$

$$+\alpha_i\alpha_{n_t}\cos\big(2\pi[\tau_{n_t} - \tau_i]f\big)$$

If Equation (4.3) is specialized to have all echoes equally spaced, (which is consistent with the cases considered in Fig. 25) the fundamental frequency of all cosine terms in A_i are an integer multiple of τ. Therefore, only the n_t rahmonic peak in the cepstrum curve encodes information regarding its corresponding α_i. The rest of rahmonic peaks encode information of multiple α's. For example, if in the case of three equally spaced layers the inhomogeneity on the illuminated side of the slab is removed (maintaining the thickness of the slab and position of the other 2 layers), the minor rahmonic peak at 8.59 fs will diminish but not disappear completely due to the effect of the rest of α's. Note that this kind of analysis neglects multiple reflections.

These results offer good evidence that the elongated photonic nanojet used in these studies indeed provides the action of a nearly one-dimensional beam over a significant range of cepstral frequencies. The nanojet allows the high spatial frequencies inherent in the fluctuations of the inhomogeneous near-field to be projected to the far-field in three dimensions in a manner consistent with its

projection of a perturbing nanoparticle to the far-field. Further, a backscattering scheme which emphasizes such a one-dimensional action does indeed provide a means to detect ultra-subwavelength thin, weakly contrasting dielectric features deeply embedded within a surrounding material medium.

Chapter 5

Probing Dielectric Slabs having Rough Surfaces

5.1 Introduction

All the dielectric target cases considered in the previous Chapter are useful in understanding how the basic parameters of a flat dielectric slab such as electrical properties, thickness, transversal area, etc, effect the shape of the cepstral curve and position of its rahmonic peaks. These findings can find practical applications in metrology, inspection of semiconductor material in production lines, and high density optical data disks. However, particularly for microscopy and spectroscopy applications, the interaction of photonic nanojets with rough and curved-surface targets must be considered, since these shapes are often inherent to natural surfaces and biological materials.

The roughness and curvature effect how the incident EM waves are transmitted into the dielectric targets and scattered. It is well known that the effects of the roughness and shape of a surface depends on the λ and the angle of incidence. The present Chapter covers in general two categories of surface roughnesses: (1) checkered square patterns that are predetermined; and (2) pseudo-random patterns. Later, in Chapter 7, the effects of a curved and rough surface, corresponding to the shape of a biological cell, is studied. Comparisons with 1D-FDTD are not provided because it is not possible to model transversal surface roughness and shape variations in a 1-D grid.

5.2 Checkered Square Patterns

In a similar manner as in the previous chapter, the system considered for this study is composed of 2-μm dielectric cube of refractive index *n* = 1.3 centered upon the elongated photonic nanojet. The only difference is that the illuminated surface of the cube has an etched a square checkered surface pattern rather than it being flat. Each square has a transversal side equal to its height (a), as is shown in Fig. 26. The cube is initially assumed to be homogeneous, and in a second case it has embedded at its midpoint a 25-ηm-thin (λ/20) film-like inhomogeneity of index *n* = 1.4. The grid resolution is again 25 ηm. The complete 3D-FDTD grid size is 260X260X800 cells in the x, y, and z Cartesian directions respectively. For each simulation case, the backscattered time-waveform is recorded 1.25 μm on the incident side of the microsphere for subsequent cepstral post-processing.

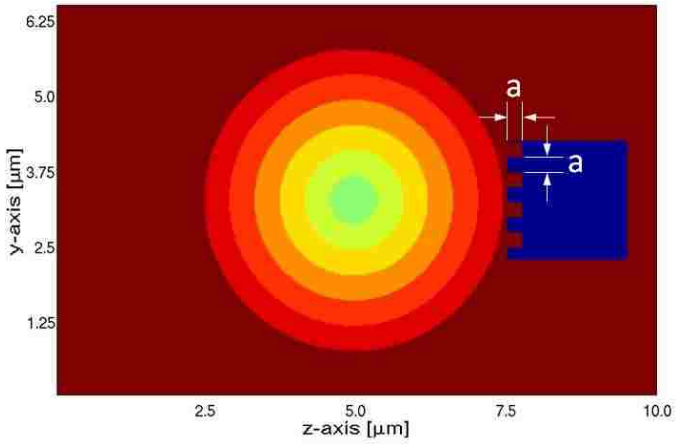

Figure 26: 2-D slice of the geometry of a 3-D six-layer radially graded dielectric microsphere exciting the 2-μm test homogeneous dielectric cube with a square pattern etched at its illuminated surface.

In this initial study on backscattering from rough surfaces, two different roughnesses are considered: a = 25 and 250 ηm. This means, for the 25 ηm roughness case, the slab has a maximum thickness of 2 μm and a minimum

thickness of 1.975 μm. Similarly, for a = 250 ηm, the maximum thickness is 2 μm end the minimum thickness is 1.75 μm. The resulting cepstral curve is shown in Fig. 27. For convenience to later discussion of results, the flat surface case is included.

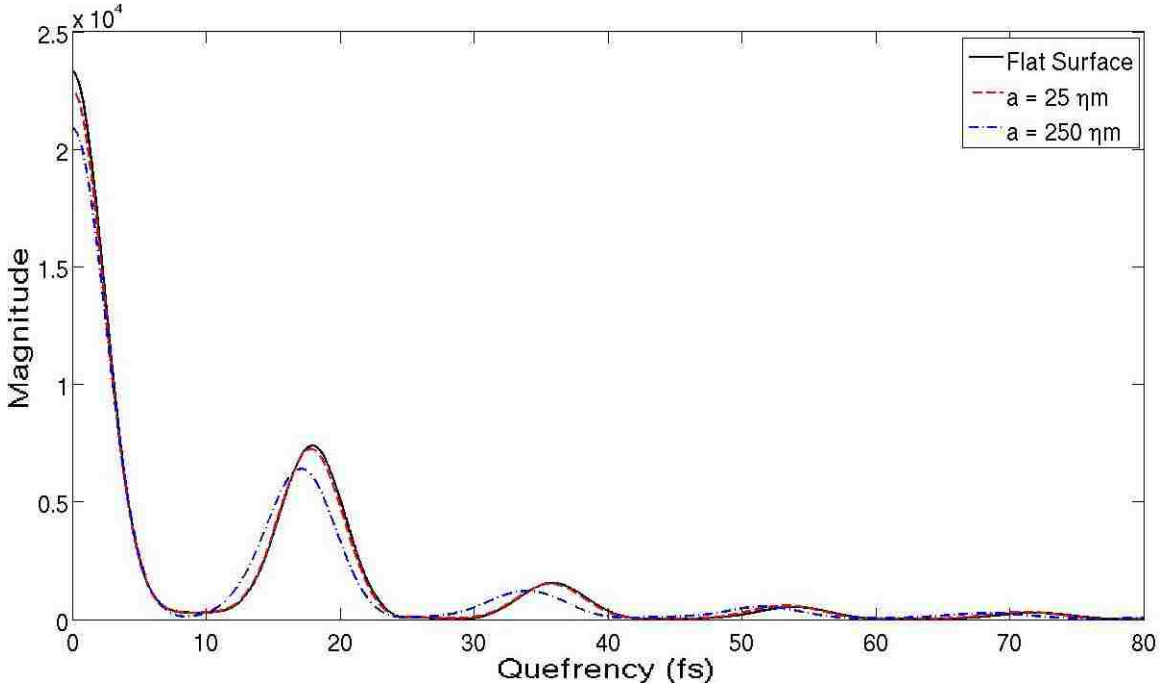

Figure 27: Comparison of the cepstra of the 3-D nanojet-illuminated *n* = 1.3 homogeneous cube with flat surface and squared patterns for a = 25 and 250 ηm. The magnitude is in absolute values.

The selected roughness patterns have two effects on the cepstral curve: first, the absolute magnitude of the rahmonic peaks (and the intersection with the vertical axis) diminishes with roughness; second, the position of rahmonic peaks shift to lower values with roughness. Note that for these predetermined roughness patterns no additional rahmonic peak is induced in the cepstral curve with respect to the homogenous, flat surface case.

When the illuminated surface has a certain roughness, the incident wave is not only reflected in a specular direction, but there is also a scattering component

pointing in different directions due to the edges of the squares and dependent thicknesses with location on the surface. Therefore, the directly backscattered fields diminish with respect to that from a flat surface. This is the cause for the reduction in the maximum magnitude of the rahmonic peaks in the cepstrum curve.

In Fig. 27, the first rahmonic peak that corresponds to the 25 ηm roughness appears shifted 0.114 fs towards lower quefrency values with respect the flat surface case. This is the same position in which the rahmonic peak would be located by solving a flat surface dielectric slab 13.145 ηm thinner than the reference case. Similarly, for the 250 ηm roughness case, the shift in position of the first rahmonic peak is 0.836 fs. This would correspond to a flat slab 96.397 ηm thinner. Because the equivalent flat surface thickness is in between the minimum and maximum heights of the squared surface, for this kind of roughness pattern the photonic nanojet has an averaging effect of the highest and the lowest dielectric thickness with position on its illuminated surface. It is also interesting to see that this elongated nanojet can be sensitive to changes on the surface of the target in the direction of the nanojet that are on the order of λ/20.

For a second case, the dielectric slab has embedded a 25-ηm-thin film-like inhomogeneity of index n = 1.4. Fig. 28 shows results corresponding to the 250 ηm square pattern surface. Here, because the maximum field intensity of the elongated photonic nanojet occurs about 5 μm away from the shadow side of the layered microsphere (refer to Fig. 5), the illuminated surface of all the slabs of

Fig. 28 are shifted a distance (d) of 5.1 μm away from the surface of the microsphere. This adjustment of the dielectric target position with respect to the sphere is done to test the enhancement of the contrast of the minor rahmonic peak that normally arises with the presence of the inhomogeneity with respect the major rahmonic peaks.

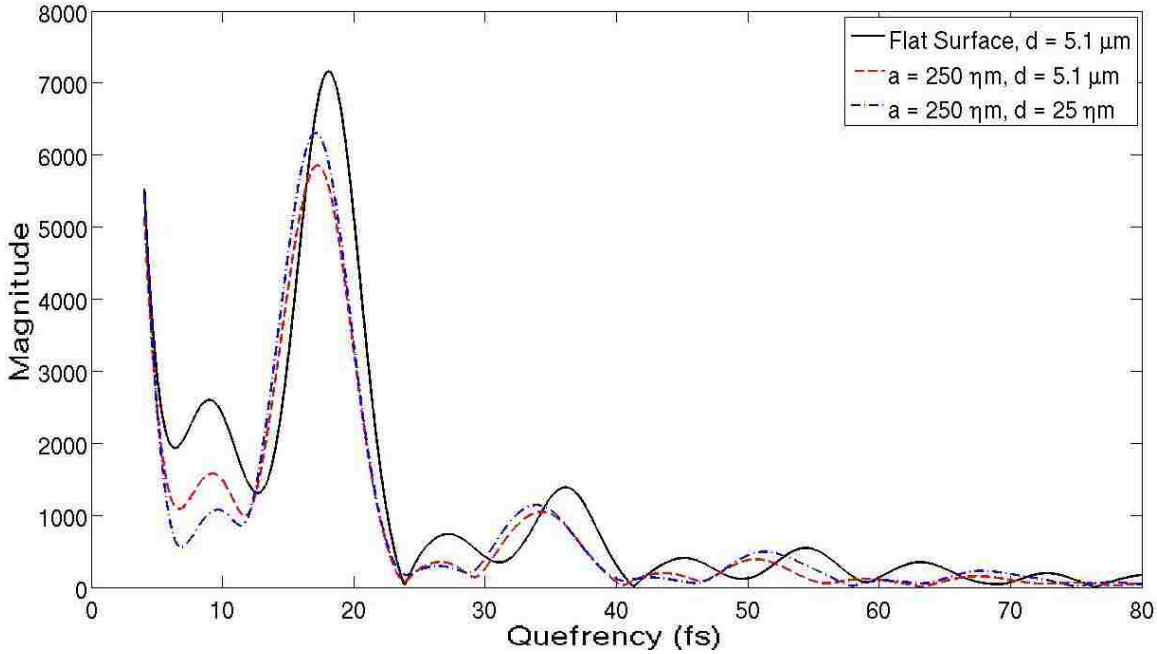

Figure 28: Comparison of cepstra curves corresponding to dielectric cubes having predetermined squares pattern on the illuminated face. The dielectric slabs have a 25-ηm (λ/20) *n* = 1.4 film-like inhomogeneity embedded at their midpoint depths. The section of the cepstral curve that shoots to the intersection with the vertical axis was omitted. The magnitude is absolute values.

The usual minor peak that indicates the presence of the thin film-like inhomogeneity (at about 9.5 fs for these cases) still arises with the presence of the rough surface pattern, and simultaneously no additional peak with respect to the flat surface case is introduced. It is evident that the square checkered pattern causes the magnitude of the peaks to diminish but it is interesting to note that the ratio of the minor to the major peak increases for the case where the illuminated

surface was shifted to place it at the maximum field intensity zone of the elongated photonic nanojet.

As a final test case related to the predefined square checkered surface roughness, the 250 ηm pattern is modified in such a way that the illuminated surface of the raised squares are tilted 45 degrees in the x-direction only (not y-direction) with respect to the photon propagation direction (z axis). For a better understanding of this new dielectric slab geometry, Fig. 29 shows a pair of 2-D cuts in the x-z and y-z planes.

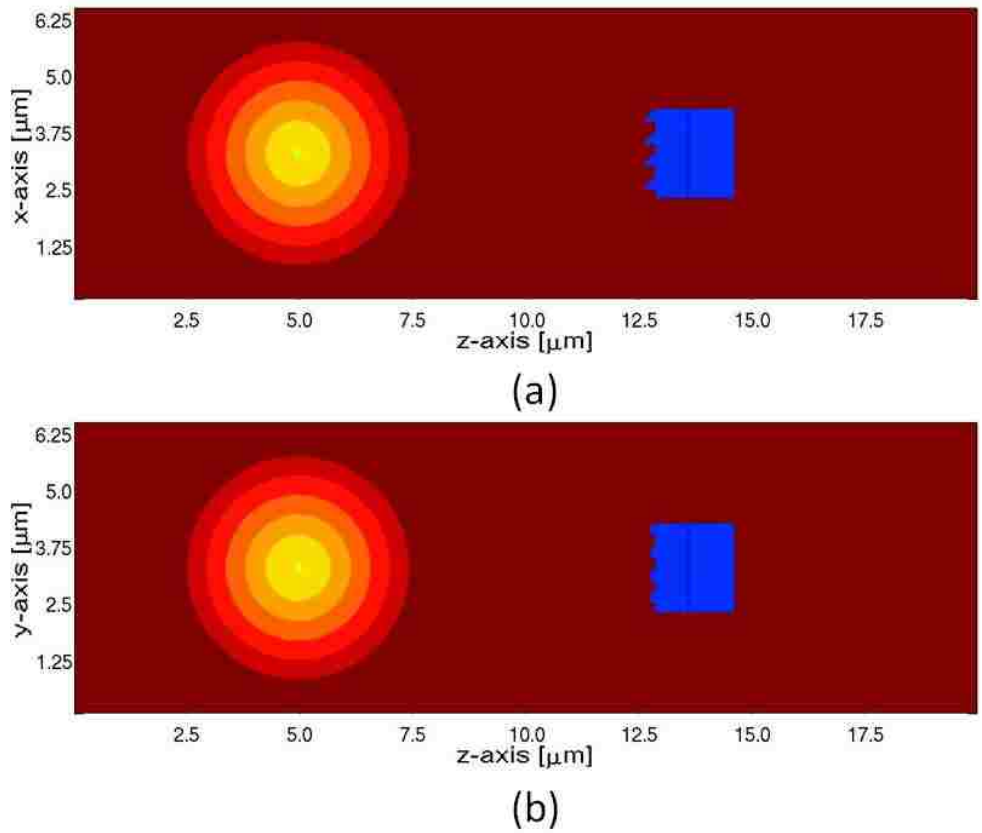

Figure 29: 2-D slices of the geometry of a 3-D six-layer radially graded dielectric microsphere exciting the 2-μm test homogeneous dielectric cube with a tilted square pattern etched at its illuminated surface: (a) cut on the x-z plane and (b) cut in the y-z plane.

Cepstral curves obtained from this configuration are shown in Fig. 30. The further reduction of the major peaks in the cepstral curve that correspond to the new

surface geometry with respect to those of the original squares pattern is an indicator that the direct backscatter from the new target is reduced. The 45 degrees inclination of the squares surfaces decreases the retroreflected light recorded at the observation point and increases the scattered component in other directions.

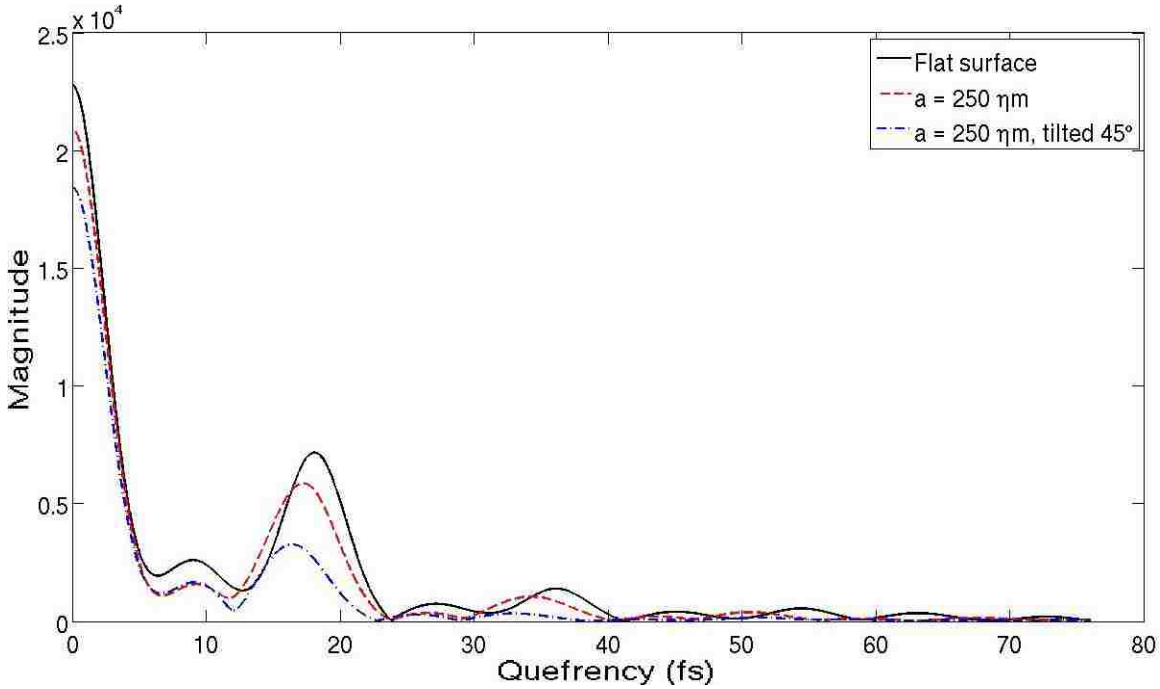

Figure 30: Comparison of the cepstra of rough surfaces having a predetermined squares pattern. In one case the illuminated face of the square is tilted 45 degrees with respect the photon propagation direction. In the other case the illuminated surface is normal to the incident light. For convenience, the flat surface case is also included. The magnitude is absolute values.

Fig. 31 shows a comparison of the backscattered signal from both square pattern cases in the time domain. The difference in the amplitude of the backscattered light from the rough surface (first pulse) is evident. This results in an enhanced contrast between minor and major peak in the cepstral curves with respect to both the flat surface and original squares pattern.

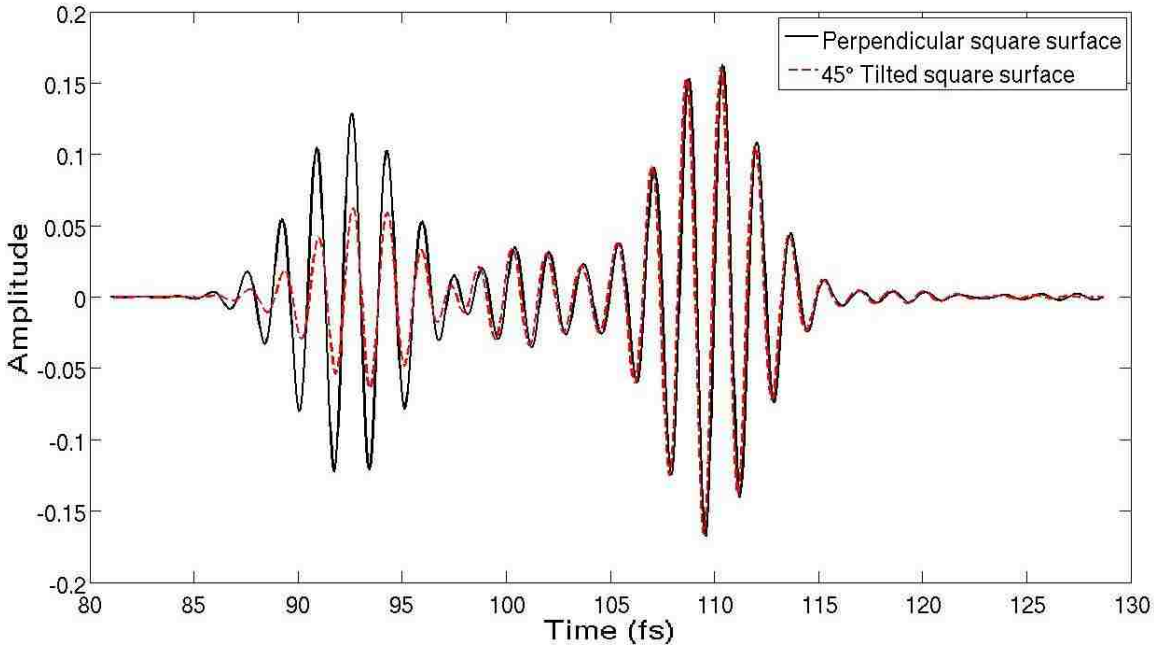

Figure 31: Comparison of the backscattered light from rough surfaces having a predetermined squares pattern in time domain. In one case the square's illuminated surface is tilted 45 degrees, the other is the original squares pattern (perpendicular to z axis).

5.3 Random Surface Roughness

A lot of the rough surfaces encountered in nature or artificially created by human being can be considered random for practical purposes. For example, the electrochemical etch of a compound semiconductor like gallium phosphide (GaP) with sulfuric acid (H_2SO_4) can create a macroporous network that forms a strongly randomized scattering structure in the optics regime [15]. The robust and accurate prediction of the scattering from random rough surfaces is important to compensate for unintended effects or to take advantage of this phenomenon. Therefore, the rest of study cases considered in this Chapter involve dielectric targets with the illuminated surface having a roughness pattern that is determined by a pseudorandom number generator.

For the first case of this section, a cube of refractive index n = 1.3 with a mean thickness of 1.875 ηm is considered. The total thickness in the z-direction of the

dielectric is dependent with position on the illuminated surface. This height is determined pseudorandomly for each grid position on the x-y plane presenting a maximum height variation of 250 ηm. Fig. 32 shows a 2-D slice of the dielectric target and microsphere configuration having the 25 ηm thin layer-like inhomogeneity.

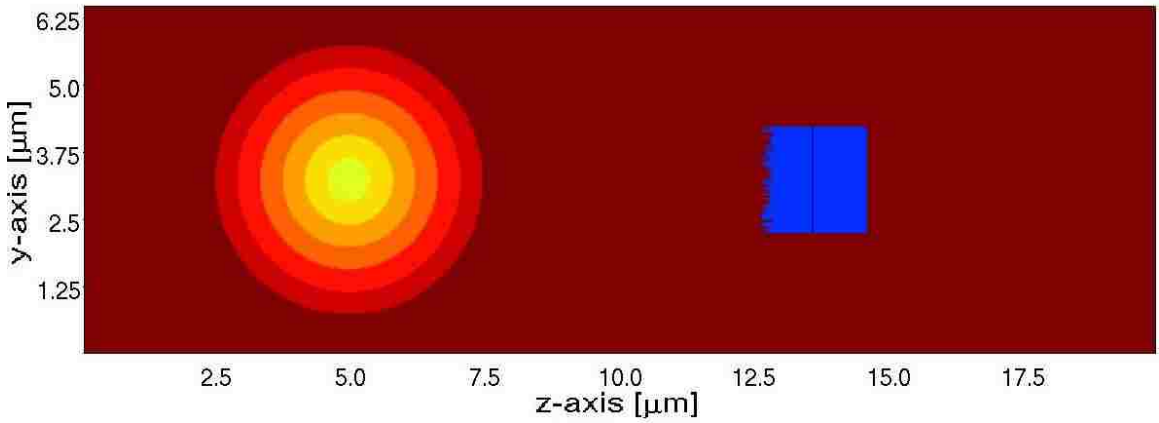

Figure 32: 2-D slice of the geometry of a 3-D six-layer radially graded dielectric microsphere exciting the inhomogeneous dielectric cube with a pseudorandom pattern etched at its illuminated surface.

As shown in Fig. 33, a pseudorandom roughness can increase the magnitude of the rahmonic peak that indicates the presence of the inhomogeneity (located at about 9 fs for the specific configuration of Fig. 5.7) with respect to the rest of the peaks in the cepstral curve. This increment extends high enough to make the peak at 9 fs the major one, ignoring the quefrency = 0 component. The enhanced contrast of the information related to the inside of the dielectric target with respect to that related to the surfaces is not necessarily at the expense of significant reduction of the additional peak (at 9 fs) absolute value. Comparing the current case under study against results from the flat surface dielectric, the first rahmonic peak is reduced to 76% of the benchmark case while the peak at about 18 fs is reduced down to 16%.

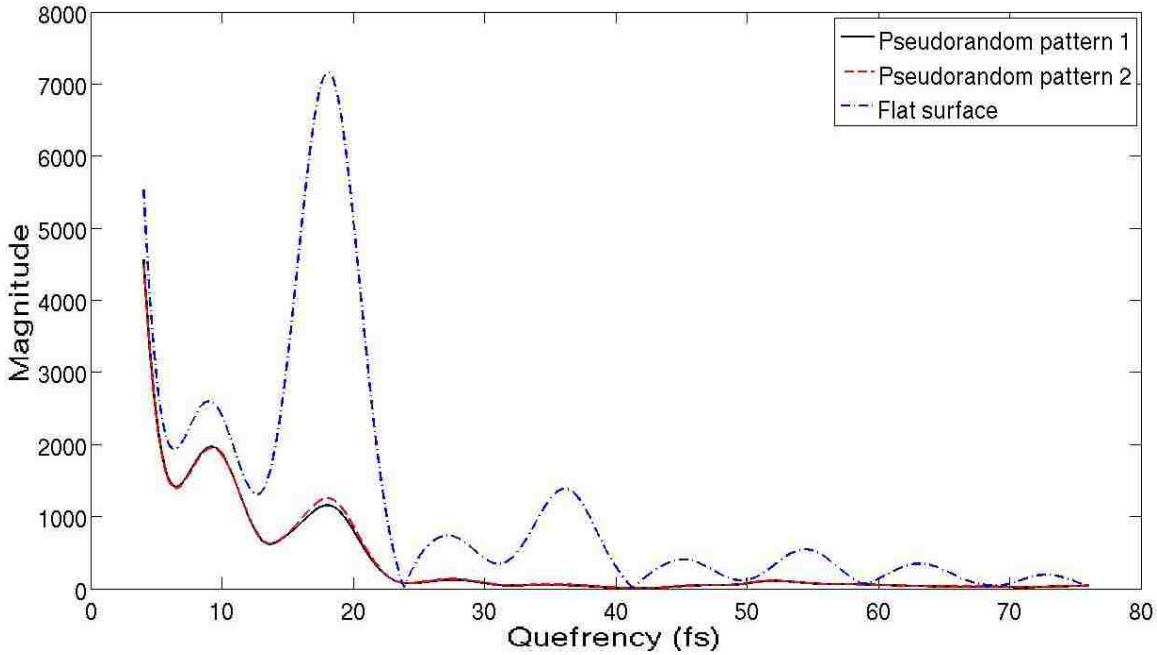

Figure 33: Comparison cepstral curves corresponding to 2 different pseudorandom generated rough surface patterns. The flat surface case is also shown for comparison of rahmonic peaks levels. The section that shoots to the quefrency = 0 component is omitted to distinguish better the difference in magnitudes of peaks.

Considering the results illustrated in Fig. 33, it is worthwhile to analyze again the dependence of the cepstral curve with respect to the transverse width of the inhomogeneity, but in this occasion illuminating a dielectric slab having a pseudorandom roughness pattern instead of a perfect flat surface.

Fig. 34 illustrates cepstral results for a 25-ηm thin film embedded at the dielectric cube's midpoint in z direction and having a transverse width of 300, 500, 750, or 1500 ηm. The particular results for a width of 500 ηm are most meaningful for comparison purposes. For this case, the cepstral curve still shows an observable minor peak that indicates the presence of the inhomogeneity. Referring to Fig. 22 that corresponds to the flat surface case, this same transversal width already converges very close to its respective homogeneous case.

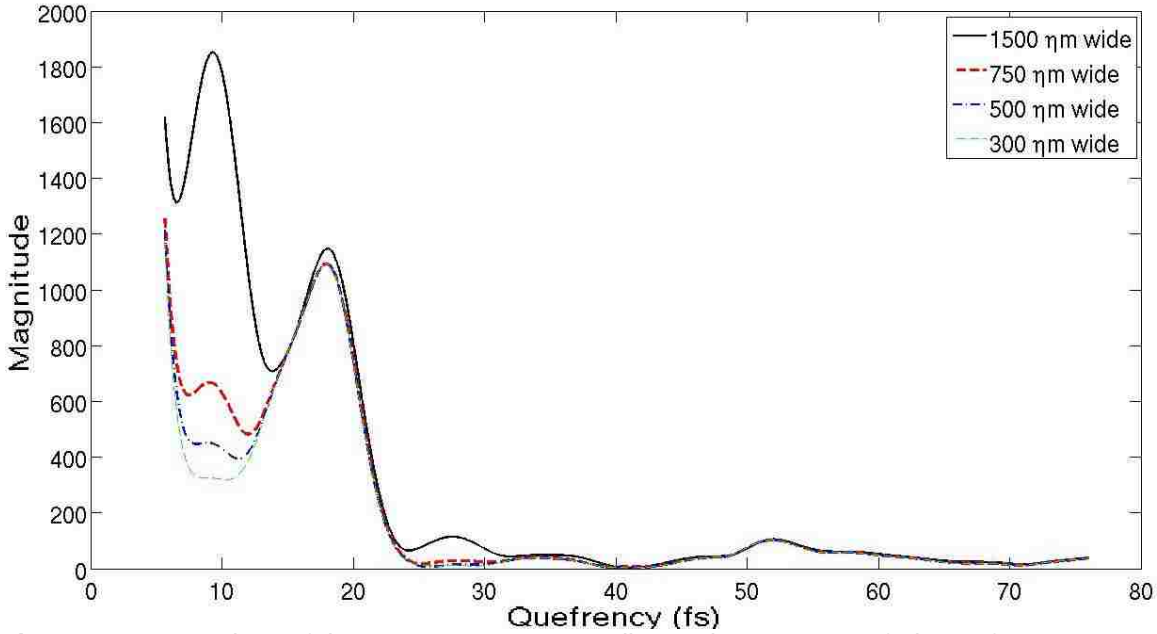

Figure 34: Comparison of the cepstra curves according to the geometry of Fig. 32 for transverse widths of the 25-ηm thin inhomogeneity equal to 300, 500, 750 and 1500 ηm.

All the simulation cases considered to this point were performed using the Scattered Field formulation of the FDTD method. In this code, the microsphere is illuminated with the incident plane wave and the resulting photonic nanojet is the beam of light that impinges the dielectric target. Results obtained from this kind of modeling were compared against those from the TF-SF formulation, where the incident field is time stepped through the complete Total Field region of the grid. The agreement between these two formulations is satisfactory. Referring to Fig. 8, the dominant component of the total EM fields propagating in the neighborhood of the sphere is the nanojet ($T_{12}T_{21}$ term). The incident field component is null in the area covered by the shadow of the sphere, where the dielectric target is located for all configurations covered in the previous and present Chapters. The agreement is still satisfactory for cases where a rectangular dielectric slab, either having flat or rough surface, extend more than the area covered by the shadow of the sphere. This is because while probing

rectangular dielectrics the backscattering component from the photonic nanojet dominates over the backscattering from plane wave illumination of the area not covered by the shadow of the microsphere. Fig. 35 shows a comparison between the results from both formulations for the case of a 2 μm dielectric cube case having a 25 ηm thin layer-like inhomogeneity at the middle point in the z-direction.

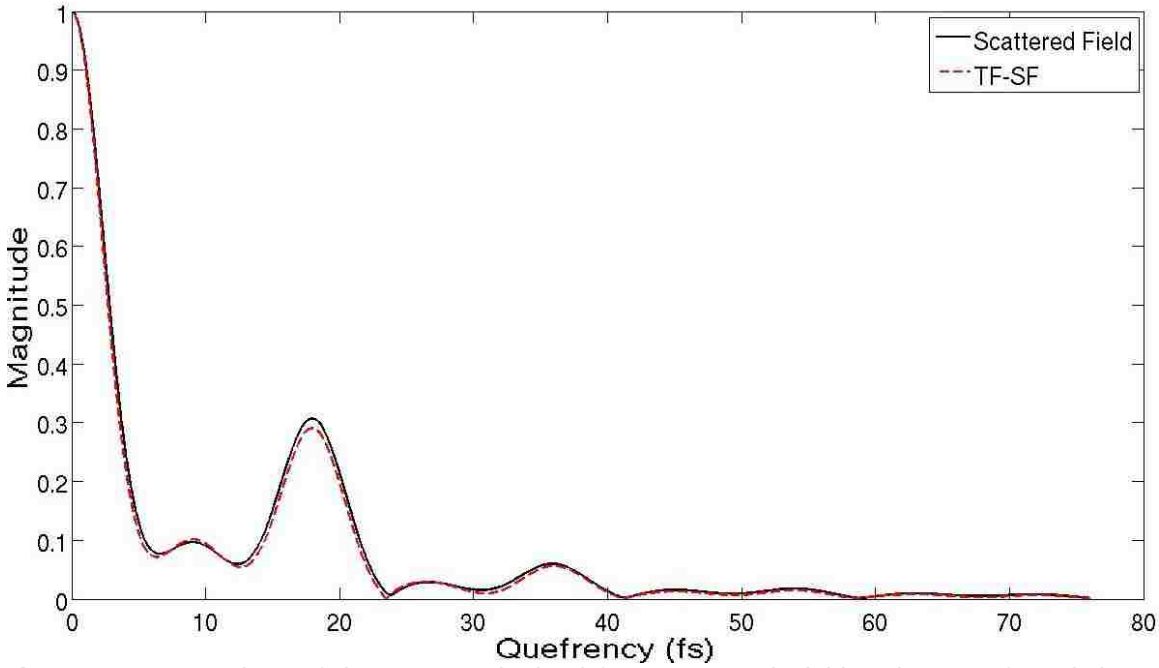

Figure 35: Comparison of the cepstra obtained from Scattered Field and TF-SF formulations. The curves correspond to the 2 μm dielectric cube having a flat surface with a 25 ηm inhomogeneity in the middle.

Chapter 6

Probing Biological Cells

6.1 Introduction

This chapter analyzes 3-D FDTD calculated backscattering results for photonic nanojet-illuminated dielectric objects representing biological cells. The major motivation of this kind of study is the application of photonic nanojets to early detection of cancer. Conventional far-field optical systems are restricted to a resolution of at best 200 ηm because of the diffraction of light. However, results documented in Chapters 5 and 6 make photonic nanojets a promising candidate for solving intracellular solids of ultra subwavelength thickness that cannot be detected with existing far-field optical imaging systems. The length scale of fundamental components of a biological cell such as nucleosomes, protein complexes, cytoskeleton, etc, is less than or about 100 ηm [13], and these intracellular solids provoke fluctuations in refractive index that can range in between 0.02 and 0.1 [20]. Hence molecular, genetic, or epigenetic aberrations can potentially be solved by employing photonic nanojets before the disease provokes alterations detectable with histological examinations of cells and tissue. The present Chapter is devoted to document the computational tests of this hypothetical ability of photonic nanojets.

6.2 The Model

The accurate and robust modeling of backscattering from a biological cell requires an increased demand of computational resources and complexity in comparison with the cases considered previously. In this Chapter, FDTD-

computed backscattered fields from nanojet-illuminated biological cell targets are obtained to examine the impact of the surface shape and roughness on the nanojets ability to detect embedded ηm-scale dielectric inhomogeneities of varying dimensions and positions. Specifically, the human colon cell HT29 is considered in the modeling by importing measurements taken with Atomic Force Microscopy (AFM). This is a very high-resolution type of scanning probe microscopy. It can resolve surface fluctuations of lengths on the order of fractions of a nanometer, which is more than 1000 times better than the best resolution obtained with diffraction limited optical systems. The traces were provided to Prof. Simpson's Computational Electrodynamics Laboratory by Richter [52]. Fig. 36 illustrates a top-down view of the topography of the HT29 colon cell that is imported to the FDTD model.

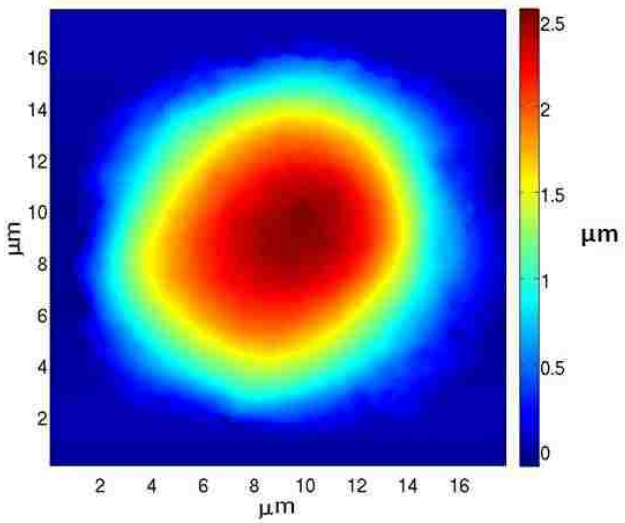

Figure 36: AFM topography of fixed HT29 colon cell provided by Richter [52]. Mapping was performed in an area of 17.8 by 17.8 µm with 512 sampling points in each direction.

The elongated photonic nanojet that is employed in Chapters 4 and 5 maintains very high intensity at many wavelengths away from the generating graded microsphere without significant divergence. Therefore this nanojet is a very good

option for applications requiring the detection of dielectric inhomogeneities that are embedded deep inside the target. But this enhanced length comes at the expense of increased beam width. The FWHM of the elongated photonic nanojet introduced in Chapter 3 is about 2.5 λ (1.28 μm). Because the maximum height of the particular biological HT29 cell used in this study is only about 2.5 μm, it is worth to make a trade-off between beam length and beam width in order to not only improve the transversal area resolution but to also ensure probing across the entire cell in the direction of photon propagation. Thus, the graded microsphere is replaced by a silica microsphere of 1.5 μm diameter. The resulting nanojet is shown in Fig. 37

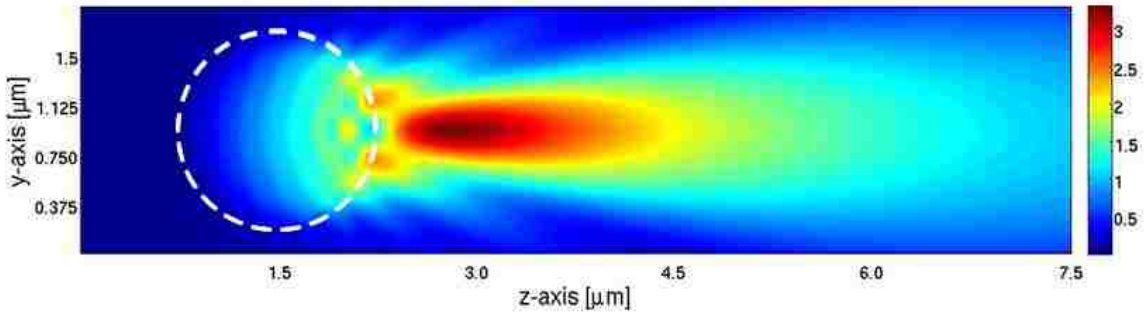

Figure 37: Visualization of a photonic nanojet generated by a plane-wave-illuminated silica microsphere of 1.5 μm diameter submerged in water. The λ of incident light is 500 ηm.

An additional change in the model is the background medium. For this study the system formed by the biological cell HT29 and the microsphere is assumed to be submerged in water. There are two reasons for this change. First, there exist studies in biological sciences in which it is desirable to get the image acquisition of a living cell to understand its physiology; this is better accomplished if the cell does not dry out. Second, for a fixed diameter of the silica sphere, the length of the nanojet is improved and unintended resonances inside the sphere are reduced, if the sphere is submerged in water. This is consequence of a lower

refractive index contrast of the silica sphere with respect to the water rather than with respect to free space.

Even by having water as background medium, the refractive index contrast of the silica is high enough to produce noticeable backscattering relative to echoes from the biological cell. These retroreflected pulses from the sphere are an unintended effect that carries no useful information regarding the dielectric target. Therefore during the data postprocessing of the results from a model involving the silica sphere, the backscattering from the sphere is subtracted from the recorded backscattered signal in the time domain before performing the double DFT to get the cepstral curve.

The area that spans the AFM measurements of the biological cell HT29 is considerably larger than the shadow area of the silica sphere. In addition, the cell topography is a complicated surface with roughness and overall curvature. To account in a more robust way for retroreflected light due to plane wave illumination of the biological cell, in this chapter the modeling is performed employing the TF-SF formulation.

For each simulation case, the backscattered time-waveform is recorded 3.8 μm on the incident side of the microsphere for subsequent post-processing to guarantee that there the cepstral curve presents no dependence with position of the observation point.

Even though during an actual microscopy observation the biological cell submerged in water may be a living entity and hence moving continuously, in the

present modeling it is assumed to be static at all times, thereby neglecting any possible Doppler-shifted frequency components.

6.3 Determining Resolution for Surface Roughness

One of the initial steps in any FDTD modeling project is the determination of the grid unit cell size. The chosen size must satisfy two requirements: 1) it has to be at the most $1/10^{th}$ of the smallest λ of interest, although for research purposes a size of $\lambda/20$ is usually recommended, and 2) it has to be small enough to correctly account for the effect of the smallest geometrical feature of interest. Because the present study is intended to account for the effects of the cell topography, it is the smallest geometrical feature of interest which is more likely to determine the required unit cell size. The resolution of AFM is so high compared to the best capabilities of any optical system that it is not necessary to use the trace's original precision as criteria to determine the grid unit cell size. Instead, an iterative procedure is used to determine the optimum value. Basically, the process begins by making an educated guess for a candidate unit cell size (in this case, 30 ηm). This initial resolution is used to generate an FDTD model of a 6×6 μm transversal section of the HT29 cell rather than the complete area covered by the AFM traces. This size section of the cell is wide enough to avoid interactions of the nanojet with lateral surfaces and it is positioned at the geometrical center of the area covered by the AFM measurements. The initial value of this grid unit cell is then gradually reduced until the cepstral curve converges.

At first, the biological cell is assumed to be homogeneous with a refractive index n equal to the mean refractive index n_o = 1.38 of a HT29 cell having pseudorandom n fluctuations [13]. The shadow side surface of the biological cell is assumed to be flat; this is shown in Fig. 38.

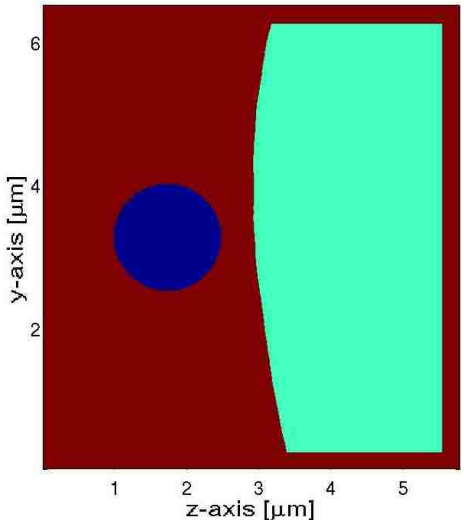

Figure 38: 2-D slice of the geometry of the 1.5 µm diameter silica dielectric microsphere exciting a 6 by 6 µm area of the HT29. For initial studies the biological cell is assumed to be homogeneous.

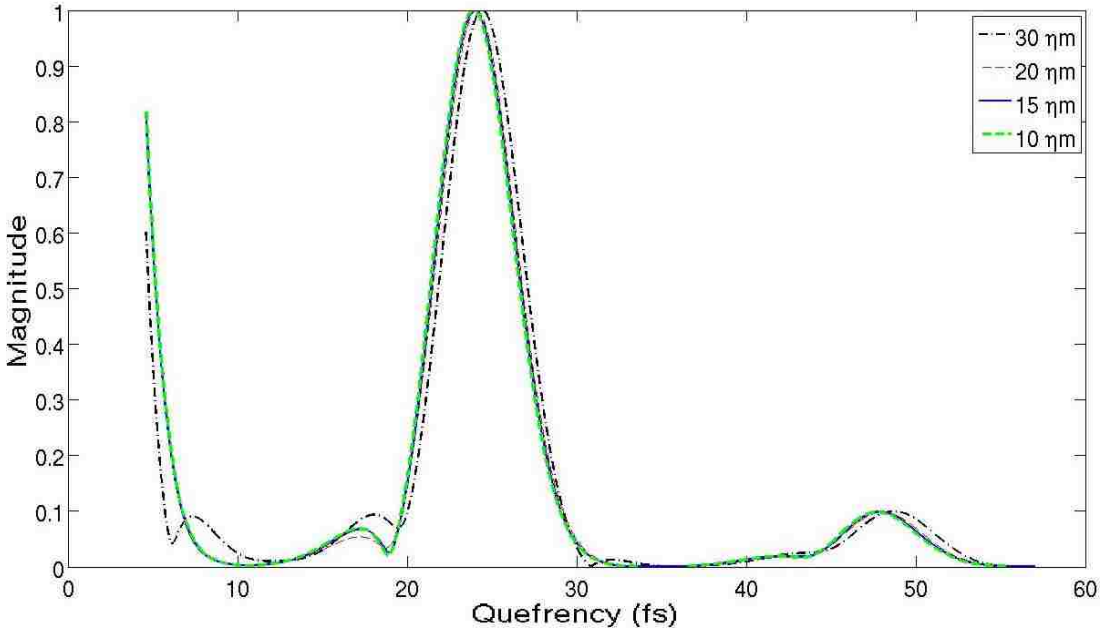

Figure 39: Dependence of cepstral curve with grid unit cell size. The grid cell is cubic, i.e. it has the same size in all three Cartesian directions. The magnitude is normalized to the major rahmonic peak magnitude. The section that shoots to quefrency = 0 component is omitted to better illustrate the convergence of the curves.

The resulting cepstral curves corresponding to modeling the scenario of Fig. 38 using grid unit cell sizes of 30, 20, 15, or 10 ηm are shown in Fig. 39.

These results reveal that the nanojet has a maximum resolution to topographic fluctuations of about 15 ηm. Hence the grid unit cell size for the rest of the modeling in this chapter is set to 10 ηm.

Note that the cepstral curve to which results converge is very similar to that of a homogeneous cubic dielectric slab, except that there is a minor peak that does not diminish with grid resolution at about 18 fs. This is not observed shape for all previous homogeneous targets considered in this dissertation. The signal in the time domain shows that the leading pulse takes a longer time to diminish than the second pulse due to multiple scatterings on the rough surface of the cell; this is shown in Fig. 40. For comparison, the backscattered field from a homogenous slab having the same *n* and thickness is also shown.

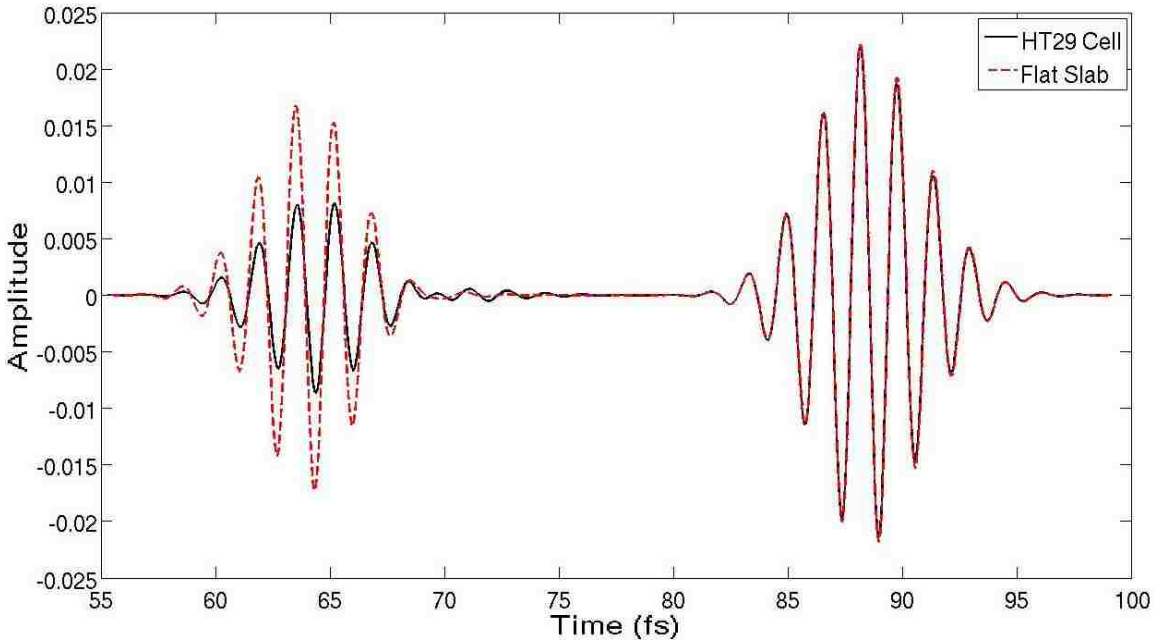

Figure 40: Recorded backscattered light in time domain from the biological cell HT29 topography or a dielectric slab having the same *n* and thickness. The plot corresponds to the grid unit cell size equal to 10 ηm.

The roughness of the cell topography produces reflections in all directions and also generates interferences between reflected rays that are out of phase due to the difference in the distance that they traveled to impinge the surface of the HT29 cell. Hence, the backscattered echo from the rough surface is reduced in amplitude and also presents modified frequency content with respect to the backscattering from a smooth surface case. This makes the leading pulse different than the echo corresponding to the shadow side of the cell. As a consequence, the representation of the signal in the time domain with Equation 4.1 becomes less representative of the signal, and the resulting cepstral curve differs from the predicted shape.

The comparison of the spectra corresponding to each pulse is shown in Fig. 41.

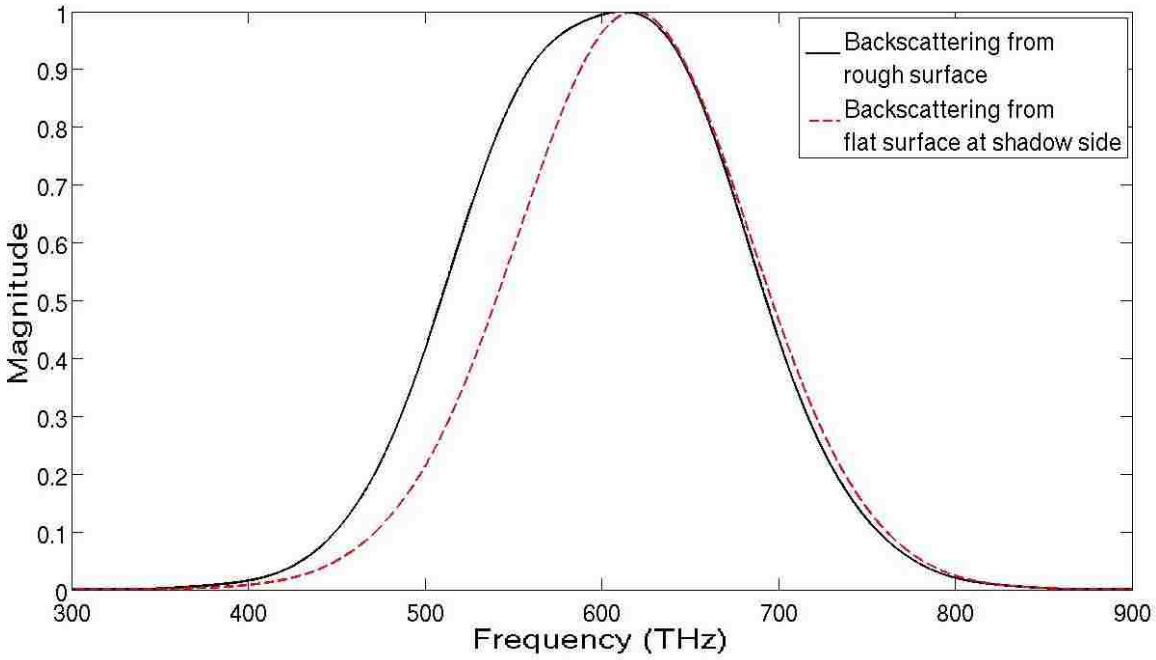

Figure 41: Comparison of spectrum magnitude of backscattered light from biological cell HT29 topography at the illuminated side and flat surface at the shadow side.

To illustrate the effects of the surface roughness modeled with different grid unit cell sizes, Fig. 42 shows the FDTD grid of the biological cell surface area that is

directly illuminated by the nanojet. All four grid resolutions considered in Fig. 39 are shown.

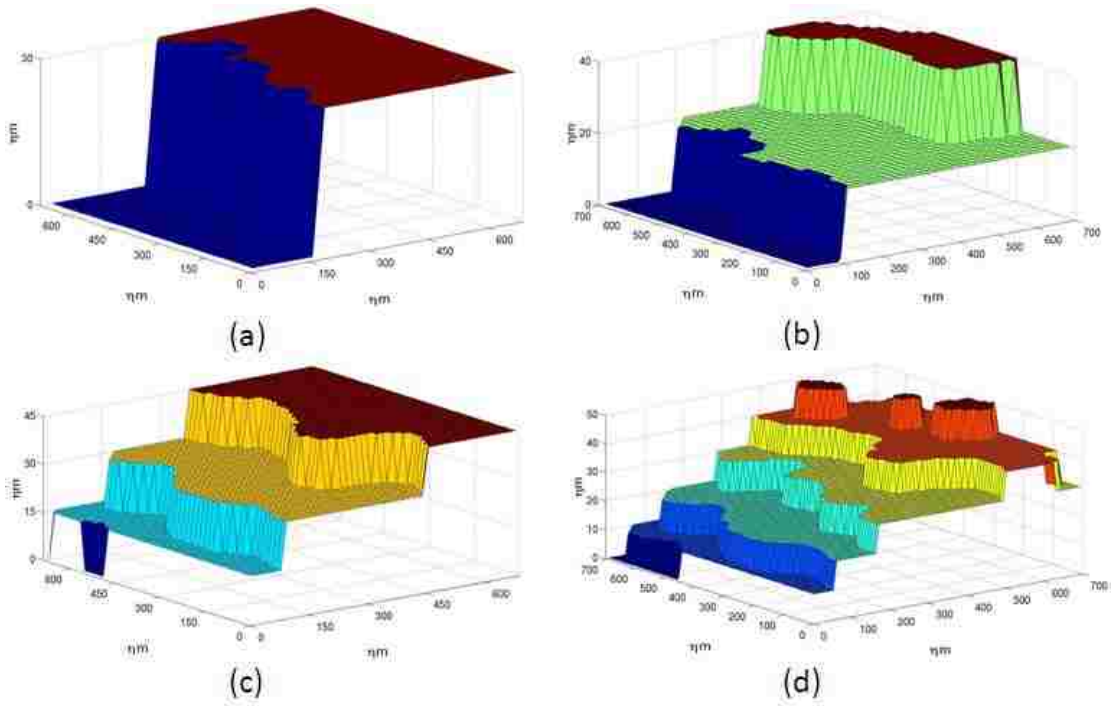

Figure 42: Zoomed in FDTD grid representation of the area that spans the nanojet illuminated surface region of the HT29 topography for the different grid resolutions considered in this study: (a) 30 ηm, (b) 20 ηm, (c) 15 ηm, and (d) 10 ηm.

6.4 Probing Random Refractive Index

The model of the biological cell HT29 accounts not only for its topography but also for the effect of internal organelles. It is known that there exist fluctuations of the *n* inside of the cell due to the dependence with position of concentrations of intracellular solids like DNA, RNA, lipids, etc. Thus the intra cellular solids of the biological cell are modeled as a stationary process in the second-order cumulant approximation [46]. In this kind of process, the *n* is determined randomly with position and it has negligible variations along a distance equal to a parameter termed correlation length l_c. In other words, to advance the modeling to account for the effect of intracellular solids, the biological cell is filled with rectangular

blocks of homogeneous *n*. The value of *n* for each block is determined pseudorandomly and each block has a specific l_c in each Cartesian direction. It is the value of this l_c that determines the aggressiveness of the specific HT29 cell line. For all cases, the mean refractive index n_o is equal to 1.38. The maximum refractive index variations (Δn) for typical biological tissue can range from 0.02 to 0.1 [20], but for this work the maximum Δn is set to 0.1. Figure 43 shows a 2-D slice of the HT29 cell filled with 60×60×60 ηm dielectric cubes. In this study the complete HT29 cell is imported into the model.

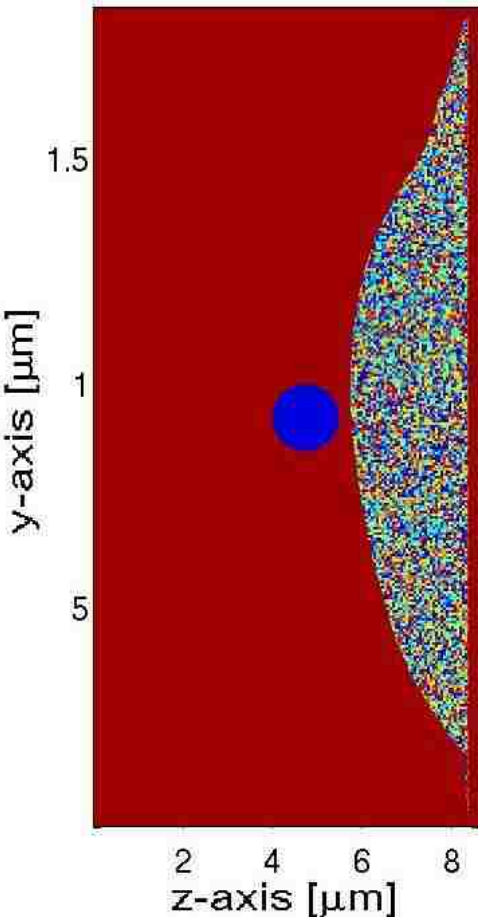

Figure 43: 2-D slice of the geometry of the 1.5 µm diameter silica dielectric microsphere exciting the colon cancer cell HT29 having a pseudorandom refractive index pattern. In the example shown, the homogeneous blocks are 60 × 60 × 60 ηm.

In the first study involving random *n* fluctuations, the sensitivity of photonic nanojets to small values of l_c is tested. The analysis begins by considering 600×600×100 ηm rectangular blocks and the size of the blocks is gradually decreased until the cepstral curve converges to the homogenous HT29 case. Note that unlike the initial homogeneous block (600×600×100 ηm), for the 3 smaller l_c the blocks are cubic. Resulting cepstral curves are shown in Fig. 44.

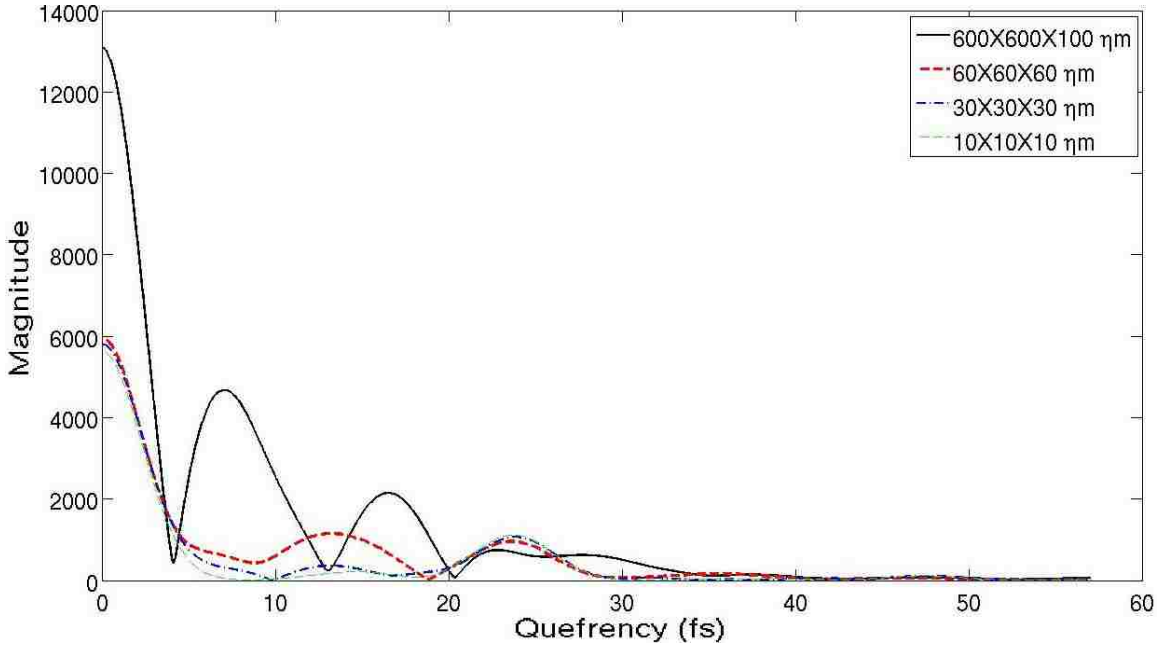

Figure 44: Comparison of cepstral curve with different l_c starting with rectangular blocks of 600×600×100 ηm in the x, y and z directions respectively. The sizes of the blocks are gradually reduced until the cepstral curve converges to the homogeneous case. The homogeneous case is not shown because it is a perfect match with the 10×10×10 ηm blocks.

In general, the magnitudes of the cepstrums in Fig. 44 indicate that a decrease of the l_c results in a reduction of the backscattered field from the biological cell membrane. There is also a gradual reduction with l_c of the peaks that are located at quefrency values less than 25 fs (this is the delay from the shadow side of the biological cell). This suggests lower backscattering levels from internal square blocks. As the curves converge to the homogeneous case, the peak that

corresponds to the flat side of the biological cell has a slight tendency to increase. This ability to detect blocks as small as about 30 ηm demonstrates the nanojets potential to detect the fundamental “building blocks” of a biological cell because these have been experimentally proven to be about 100 ηm or less [13].

The maximum variation of the *n* inside the biological cell is a constant that does not depend on how advanced the carcinogenesis stage is; what determines the aggressiveness of a cell line and distinguishes it from other lines is the value of l_c. Two cases of cell lines are considered. One is the C-terminal Src kinase (Csk) knockdown and it can be represented with the 600×600×100 ηm rectangular homogeneous blocks filling the cell topography. The other case is the epidermal growth factor receptor (EGFR) knockdown which is less aggressive and it is filled with 60×60×60 ηm cubic blocks [13]. The cepstral curves from three different pseudorandom patterns per cell line are shown in Fig. 45.

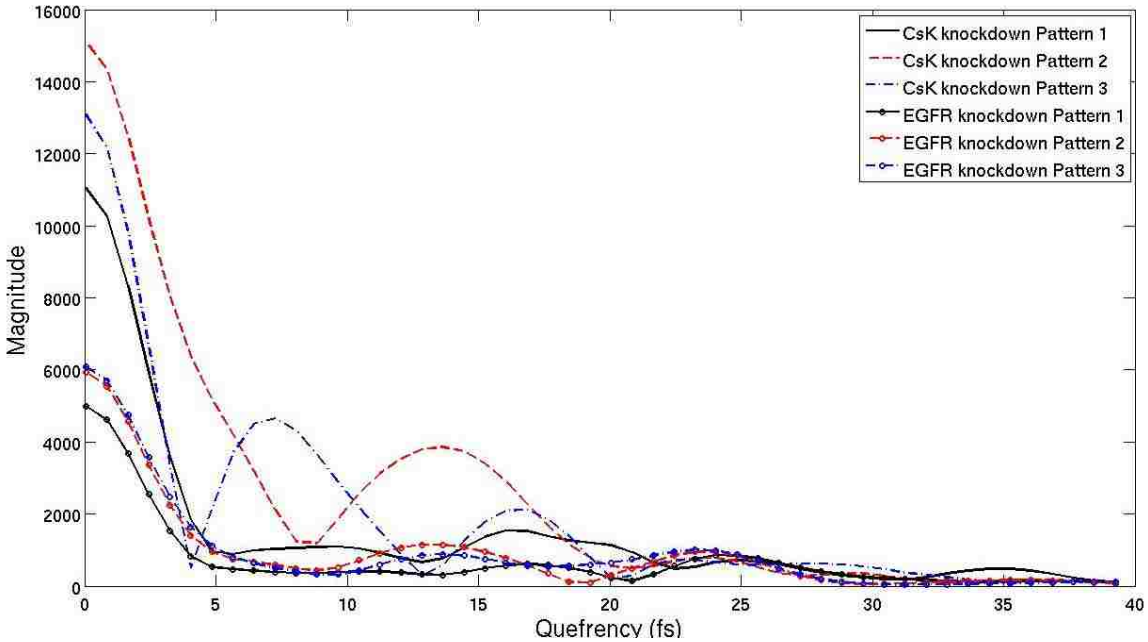

Figure 45: Comparison of cepstral curve from the cell lines CsK and EGFR. 3 different pseudorandom patterns are shown.

In general, the more aggressive cell line (CsK) backscatters more EM fields than the EGFR line, but the pattern number 1 of the CsK line shows that it may be possible to see an overlap with some samples of the EGFR line for quefrency positions greater than 5 fs. However, in all the cases considered in this study it is possible to distinguish one cell line from the other based on the quefrency = 0 component of the cepstral curve.

6.5 Comparison of Rough Vs Smooth Topography

This section involves a study of the effect that different degrees of cell surface roughness have on the cepstral curve of the backscattered light. To manipulate the topography of the HT29, the original trace is approximated with polynomials of different orders before importing the biological cell to the model. This fitting procedure results in biological cells having the approximate same overall shape and dimensions than the actual measurements but with a smoother surface that depends on the degree of the polynomial. Fig 46 illustrates a comparative of the cell topography corresponding to the original measurements taken with AFM and the one obtained after fitting the traces with a polynomial of 6^{th} order.

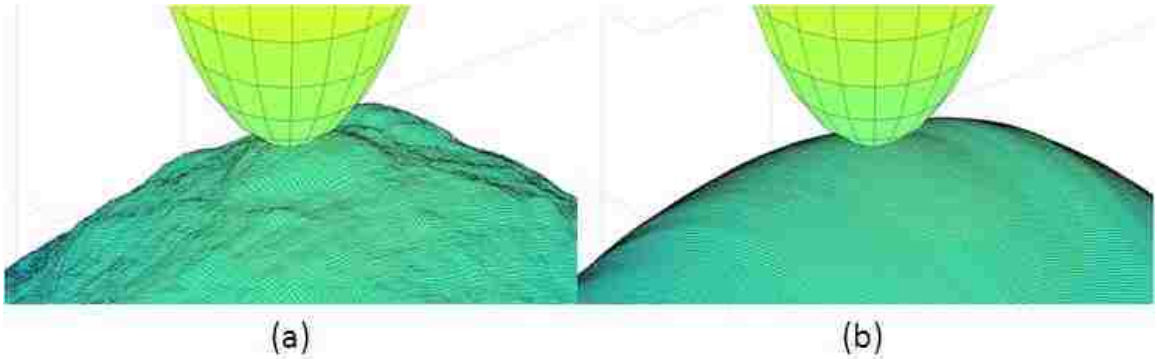

Figure 46: Comparison of biological cell HT29 corresponding to: (a) original measurements taken with AFM, and (b) smoothen with a polynomial of 6^{th} order. The silica microsphere is shown to illustrate the photonic nanojet illuminated position.

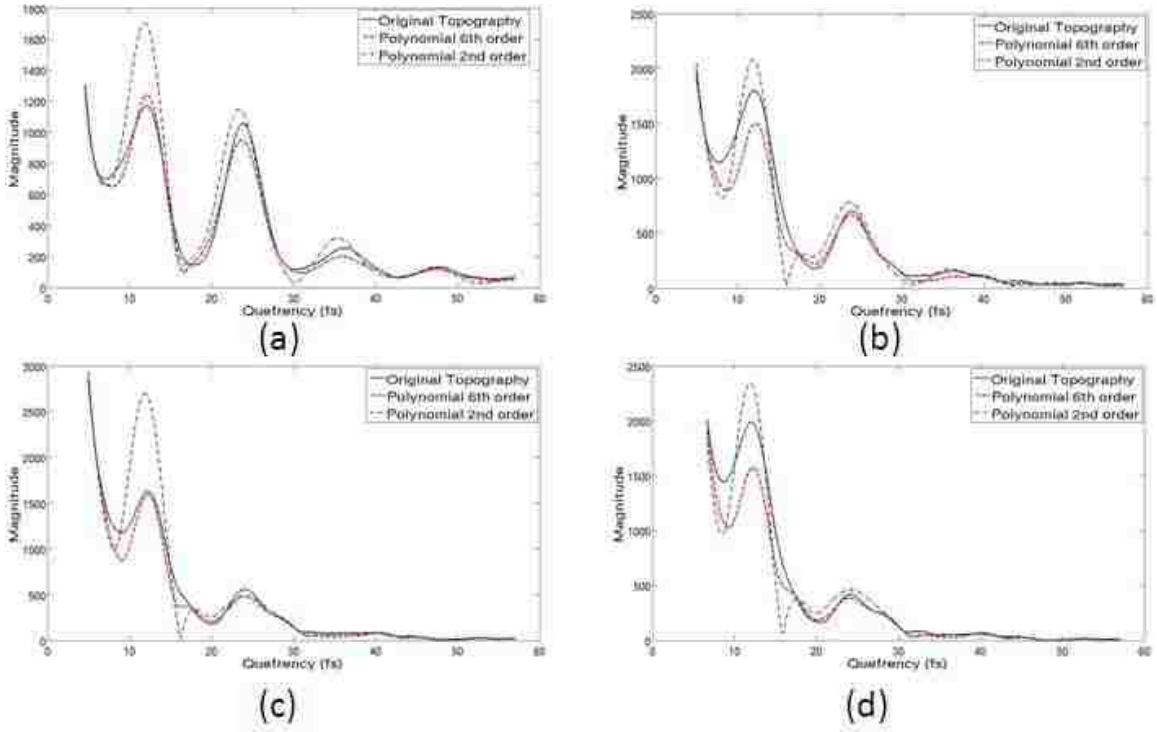

Figure 47: Cepstral curves corresponding to the biological cell HT29 having different surface roughness with an n = 1.4 thin layer inhomogeneity thickness of: (a) 10 ηm, (b) 20 ηm, (c) 30 ηm, and (d) 40 ηm.

To study the effect of the surface roughness on the sampling of an intracellular target, embedded in the biological cell is an inhomogeneity of n = 1.48 (this represents a Δn = 0.1 with respect to the average of the cell). Three different surface roughnesses are considered: original topography, polynomial of 6th order, and polynomial of 2nd order. Fig. 47 shows results for inhomogeneity thicknesses of 10, 20, 30 and 40 ηm. These results are consistent with those shown in Fig. 33 corresponding to the pseudorandom surface pattern on a dielectric slab in the sense that the peaks of the flat surface are higher than those corresponding to rough surfaces. This is considering that the topography fitting procedure using the 2nd order polynomial provides a smooth surface. However it also should be noted that for the HT20 having a smooth surface, the peak that indicates the presence of the inhomogeneity is greater than the peak indicating the time delay

from the shadow side surface of the cell regardless of the surface roughness. This is not the case for a flat dielectric slab.

In section 6.2 it was seen that the surface roughness of the biological cell affects the frequency content of the backscattered fields from this rough surface. Because the spectra of the two echoes differ from each other, a minor peak arises in the cepstral curve just next to the major peak. It would be expected that the cepstral curve should converge to that of a homogeneous dielectric slab having the same *n* as the surface is smoothen. This is actually the case only for a section of the cell like the one shown in Fig. 38. However, when the complete cell is imported to the modeled, an extra retroreflected pulse appears in the signal in the time domain. This extra pulse is delayed with respect to the backscattered pulse from the shadow side of the biological cell. This is caused by the plane wave illumination of the area of the cell that is not covered by the shadow of the microsphere. This extra pulse in the time domain amplifies the minor peak in the cepstral curve and therefore the cepstral curve of the complete cell never converges to an equivalent homogeneous slab even with the smoothed surface obtained with the 2^{nd} order polynomial. The cepstral curve dependence on surface roughness for the complete HT29 cell is shown in Fig. 48.

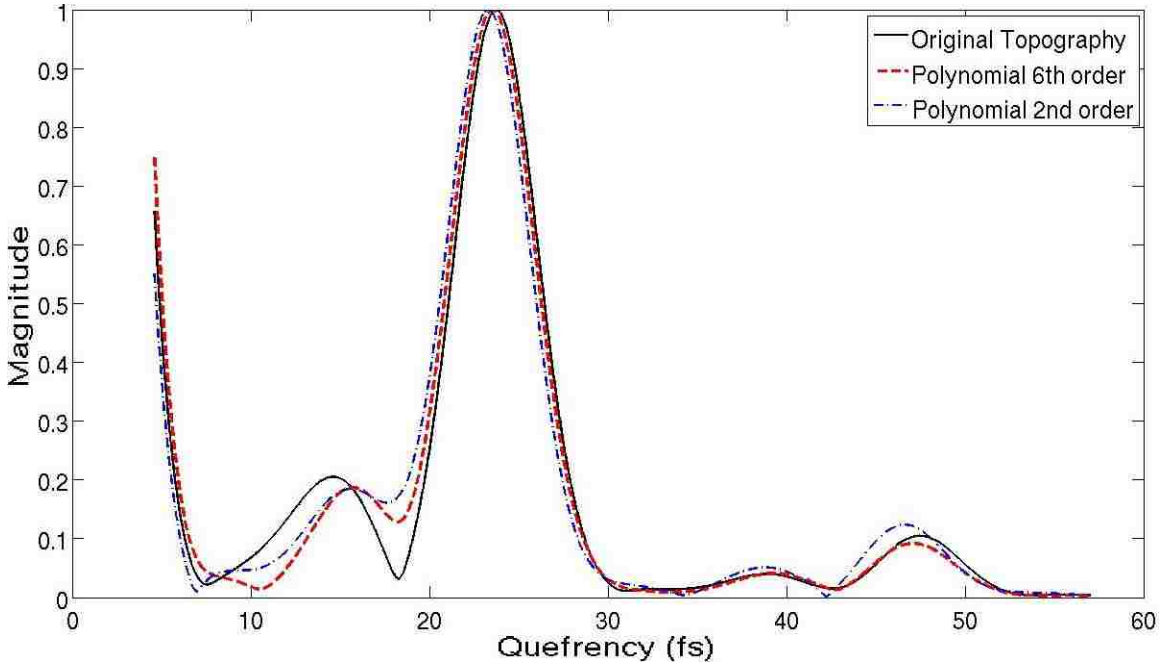

Figure 48: Cepstral curves corresponding to the homogeneous biological cell HT29 having different surface roughness.

Chapter 7

Future Work

7.1 Introduction

Cepstral analysis of backscattered light from photonic nanojet illumination of a dielectric target is a powerful signal processing method to detect ultra-subwavelength-thin, weekly contrasting film-like inhomogeneities embedded within the target. For example, it is possible to determine details like the electrical thickness of the slab, position of the inhomogeneity in the photon propagation direction, *n* contrast, etc. In Chapter 4 it was shown that for equally spaced interfaces (boundaries between the background medium and dielectric slab sides, and boundaries between inhomogeneities and dielectric slab sides) each i^{th} rahmonic peak in the cepstral curve carries information regarding multiple interfaces. For most of the cases, it is the backscattering from the i^{th} interface that dominates the amplitude of the peak. Therefore it should at least in principle be possible to engineer a configuration of a dielectric slab having several multiple inhomogeneities that after a cepstral analysis allows an optimum and reliable application of photonic nanojets to optical data storage disks having several layers. This may be tackled by testing configurations of layers having different *n*, allowing for non-uniform gaps between layers to place the components of the A_i terms of Equation (4.4) so that they do not interfere with certain $\cos(2\pi\tau_i f)$ terms, depicting information from the phase of the cepstrum and spectrum, or testing alternative definitions of cepstra.

Further, the present work can be applied to inspecting semiconductor wafers during the manufacturing of ICs. However it is necessary to study the effect of metallic nanoparticles and nanostructures on the cepstral curves. For another project, the author of this dissertation implemented the auxiliary differential equation (ADE) within an FDTD model in order to account for the free-electron and bounded-electron effects of metallic materials in the optics regime using the Lorentz-Drude model. The application of the ADE to account for gain of semiconductor materials is yet to be implemented.

Very recently, Kim *et al.* [53] have experimentally demonstrated different ways to engineer the properties of photonic nanojets by employing axially asymmetric structures or by manipulating the illumination conditions like the wavelength, the amplitude distribution, or the polarization. It is worth investigating the possibility of applying the contribution documented in [53] to expand the capabilities of photonic nanojet in uniquely determining the relevant parameters of dielectric targets, in particular for complicated targets like biological cells. It also may be convenient to investigate if these techniques still hold for a layered microsphere that generates an elongated photonic nanojet.

7.2 Disorder strength

In this dissertation a cepstral curve is obtained from a 1-D channel that transversally intersects the dielectric to be solved. For most microscopy applications it is desirable to generate a visual 2-D map of the complete area occupied by the biological cell. Using photonic nanojets, this 2-D map would be

comprised of an array of 1-D channels, i.e. each of the 1-D photonic nanojet illuminations would yield a pixel of a 2-D image.

The disorder strength is a scalar measurement of the backscattered light over the complete λ range of interest that is used in mesoscopic light transport theory. This parameter depicts the refractive index contrast and l_c of any scale. For computing the disorder strength from the recorded signal, the fluctuating component of the backscatter spectrum would be used to calculate the correlation function of the refractive index fluctuations inside the dielectric target.

Disorder strength can be applied to the backscattered light from a system involving photonic nanojets to generate 2-D images of biological cells that depicts information about ultra-subwavelength weekly contrasting intracellular structures.

7.3 Application of photonic nanojet to photodetectors

There exists a broad potential for applications of photonic nanojets to the sensing of light in the field of nanotechnology. But the light absorption into electronic devices at chip-level is problematic; this is why it is necessary to develop novel and highly efficient photodetectors. At present, the power dissipation, noise, area and latency of photodetectors must be improved in order to achieve satisfactory efficiency at a system level. This problem arises from the size incompatibility between microscale dielectric photonic devices and nanoscale silicon electronics on the chip level. Photodetectors employing plasmonics offers a promising means to integrate optics with silicon electronics at nanoscale dimensions. The capability of photonic nanojets to generate subwavelength beam widths makes them good candidates to combine them together with the metallic nanostructure

that produces the plasmonics in order to significantly enhance the light absorption into a semiconductor slab.

Chapter 8

Conclusions

In summary, this dissertation began by introducing an elongated photonic nanojet that has an improved length over the original version proposed by Kong, et al. [6]. This elongated nanojet is generated by using a layered microsphere with a modified refractive index profile in the radial direction. Photonic nanojets were then demonstrated to permit detection of ultra-subwavelength-thin, weakly contrasting film-like inhomogeneities embedded in 3-D dielectric structures via 1-D illumination and detection. As a result, photonic nanojets are able to serve as a useful, new approach for conducting inverse-scattering studies of weakly contrasting micron-scale material objects having embedded ultra-subwavelength features.

FDTD computational modeling of photonic nanojets illuminating dielectric targets along with post-processing of backscattered field data to obtain the cepstrum permits extraction of dielectric target properties, such as transverse area, refractive index and thickness. These same properties can also be obtained for ultra-subwavelength thin layer(s) embedded at certain distances from the target surface.

The effect of dielectric slabs having a rough surface on the nanojet illuminated side was investigated. Two methods were used to define the surface roughness: predetermined square checkered patterns and pseudorandom patterns. It was demonstrated that the surface roughness can decrease the absolute magnitude

of the backscattered fields, but the detection of the internal features were enhanced.

The ultimate test in this dissertation was to use photonic nanojets to detect nanometer-scale features within a sample human colon cancer HT29 cell accounting for the effects of the cell topography. In a similar manner as for the dielectric slab case, the roughness of the cell was found to reduce the total backscattered light, but it improves the detection of the internal features. The ability of photonic nanojets to distinguish between two different degrees of cancer cell aggressiveness, with neither exhibiting histological aberrations, was demonstrated.

REFERENCES

[1] Q. Wu, G. D. Feke, R. D. Grober, and L. P. Ghislain, “Realization of numerical aperture 2.0 using a gallium phosphide solid immersion lens,” *Applied Physics Lett*., vol. 75, issue 26, pp. 4064-4066, 1999.

[2] Z. Chen, A. Taflove, and V. Backman, “Photonic nanojet enhancement of backscattering of light by nanoparticles: A potential novel visible-light ultramicroscopy technique,” *Optics Express*, vol. 12, issue 7, pp. 1214-1220, April 5, 2004.

[3] X. Li, Z. Chen, A. Taflove, and V. Backman, “Optical analysis of nanoparticles via enhanced backscattering facilitated by 3-D photonic nanojets,” *Optics Express*, vol. 13, pp. 526-533, Jan. 24, 2005.

[4] A. Heifetz, K. Huang, A. Sahakian, X. Li, A. Taflove, and V. Backman, “Experimental confirmation of backscattering enhancement induced by a photonic jet,” *Applied Physics Lett*., vol. 89, 221118, Nov. 27, 2006.

[5] A. Heifetz, S.-C. Kong, A. V. Sahakian, A. Taflove, and V. Backman, “Photonic nanojets,” *J. Computational & Theoretical Nanoscience*, vol. 6, pp. 1979-1992, Sept, 2009.

[6] S.-C. Kong, A. Taflove, and V. Backman, “Quasi one-dimensional light beam generated by a graded-index microsphere,” *Optics Express*, vol. 17, pp. 3722-3731, March 2, 2009.

[7] E.H. Synge, “A suggested method for extending microscopic resolution into the ultra-microscopic region,” *Philos. Mag*., vol. 6, pp. 356–362, 1928.

[8] Y. Oshikane, T. Kataokaa, M. Okudaa, S. Haraa, H. Inouea, and M Nakanoa, “Observation of nanostructure by scanning near-field optical microscope with small sphere probe.” *Sci. Technol. Adv. Mater*., vol 8, issue 3, pp. 181-185, 2007.

[9] J. B. Pendry, “Negative refraction makes a perfect lens.” *Phys. Rev. Lett*., vol 85, issue 18, pp. 3966–3969, 2000.

[10] M. I. Stockman, S. V. Faleev, and D. J. Bergman, “Coherent Control of Femtosecond Energy Localization in Nanosystems,” *Phys. Rev. Lett*., vol. 88, issue 6, pp. 067402-1-4, 2002.

[11] S. W. Hell and J. Wichmann, “Breaking the diffraction resolution limit by stimulated emission: stimulated-emission-depletion fluorescence microscopy,” *Optics Letters*, vol. 19, issue 11, pp. 780-782, 1994.

[12] E. Rittweger, K. Y. Han, S. E. Irvine, C. Eggeling, S. W. Hell, “STED microscopy reveals crystal colour centres with nanometric Resolution,” *Nature Photonics*, vol 3, pp. 144–147, 2009.

[13] H. Subramanian, P. Pradhan, Y. Liu, I. Capoglu, X. Li, J. Rogers, A. Heifetz, D. Kunte, H. Roy, A. Taflove, and V. Backman, “Optical methodology for detecting histologically unapparent nanoscale consequences of genetic alterations in biological cells,” *Proc. Natl. Acad. Sci*., vol. 105, issue 51, pp. 20124-20129, 2008.

[14] H. Subramanian, P. Pradhan, Y. Liu, I. R. Capoglu, J. D. Rogers, H. K. Roy, R. E. Brand, and V. Backman, “Partial wave microscopic spectroscopy detects sub-wavelength refractive index fluctuations: an application to cancer diagnosis,” *Optics Letters*, vol. 34, issue 4, pp. 518-520, 2009.

[15] E.G. van Putten, D. Akbulut, J. Bertolotti, W.L. Vos, A. Lagendijk, A.P. Mosk, “Scattering Lens Resolves sub-100 nm Structures with Visible Light,” *Phys. Rev. Lett.*, vol. 106, issue 19, pp. 193905-1-4, 2011.

[16] S. Yang, A. Taflove, and V. Backman, “Experimental confirmation at visible light wavelengths of the backscattering enhancement phenomenon of the photonic nanojet,” *Opt. Express*, vol. 19, issue 8, pp. 7084-7093, 2011.

[17] S. Kong, A. Sahakian, A. Taflove, and V. Backman, “Photonic nanojet-enabled optical data storage,” *Opt. Express*, vol. 16, issue 18, pp. 13713-13719, 2008

[18] “Intel® 32nm Logic Technology”, Intel Corporation URL: http://www.intel.com/technology/architecture-silicon/32nm/index.htm

[19] Z. Chen, H. Chu, and S. Li, “Optical metrology using a photonic nanojet,” U.S. Patent 7,394,535, 2008.

[20] J. M. Schmitt and G. Kumar, “Optical Scattering Properties of Soft Tissue: A Discrete Particle Model,” *Appl. Opt*. vol. 37, issue 13, pp. 2788-2797, 1998

[21] K. S. Yee, “Numerical solution of initial boundary value problems involving Maxwell's equations in isotropic media,” *IEEE Trans. Antennas Propagat.*, vol. AP-14, issue 8, pp. 302-307, May, 1966

[22] A. Taflove and S. C. Hagness, Computational Electrodynamics: The Finite-Difference Time-Domain Method, 3rd edition. Norwood, MA: Artech House, 2005

[23] J. B. Keller, "Geometrical Theory of Diffraction," *J. Opt. Soc*. vol. 52, issue 2, pp. 116-130, 1962

[24] R. F. Harrington, Field Computation by Moment Methods, New York: Macmillan, 1968

[25] C. Guiffaut and K. Mahdjoubi, “A parallel FDTD algorithm using the MPI library,” *IEEE Antennas Propag. Mag*., vol. 43, no. 2, pp. 94–103, Apr. 2001

[26] K. S. Kunz, and R. J. Luebbers, The Finite Difference Time Domain Method for Electromagnetics, CRC Press, London, 1993

[27] Jean-Pierre Berenger, “A perfectly matched layer for the absorption of electromagnetic waves,” *Journal of Computational Physics*, volume 114, issue 2, pp. 185-200, 1994

[28] J. A. Roden and S. D. Gedney, “Convolution PML (CPML): An efficieint FDTD implementation of the CFS-PML for arbitrary media,” *Microwave Optical Techn. Lett.*, vol. 27, no. 5, pp. 334-339, 2000.

[29] M. Kuzuoglu and R. Mittra, "Frequency dependence of the constitutive parameters of causal perfectly matched anisotropic absorbers," *IEEE Microwave and Guided Wave Letters*, vol. 6, pp. 447-449, 1996

[30] W. C. Chew and W. H. Weedon, "A 3d Perfectly Matched Medium from Modified Maxwells Equations with Stretched Coordinates," *Microwave and Optical Technology Letters*, vol. 7, pp. 599-604, 1994.

[31] R. J. Luebbers and F. Hunsberger, "FDTD for Nth-Order Dispersive Media," *IEEE Transactions on Antennas and Propagation*, vol. 40, pp. 1297-1301, 1992

[32] J. H. Beggs, R. J. Luebbers, K. S. Yee, and K. S. Kunz, "Finite-Difference Time-Domain Implementation of Surface Impedance Boundary-Conditions," *IEEE Transactions on Antennas and Propagation*, vol. 40, pp. 49-56, 1992

[33] L. Zhao and C. K. Ong, “Direct observation of photonic jets and corresponding backscattering enhancement at microwave frequencies,” *J. Appl. Phys*., vol. 105, issue 12, pp. 123512, 2009.

[34] J. F. Poco, and L. W. Hrubesh, “Method of producing optical quality glass having a selected refractive index,” U.S. Patent 6,158,244, 2008.

[35] Z. B. Wang, W. Guo, A. Pena, D. J. Whitehead, B. S. Luk'yanchuk, Lin. Li, Z. Liu, Y. Zhou, and M. H. Hong, “Laser micro/nano fabrication in glass with tunable-focus particle lens array,” *Optics Express*, vol. 16, issue 24, pp. 19706-19711, Nov. 24, 2008.

[36] Gustav Mie, “Beiträge zur Optik trüber Medien, speziell kolloidaler Metallösungen,” *Annalen der Physik*, Vierte Folge, Band 25, No. 3, p 377-445, 1908

[37] P. Debye, “The electromagnetic field around a cylinder and the theory of the rainbow” (translation of “Das elektromagnetische Feld um einen Zylinder und die Theorie des Regenbogens,” Phys. Z. 1908), in Geometrical Aspects of Scattering, P. L. Marston ed. (SPIE, 1994)

[38] A. V. Itagi and W. A. Challener, "Optics of photonic nanojets," *J. Opt. Soc*., Vol. 22, Issue 12, pp. 2847-2858, 2005.

[39] J. A. Stratton, "Cylindrical waves," in *Electromagnetic Theory*, McGraw-Hill, 1941.

[40] M. Born, E. Wolf, Principles of optics: electromagnetic theory of propagation, interference and diffraction of light, Cambridge University Press, Cambridge, New York, 1999

[41] P.W. Anderson, D.J. Thouless, E. Abrahams, D.S. Fisher, “New method for a scaling theory of localization.” *Phys Rev B.*, vol. 22, issue 8, pp. 3519–3526, 1980.

[42] A.A. Abrikosov, I.A. Ryzhkin, “Conductivity of quasi-one-dimensional metal systems.” Adv Phys, vol. 27, Issue 2, pp.147-230, 1978.

[43] N. Kumar, “Resistance fluctuation in a one-dimensional conductor with static disorder.” *Phys Rev B.*, vol. 31, issue 8, pp. 5513–5515, 1985.

[44] R. Rammal, B. Doucot, “Invariant imbedding approach to localization. 1. General framework and basic equations.” *J Phys*, vol. 48, pp. 509–526, 1987.

[45] P. Pradhan, N. Kumar, “Localization of light in coherently amplifying random media.” *Phys Rev B*. vol. 50, issue 13, pp. 9644–9647, 1994.

[46] S.B. Haley, P. Erdos, “Wave-propagation in one-dimensional disordered structures.” *Phys Rev B*, vol. 45, issue 15, pp. 8572–8584, 1992.

[47] P.W. Anderson “Absence of diffusion in certain random lattices.” *Phys Rev.*, vol. 109, issue 5, pp. 1492–1505, 1958.

[48] R. Nevels and J. Jeong, “The time domain Green’s function and propagator for Maxwell’s equations,” *IEEE Trans. Antennas Propagat.*, vol. 52, issue 11, pp. 3012-3018, Nov. 2004

[49] B.P. Bogert, M.J.R. Healy, J.W. Tukey, and M. Rosenblatt, “The quefrency analysis of time series for echoes: Cepstrum, pseudo-autocovariance, cross-cepstrum, and saphe cracking,” in *Time Series Analysis*, M. Rosenblatt, Ed., ch. 15, pp. 209–243, 1963.

[50] A. M. Noll, “Short-Time Spectrum and Cepstrum Techniques for Vocal-Pitch Detection,” *Journal of the Acoustical Society of America*, vol. 36, issue 2, pp. 296-302, 1964.

[51] A. V. Oppenheim, "Superposition in a class of nonlinear systems" Ph.D. dissertation, Res. Lab. Electronics, Massachusetts Institute of Technology, Cambridge, MA, 1965

[52] Marc Richter, Personal communication.

[53] M.-S. Kim, T. Scharf, S. Mühlig, C. Rockstuhl, and H. P. Herzig, "Engineering photonic nanojets," *Opt. Express*, vol. 19, issue 11, pp. 10206-10220, 2011.

List of Appendices

Appendix A

Additional Doctoral Research

Ultra High-Resolution FDTD modeling of a High-Performance VLSI Package for identifying intra-chip EMC Issues

Abstract —The ability to computationally predict, study, and prevent electromagnetic compatibility (EMC) issues arising within the ICs package is crucial for the design process. This study involves a phenomenological study employing an ultra high-resolution, three-dimensional finite-difference time-domain (FDTD) model of a sample IC package having over one billion grid cells. The main goal is to identify resonances and coupling patterns arising within the highly complex IC package. The frequency range of interest extends from 100 MHz to 7 GHz. Results indicate that the arrangement and geometry of the separate power, ground, and signaling networks comprising the IC package greatly influences the electromagnetic behavior within different regions of the package.

I. INTRODUCTION

Unintended electromagnetic issues occurring within an integrated circuit (IC) package is a large concern in the design of ICs as well as for the operation of the complete platform. ICs are continually being designed to operate at higher clock speeds, be integrated at higher densities, and be powered with lower supply voltages. Further, many modern platforms such as notebooks and ultra mobile devices are continually increasing in functionality while also becoming more compact in size. As a result, ICs must be positioned in very close proximity to

other ICs as well as to a variety of high performance wireless communication systems such as Wi-Fi, VoIP, WiMAX, and Bluetooth [1-3], in addition to near field communication technology. All of these trends are causing electromagnetic compatibility (EMC) issues to greatly influence the reliability and operation of electronic devices. In consequence, as the technology progresses, EMC must be at the core of the design process of both the platforms and the components. This is particularly true for ICs, because they normally are the most susceptible component of the system due to risks of over-voltage or over-current.

Initial EMC research focused on ICs was done in 1965. The effects of EM fields from nuclear explosions on electronic devices were studied at the Special Weapons Center based at Kirtland Air Force Base. The simulation software SCEPTRE [4] was developed by IBM as a result of this pioneering work. Since then, there have been additional efforts to study the EMC performance of ICs. However, most of the research concerns about EMC issues external to the IC package (conducted coupling, susceptibility, and emission). Further, an example analysis of ICs has relied on a complicated integration of measurements, simulations, and analytical calculations through the use of macromodels [5]. In fact, as recently as 2005, the authors of Ref. [5] state that for studying ICs, “the combination of propagation effects with possibly very complex geometry… makes a direct full-wave approach not feasible.”

More recently, Srinivasan [6] employed an unconditionally stable time-domain technique using Laguerre polynomials to develop a methodology for chip-package cosimulation of ICs. To tackle the problem, the IC is divided into sub-

blocks (signal delivery and power delivery networks) for analysis using a full-wave Laguerre equivalent circuit procedure before integrating the results together.

In the work reported in [7], the computational power afforded by today's supercomputers is employed to simulate on a grand scale a complete IC package as well as the underlying printed circuit board (PCB). Specifically, the full Maxwell's equations are solved using an ultra high-resolution, three-dimensional (3-D) finite-difference time-domain (FDTD) [8, 9] model having over 1 billion grid cells and simultaneously accounting for the power, signal and ground networks (which in the remainder of this Appendix are referred as functional layers) of the IC package.

The simulations and results provided in this Appendix are taken from [7] and are directed towards obtaining resonance and coupling patterns throughout the IC package under varying excitation scenarios. Utilizing 384 cores, each of the excitation scenarios for this detailed model takes 26 hours to run. The frequency range of interest extends from 100 MHz to 7 GHz.

The present phenomenological study represents an advance towards enabling engineers to obtain a comprehensive understanding of the fundamental physics behind EMC issues within ICs, and towards providing design parameters necessary for improving and optimizing IC package layouts.

Previously, two related conference abstracts [10, 11] briefly document initial stages of the project by describing the general modeling approach employed for this study. A brief description of the sample IC package as well as one example

snapshot of electromagnetic energy propagating within one layer of the package was then provided in [12]. Reference [7], however, significantly builds off of the work of [10-12] by providing a detailed analysis of the electromagnetic behavior, particularly resonances and coupling, within different regions of the IC package and for varying excitations of the IC package. The detailed model description as well as all of the result figures and analyses are original to [7].

State of the art IC EMC laboratory test techniques are based on measuring either the emissions from the IC (TEM cells, pin current measurements, and near-magnetic field scans) or the susceptibility to electromagnetic noise (bulk current injection, direct power injection, and field coupled) [13]. In all these methods the instrumentation is located external to the IC and therefore are not suitable for direct comparisons against the results presented in this Appendix that concern the inside of the package.

The analysis provided in [7] is unique because the geometry of the layers of the IC package does not behave in an analytically predictable nature. For example, the periodic vias comprising each layer are not all connected to the same adjacent conducting planes (layers); the vias are instead each assigned to one of the three different functional layers (signal, ground, power) and as such many of them must extend through some conducting layers of a different functional type without forming an actual connection. As a result, the vias within the different regions of the package do not behave in a manner according to typical electromagnetic bandgap structures or substrate integrated waveguides as in [14].

The remainder of this Appendix is taken from [7] and is organized as follows. Section II below demonstrates the validity of the code by duplicating results of similar structures reported by other authors. Section III below provides an overview of the FDTD model. Section IV describes the general methodology of the analysis and the simulation cases that are considered. The corresponding simulation results are then documented and discussed in Section V. Finally, section VI concludes the paper.

II. CODE VALIDATION

In order to validate the code that is used for the modeling of the IC package we first successfully reproduce results obtained for a similar, but much simpler structure as reported by Shahparnia et al. [15, 16]. In these References, the authors developed an analytical model to predict the resonant properties, pass-band and stop-band of electromagnetic bandgap (EBG) structures embedded in PCBs and packages. They compare their results against finite element (FE) based results. The frequency range of interest, gap between conducting planes and via diameter are comparable to those corresponding to the IC package analyzed in this paper. A lateral view of the considered 3-D structure is shown in Fig 1.

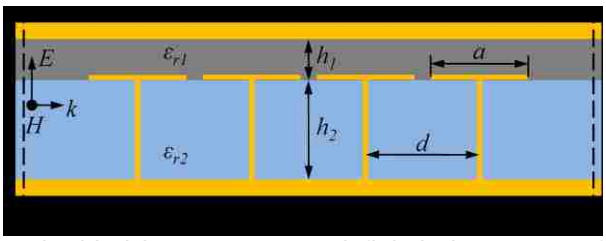

Fig. 1. EBG structure embedded in a PCB. Four infinitely long rows of EBG cells are placed between the 2 ports that are used to calculate the S parameters.

Table 1 collects the band-stop frequency range of various EBG structures. The limits of the gap are determined by a -20 dB criteria of the scattering parameter S21. For all considered cases the FDTD model shows satisfactory agreement, in particular with the results obtained from the FE simulations.

Table 1: Comparison of FDTD model calculations and results reported in [15]

d (mm)	a (mm)	h_1 (mm)	h_2 (mm)	ε_{r1}	ε_{r2}	Vias diameter (μm)	FE Gap (GHz)	Model Gap (GHz)	FDTD Gap (GHz)
10.4	10×10	1.54	1.54	4.1	4.1	800	2.1-4.0	2.5-4.0	2.0-3.9
10.4	10×10	1.54	1.54	8.2	4.1	800	1.6-3.7	1.8-3.7	1.7-4.0
10.4	10×10	1.54	1.54	12.3	4.1	800	1.3-3.1	1.5-3.5	1.4-3.6
10.4	10×10	1.54	1.54	16.4	4.1	800	1.2-2.9	1.3-3.4	1.3-3.3
2.2	2×2	0.016	0.1	4.1	4.1	125	6.0-18.1	6.1-14.7	7.2-19.5

III. FDTD MODEL OF SAMPLE IC PACKAGE AND PCB

The FDTD model employed in this study encompasses 2580×2580×160 grid cells in each x, y, and z Cartesian direction to finely model the sample IC package and the underlying sample PCB. A general schematic of the model is shown in Fig. 2. The complete FDTD model includes details of the conducting layers, silicon, dielectrics, vias, ground / power traces, and solder balls. For a practical implementation of such demanding computation and storage it becomes necessary to exploit the parallel processing techniques. Specifically, we employ the domain decomposition parallelism scheme in which the computation domain is divided into equal rectangular sub-areas. The essential elements of a parallel algorithm for the FDTD method using the Message Passing Interface (MPI) library are reported in [17].

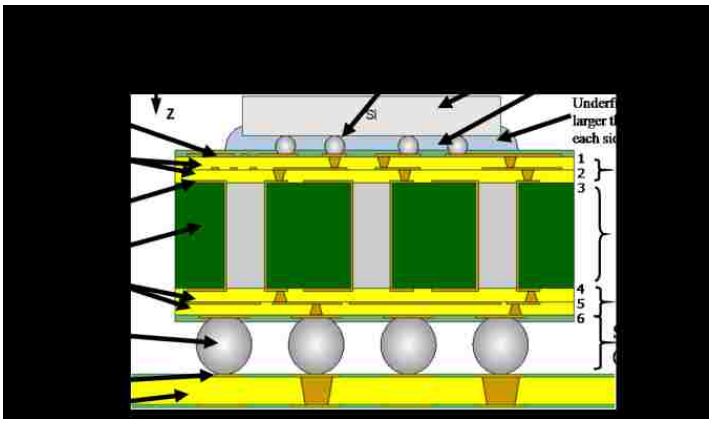

Fig. 2. General cross-sectional view of the sample six-layer IC package with the underlying sample PCB.

Figs. 3, 5, and 6 are designed with a specific color code to identify materials and functional layers. The white color was defined to represent air, red corresponds to any dielectric, yellow corresponds to ground, green corresponds to power and blue corresponds to signal.

There are in total six conducting layers in the IC package. Conducting Layers 2, 4, and 6 are ground planes while Conducting Layers 3 and 5 belong to the power network. Conducting Layer 1 is split into two conducting surfaces of equal area as shown in Fig. 3: the left side is ground and the right is power. The via pitch under the die shadow is denser than outside the die shadow (320 μm vs. 1 mm). The PCB is comprised of two conducting planes; one is power and the other is ground.

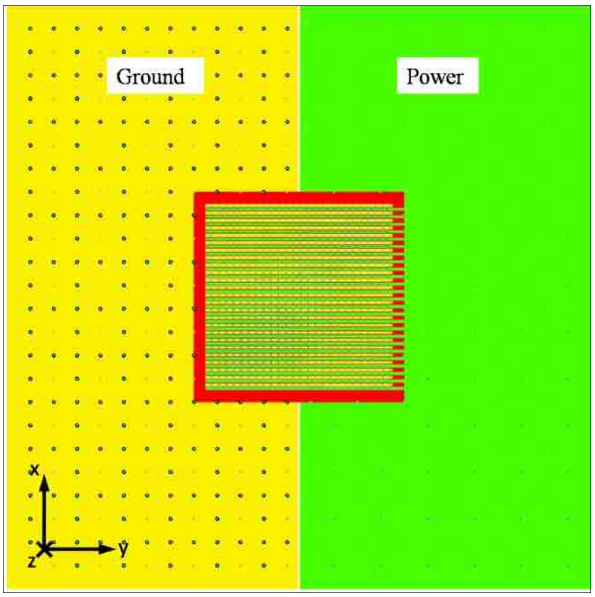

Fig. 3. Detailed top view of the IC package Conducting Layer 1 of Fig. 1. The circles represent the via/via pad/via anti-pad locations.

Each via within the structure is assigned to the signal, ground, or power function layer. Each via is thus only connected to its corresponding signal / ground / power conducting layer, respectively. That is, the ground and power vias are shorted at each end only to ground and power conducting layers, respectively, and the signal vias are connected to ground conducting layers through lumped resistors. As a result, because the ground, signal, and power conducting layers alternate through the structure, the vias must extend through an opening through some conducting planes to connect to a conducting plane further away. This geometry greatly complicates the electromagnetic behavior throughout the entire IC package.

The FDTD grid has a uniform cell size of 10×10×15 μm in x, y, and z-directions, respectively. This resolution is high enough to resolve the smallest circular via diameter within the model without introducing stair-casing effects into the computational results.

Table 2 lists all materials within the model and their corresponding electrical properties. The conductivities are calculated assuming a clock frequency of 1 GHz.

Table 2: Materials Properties

Material	Relative Permittivity (ε_r)	Loss Tan	Conductivity (S/m)
Silicon	10.24	0.025	0.01420
Underfill	3.5	0.025	0.00487
Build-Up	3.7	0.017	0.00350
Core	4.6	0.017	0.00435
FR4	4.3	0.017	0.00407

IV. METHODOLOGY AND SIMULATION CASES

A total of six simulation cases are conducted to characterize the resonances and coupling within the package. In all cases, the source is a modulated Gaussian pulse centered at 8 GHz and having spectral energy from 100 MHz to 20 GHz. We primarily consider the frequency range of 100 MHz to 7 GHz, but in a few cases we examine the performance of the IC up to 20 GHz for additional behavioral information.

For each simulation case, two neighboring solder balls are excited with the source waveform skewed at 50%. The excitation is implemented as a set of lumped resistive voltage sources [18] along the surface of both solder balls so that the total resistance of each lumped resistive source is 50 ohms. The unique feature of each simulation case is the location of these sourced pair of solder balls. Fig. 4(a) shows the source locations for simulation cases 1 – 4 having the excitation implemented at two motherboard connection solder balls between Conducting Layer 6 and the PCB upper conducting layer.

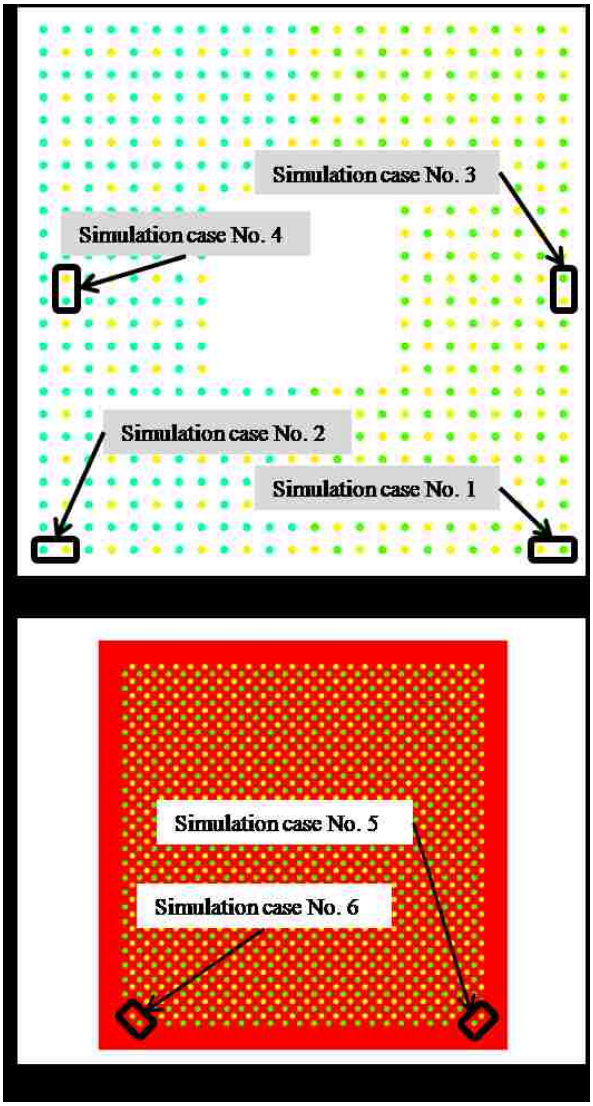

Fig. 4. Sources locations for the different simulation cases. (a) Motherboard connection solder balls. (b) Solder balls in the under-fill region, a zoomed-in view to the under-die zone.

Likewise, Fig. 4(b) shows the source locations for simulation cases 5 and 6 having the excited solder balls in the underfill region connecting the die with the packaging. Each of the two exited solder balls belongs to a different functional layer. For example, for Simulation Case 1, a solder ball at the lower right corner of the package belonging to the power network is excited, along with a neighboring solder ball to its left belonging to the ground network. Similarly, in Simulation Cases 3, 5, and 6, two neighboring power and ground solder balls are

excited as shown in Fig. 4. And in Simulation Cases 4 and 2, two neighboring signal and ground solder balls are excited.

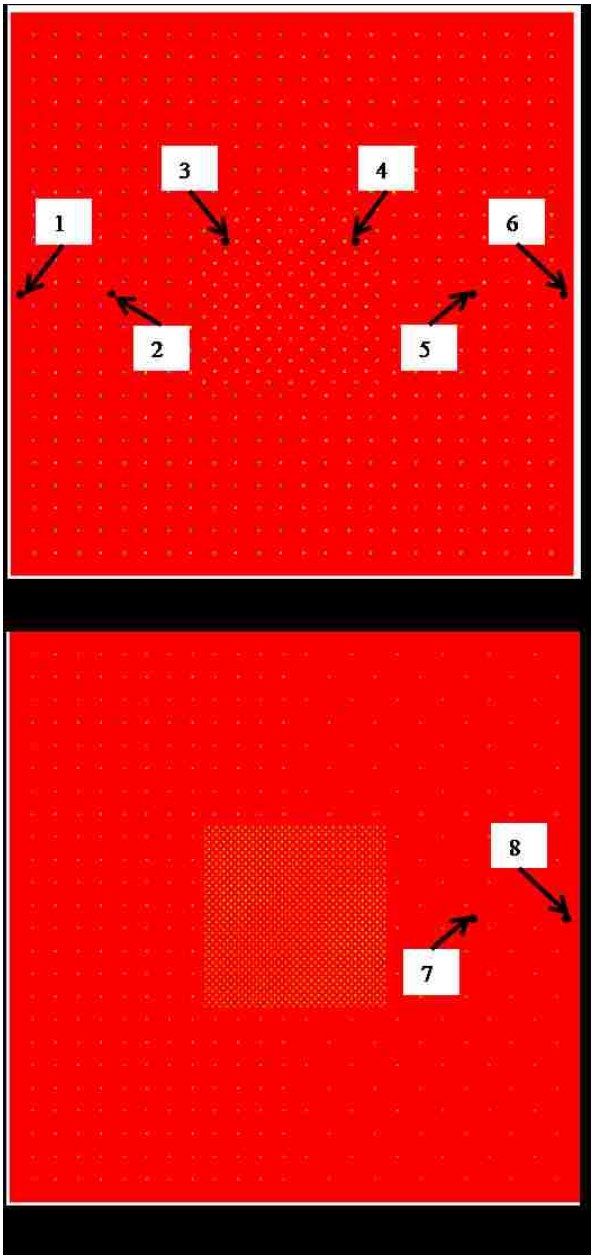

Fig. 5. Locations and numbering of each observation point at which the electric fields are recorded. (a) Build-up between Conducting Layers 4 and 5. (b) Build-up between Conducting Layers 1 and 2.

The response of the package to the excitations is based on analyzing the behavior of the electric field throughout the IC, as well as the electric conduction current flowing through the vias. Specifically, the z component of the electric field

(Ez) is recorded versus time during each of the six simulation cases at 64 observations points. Fig. 5 shows eight key observation points that will be used in this paper to illustrate the variation of the resonances within different zones of the package.

To compute the electric current (Iz), an Ampere's Law contour-line integration of the magnetic field is performed around the vias, of which we have selected five (from 90) to best illustrate the results. Each integration path for these five selected vias lies in the x-y plane at the midpoint between Conducting Layers 3 and 4 as shown in Fig. 6.

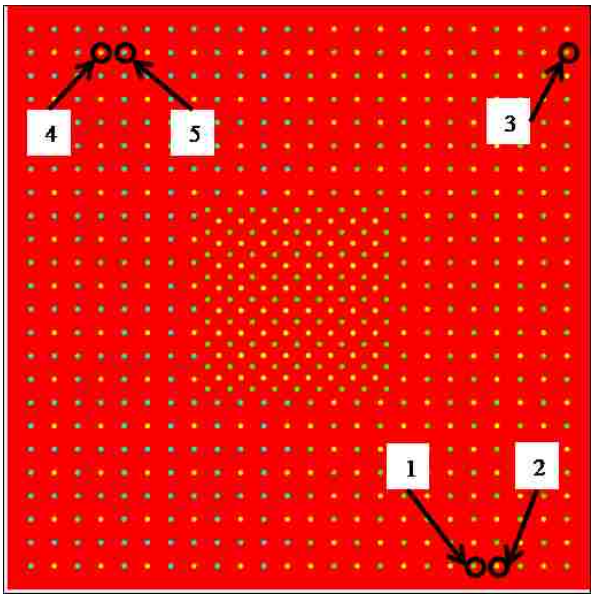

Fig. 6. Location and numbering of the vias between Layers 3 and 4 at which the electric conduction currents are computed.

The data for both Ez and Iz are normalized relative to the source spectral waveform and then to the maximum value of the response at the observation point or via having the strongest response to the excitation obtained during time stepping for each corresponding simulation. This second normalization step

allows us to compare relative to each other the magnitudes of the observed values within each separate simulation case.

The normalization procedure may be expressed as

$$a_i(f) = \frac{\frac{A_i(f)}{S(f)}}{MAX\left[\frac{A_{reff}(f)}{S(f)}\right]},$$

where ai and Ai refer, respectively, to the normalized and un-normalized values of Ez or Iz for the observation point or via i as a function of frequency f. S refers to the source waveform. The reference Areff is taken to be the corresponding Ez or Iz having maximum peak response to the excitation source relative to the other studied locations for that particular simulation case.

V. RESULTS AND ANALYSIS

The computational results demonstrate that the frequency content of the EM energy observed propagating through the package is determined to be dependent on the spatial location of the source and observation point within the structure and relative to each other. The complex sample package of Fig. 2 therefore cannot be analyzed using the results of a single simulation. Some regions of the package block certain ranges of spectral energy, while the conducting layers naturally block all of the electromagnetic energy within the frequency range of interest. Additionally, mutual coupling shifts the spectral energy and resonances throughout the structure. As a result, different simulation scenarios are performed with the sources spatially varied for each case in order to characterize which zones of the structure lead to specific resonances and behaviors. In this Section, we utilize the results from six simulation cases to

demonstrate the resonances, coupling, and shielding produced by different zones within the package.

A. Electric Conduction Currents

As stated earlier, the package is comprised of a ground network, power network and signaling vias (functional layers). The computed currents at different vias corresponding to these different functional layers indicate that each functional layer has its own set of resonant frequencies. Because of mutual coupling, these resonances continually shift towards or away from each other as the observation position moves within the package. Simultaneously, we observe in some regions of the structure that some spectral energy is shifted even to spectral ranges not included in the source spectrum (well above 20 GHz). Only while the EM energy propagates through a uniform dielectric region of dimensions on the order of a wavelength do the resulting resonant frequencies remain constant with position.

Simulation Case 1 best illustrates the shifting of the resonances due to mutual coupling. The electric current at Via 1, which is positioned almost directly above the sourced solder balls, shows that the power network resonates at 1.42 and 6.74 GHz. Similarly, the current at Via 2, also positioned almost directly above the sourced solder balls, shows that the ground network resonates at 2.66 GHz. Both Via 1 and Via 2 currents are illustrated in Fig. 7. As we move laterally away from the source location, however, any other vias within the power or ground networks on the right side of the package are found to have resonant frequencies between those of Vias 1 and 2. This is illustrated in Fig. 8 for Via 3, which is on the same right side but opposite end of the structure relative to the sourced

solder balls. Via 3 has two resonant frequencies: one at 1.58 which is between the 1.42 and 2.66 GHz resonant frequencies of Vias 1 and 2 and the other at 4.38 GHz which is between the 2.66 and 6.74 GHz resonant frequencies of Vias 1 and 2. Further observations indicate that the higher 4.38 GHz resonance of Via 3 diminishes rapidly as the EM energy propagates through the outer periodic ground and power vias on the right side of the package positioned outside the shadow region of the die. However, the resonance at 1.58 GHz can propagate through these periodic vias.

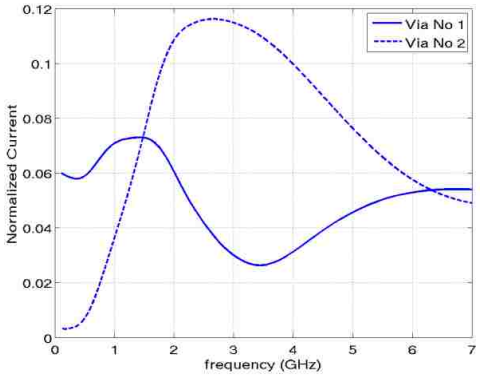

Fig. 7. Spectral response of the electric current at Vias 1 and 2 for Simulation Case 1.

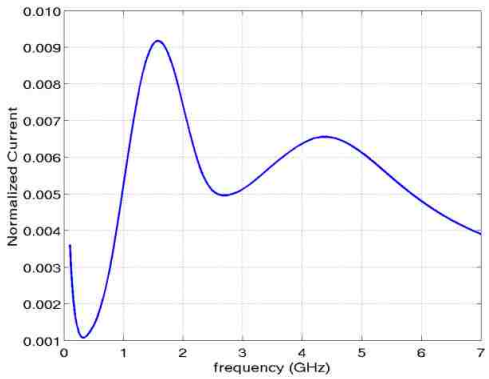

Fig. 8. Spectral response of the electric current at Via 3 for Simulation Case 1.

Regarding the left side of the package, we find from Simulation Case 2 that the ground network weakly resonates at 0.88 GHz on the left side of the package (same side as the sourced solder balls) within the main frequency range of

interest (100 MHz to 7 GHz). Fig. 9 shows this resonance for Via 4 (ground via), which is positioned on the same left side but opposite end of the structure relative to the sourced solder balls. However, by checking the spectral data of this same via current up to 20 GHz (shown in Fig. 10) instead of 7 GHz, it can be seen that most of the resonance spectral energy of the ground network is above our main frequency range of interest. Within the range of 100 MHz to 7 GHz, the magnitude of the current flowing through each of the signal vias is always an order of magnitude lower than the current flowing through any of its neighboring ground vias. These signal vias thus act to block the EM energy on the left side of the package.

We also find from Simulation Case 2 that the signal vias on the left side of the package do not have any defined resonances between 100 MHz and 7 GHz. Further, most of the signal vias currents on the left side of the package are above 10 GHz, as illustrated for Via 5 (signal via) in Fig. 10.

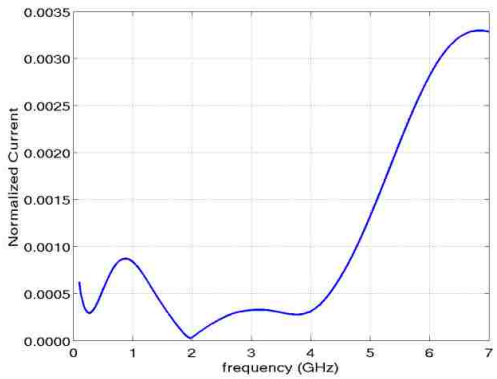

Fig. 9. Spectral response of the electric current at Via 4 for Simulation Case 2.

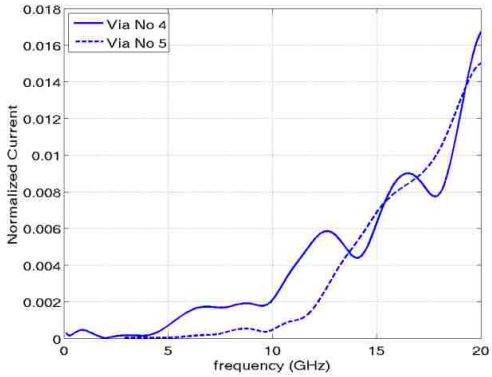

Fig. 10. Spectral response up to 20 GHz of the electric current at Vias 4 and 5 for Simulation Case 2.

B. Electric Fields

The build-up between Conducting Layers 4-5 and 5-6 has two main resonant frequencies on the right side of the package. This is illustrated in Fig. 11 for Simulation Case 1. At Observation Point 6 (located between Conducting Layers 4-5 on the same right side of the structure as the sourced solder balls), Ez is observed to have resonances at ~1.80 GHz and ~5.34 GHz, with the higher frequency (~5.34 GHz) resonance being wider band. Note that for Via 3 the Iz resonances were found centered at 1.58 and 4.38 GHz. This further illustrates the continual shift of resonant frequencies with position. Further, by comparing Observation Point 6 (positioned on the periphery of the package, just outside the periodic vias) of Fig. 11 with Observation Point 5 (positioned almost half-way towards the center of the structure) of Fig. 12, it is observed that the higher frequency 5.34 GHz resonance diminishes as the energy propagates from the periphery of the packaging into the periodic structure formed by the vias.

The lower frequency (~1.80 GHz) resonance on the right side of the package is found to be stronger within the build-up between Conducting Layers 1-2 and 2-3 than in the build-up between Conducting Layers 4-5 and 5-6. Observation Points

7 and 8 (shown in Figs. 11 and 10, respectively) demonstrate this using results from Simulation Case 1. Additionally, the higher frequency resonance (at ~5.34) is no longer present at Observation Points 7 and 8.

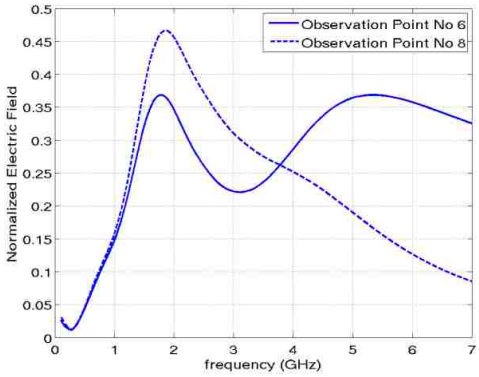

Fig. 11. Spectral response of the electric field at Observation Points 6 and 8 for Simulation Case 1.

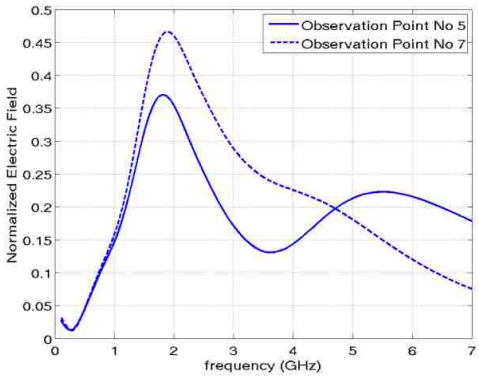

Fig. 12. Spectral response of the electric field at Observation Points 5 and 7 for Simulation Case 1.

Fig. 13 is an example 2-D slice of Ez values that demonstrates the resonances occurring within the core for Simulation Case 1. It is observed that the periphery of the package acts like a transmission line wherein the EM energy propagates at the higher frequencies (5.34 GHz). The reduction of this ~5.34 GHz energy as the EM energy propagates into the periodic vias is also observable in Fig. 13.

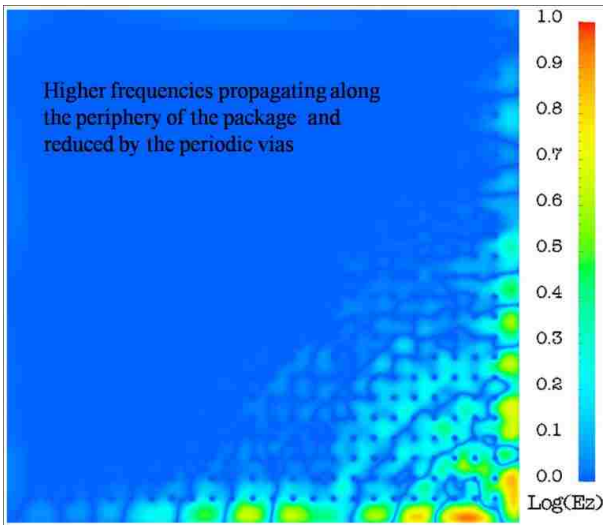

Fig. 13. Electromagnetic energy propagating through the core for Simulation Case 1. A planar cut of Ez values at the midpoint of the gap between Conducting Layers 3 and 4 is shown.

Simulation Cases 5 and 6 show that the region below the die has two resonances, one at ~500 MHz and the other at ~1.6 GHz (shown in Fig. 14). The strongest amplitudes at these frequencies are located in the build-up between Conducting Layers 4-5 and 5-6, however these resonances are also significant in the solder balls connecting the silicon layer to the package (underfill layer) as well as in the build-up between Conducting Layers 1-2 and 2-3. Interestingly, for different Simulation Cases, and thus source locations, these two resonances are also shifted towards each other by varying amounts, resulting for Simulation Cases 1 and 3 in a single but wider bandwidth resonance.

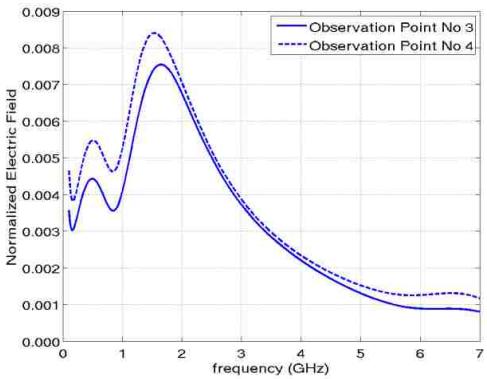

Fig. 14. Spectral response of the electric field at Observation Points 3 and 4 for Simulation Cases 5 and 6 respectively.

In all of the simulation cases, the strongest response always lies in the build-up layers between Conducting Layers 1-2, 2-3, 4-5 and 5-6 (numbered according to Fig. 2), but not in the core (between conducting planes 3-4). This is because no vias are terminated in Conducting Layers 3 and 4 bounding the core. That is, at every connection of a via to a conducting plane, EM energy is radiated, and since no vias are terminated on either side of the core, the signal energy is lower within that region. For example, in the snap-shot of Ez shown in Fig. 15, the 1st and 3rd vias (from right to left) are terminated in Conducting Layer 1. As a result, these vias radiate energy outside (above) the package as well as in the build-up between Conducting Layers 1 and 2. The 2nd via, however, is terminated in Conducting Layer 2 and as a result does not radiate energy above the package (above Conducting Layer 1), but instead radiates energy upwards between Conducting Layers 1 and 2, and downwards, between Conducting Layers 2 and 3.

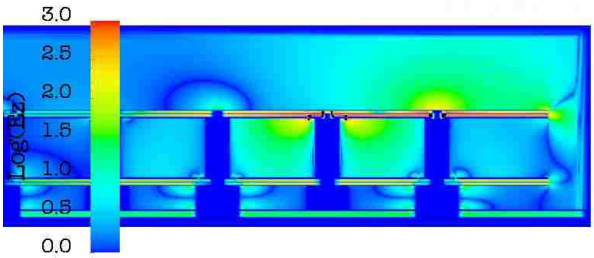

Fig. 15. EM energy propagating through the package for Simulation Case 1. Vertical slice of Ez intersecting the center of Vias 1 and 2. Zoomed-in view to the three right most vias of the entire structure.

Regarding the left side of the package, only the build-up between Conducting Layers 4-5 and 5-6 resonate weakly at ~680 MHz, as observed at Observation Point 2 for Simulation Case 2. But as for the analysis of the currents, this

resonance can be neglected compared to all the spectral energy present at frequencies above 7 GHz as shown in Fig. 16.

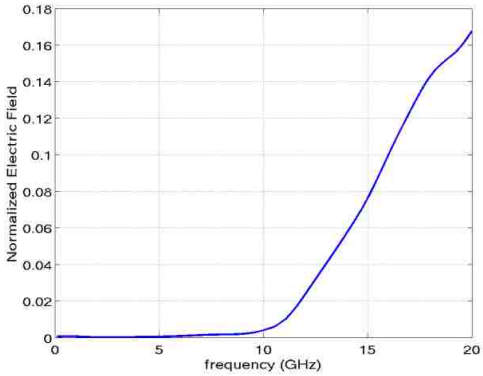

Fig. 16. Spectral response up to 20 GHz for the electric field at Observation Point 2 for Simulation Case 2.

In Simulation Case 6, which is the only simulation case of the six wherein the source is located on the left side of the package and the excited solder balls correspond to the ground and power networks, most of the signal energy propagates only along the periphery of the left side of the package. This is apparent by comparing Observation Point 2 with its symmetry Observation Point 5. A comparison of Observation Points 1 and 2 for Simulation Case 6 illustrates this effect in Fig. 17.

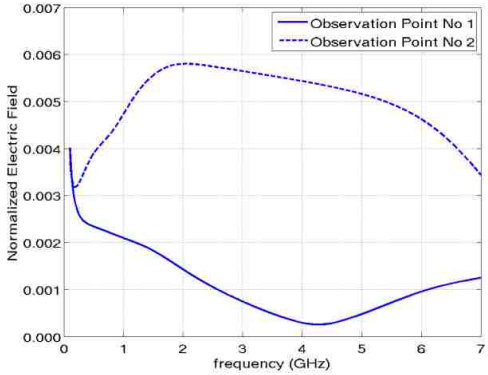

Fig. 17. Spectral response of the electric field at Observation Points 1 and 2 for Simulation Case 6.

VI. CONCLUSION

We have performed a phenomenological study with the goal of examining resonances and coupling within a sample IC package using a greater than one-billion cell full-Maxwell's equations FDTD model. Results from six separate simulation cases permitted us to demonstrate the behavior and characteristics of each of the three functional layers of the IC as well as the different regions of the package, such as under-die, left side, right side, core, build-up layers, etc.

Due to the highly complex geometry and interconnections of the IC package along with the effects introduced by the underlying PCB, EMC for IC design is a difficult problem. It is apparent from the results presented in this paper, however, that an external wireless transmitter emitting radiation within the frequency range of 500 MHz to 2 GHz could, depending upon its location and frequency content, present a hazard for specific regions within the IC package. That is, especially if the transmitter's frequency content includes a resonance found in a region of the package and that region of the package lies within a direct propagation path of the transmitter, the radiation from the transmitter may couple into the IC.

APPENDIX A REFERENCES

[1] "Beyond the call- Intel and Motorola explore new possibilities for the cell phone platform," URL: http://techresearch.intel.com/articles/Exploratory/1431.htm

[2] "Intel's portable prototypes," PC Magazine, URL: http://www.pcmag.com/article2/0.2704.1884623,00.aspR. F. Harrington, *Time-Harmonic Electromagnetic Fields*, McGraw-Hill, New York, 1961.

[3] "New Intel Portable PC concept at Computex Paipei 2007," Coolestgadgets.com, URL: http://www.coolest-gadgets.com/20070606/new-intel-portable-pc-concept-atcomputex-taipei-2007

[4] S R. Sedore, Automated digital computer program for determining responses of electronic circuits to transient nuclear radiation (SCEPTRE), AFWL TR 66-126, *Air Force Weapons Laboratory*, 1967a.

[5] F. Canavero, S. Grivet-Talocia, I. A. Maio, and I. S. Stievano, “Linear and nonlinear macromodels for system-level signal integrity and EMC assessment,” *IEICE Trans. Commun.: Invited Paper, Special section of 2004 International Symposium on EMC*, vol. E88-B, No. 8, Aug. 2005, pp. 3121-3126.

[6] K. Srinivasan, “Multiscale EM and circuit simulation using the Laguerre-FDTD scheme for package-aware integrated-circuit design,” Ph.D. dissertation, School of ECE, Georgia Institute of Technology, Atlanta, GA, 2008.

[7] C. Mendez Ruiz and J. J. Simpson, “Ultra high-resolution FDTD modeling of a high-performance VLSI package for identifying resonances and couplings,” Applied Computational Electromagnetics Society Journal (accepted)

[8] K. S. Yee, "Numerical solution of initial boundary value problems involving Maxwell's equations in isotropic media," *IEEE Trans. Antennas Propagat*., vol. AP-14, issue 8, pp. 302-307, May, 1966.

[9] A. Taflove and S. C. Hagness, Computational Electrodynamics: The Finite-Difference Time-Domain Method, 3rd edition. Norwood, MA: Artech House, 2005.

[10] J. J. Simpson, B. Horine, and H. Heck, "Ultra high-resolution FDTD modeling of an integrated circuit package for characterizing and solving EMC problems in compact portable electronic devices," *Proc. IEEE AP-S Intern 't Symp. and USNC/URSI Nat '1 Radio Science Meeting*, San Diego, CA, July 2008.

[11] J. J. Simpson, "FDTD full-Maxwell's equations modeling from near-DC to light," *Proc. 24th Int'l Review of Progress in Applied Computational Electromagnetics (ACES)*, Niagara Falls, Canada, April 2008.

[12] C. Mendez Ruiz, J. J. Simpson, B. Horine, K. Slattery, “Utra high-resolution FDTD modeling of a high-performance VLSI package,” *IEEE AP-S International Symposium and USNC/URSI National Radio Science Meeting*, Charleston, SC, June 2009.

[13] S. Ben Dia, M. Ramdani, E. Sicard, editors, Electromagnetic Compatibility of Integrated Circuits – Techniques for Low Emission and Susceptibility, Springer, 2006.

[14] F. Xu and K. Wu, “Guided-wave and leakage characteristics of substrate integrated waveguide,” *IEEE Trans. Microw. Theory Tech.*, vol. 53, no. 1, pp. 66–73, Jan. 2005.

[15] S. Shahparnia and O. M. Ramahi, “A simple and effective model for electromagnetic bandgap structures embedded in printed circuit boards,” *IEEE Microw. Wireless Compon. Lett.*, vol. 15, no. 10, pp. 621–623, Oct. 2005.

[16] S. Shahparnia and O. M. Ramahi, “Miniaturazed electromagnetic bandgap structures for ultra-wide band switching noise mitigation in high-speedprinted circuit boards and packages,” *in Proc. 13th Topical Meeting Electrical Performance Electronic Packaging.*, Portland, OR, Oct. 25-27, 2004, pp. 211-214.

[17] C. Guiffaut and K. Mahdjoubi, “A parallel FDTD algorithm using the MPI library,” *IEEE Antennas Propag. Mag.*, vol. 43, no. 2, pp. 94–103, Apr. 2001.

[18] M. Piket-May, A. Taflove, and J. Baron, “FD-TD modeling of digital signal propagation in 3-D circuits with passive and active loads,” *IEEE Trans. Microwave Theory and Tech*., vol. 42, issue 8, pp. 1514-1523, Aug, 1994.

Appendix B

Author's Publications

[1] C. Mendez Ruiz and J. J. Simpson, "Ultra high-resolution FDTD modeling of a high-performance VLSI package for identifying resonances and couplings," *Applied Computational Electromagnetics Society Journal* (accepted).

[2] C. Mendez Ruiz and J. J. Simpson, "Analysis of backscattered fields from photonic nanojet-illuminated inhomogeneous dielectric objects having rough surfaces," *Proc. URSI National Radio Science Meeting*, Boulder, CO, Jan. 2011 (invited).

[3] C. Mendez Ruiz and J. J. Simpson, "Detection of embedded ultra-subwavelength-thin dielectric features using elongated photonic nanojets," *Optics Express*, vol. 18, iss. 16, pp. 16805-16812, 2010

[4] C. Mendez Ruiz and J. J. Simpson, "Ultra High-Resolution FDTD Modeling of a High-Performance VLSI Package for Identifying EMC Issues," *Proc. URSI National Radio Science Meeting*, Boulder, CO, Jan. 2010.

[5] C. Mendez Ruiz, J. J. Simpson, B. Horine, K. Slattery, "Ultra high-resolution FDTD modeling of a high-performance VLSI package," *IEEE AP-S International Symposium and USNC/URSI National Radio Science Meeting*, Charleston, SC, June 2009.

Appendix C

Awards

2010-2011 IEEE Antennas and Propagation Society Doctoral Research Award

Spring 2011 ECE Outstanding Graduate Student